الجمهورية الجزائرية الديمقراطية الشعبية
République Algérienne Démocratique Et Populaire
وزارة التعليم العالي والبحث العلمي
Ministère de L'Enseignement Supérieur et de La Recherche Scientifique
جامعة فرحات عباس- سطيف1
Université Ferhat Abbas - Sétif 1

THÈSE

Présentée à l'Institut d'Optique et Mécanique de Précision pour l'obtention du Diplôme de

DOCTORAT 3ème Cycle LMD

Domaine : Sciences et Techniques
Filière : Optique et mécanique de Précision
Spécialité: Matériaux pour l'optique et l'optoélectronique

Par
Meriem Aloui

Thème

Elaboration et caractérisation des nanostructures à base d'oxydes métalliques et leurs applications à l'optoélectronique

Soutenue, le: 20 juillet 2022 **Devant le jury composé de:**

Président du Jury	**N. Belkhir**	**Prof**	**F.A.U Setif -1**
Directeur de thèse	**L.Mentar**	**Prof**	**F.A.U Setif -1**
Co-directeur de thèse	**A. Beniaiche**	**Prof**	**F.A.U Setif -1**
Examinateur	**A. Zegadi**	**Prof**	**F.A.U Setif -1**
Examinateur	**M.R. Khelladi**	**Prof**	**M.B.I.U BBA**

PEOPLE'S DEMOCRATIC REPUBLIC OF ALGERIA

MINISTRY OF HIGHER EDUCATIONAND SCIENTIFIC RESEARCH

FERHAT ABBAS UNIVERSITY – SETIF -1-

THESIS

Submitted to Institute of Optics and Precision Mechanics

For the degree

Of PhD

Materials for optics and optoelectronics

By

Meriem ALOUI

Title

Elaboration and characterization of metal oxide nanostructures and their applications to optoelectronics

Defended on: July 20th,2022 **In front of the composed committee of**

Chairman	**N. Belkhir**	**Professor**	**F.A.U Setif -1**
Supervisor	**L.Mentar**	**Professor**	**F.A.U Setif -1**
Co-Supervisor	**A. Beniaiche**	**Professor**	**F.A.U Setif -1**
Examiners	**A. Zegadi**	**Professor**	**F.A.U Setif -1**
Examiners	**M.R. Khelladi**	**Professor**	**M.B.I.U BBA**

Abstract

The nanostructuration of solar cells is an interesting approach to improve the photovoltaic conversion efficiency (PCE), in which the main goal of this thesis is to enhance the performance of the electrodeposited Cu_2O and ZnO nanostructures for optoelectronic devices. Many key parameters effect are studied for both metal oxides to control their physical and electrochemical properties. Firstly, a comparative study between galvanostatic and potentiostatic mode for the ZnO nanosheets ($ZnO_{(NS)}$) and ZnO nanowires ($ZnO_{(NW)}$) is taken place. Secendly, Similar strategy was applied for Cu_2O nanostructures and Cu_2O nanoparticles. The structural, morphological, optical and electrochemical parameters were investigated for the synthesized ZnO and Cu_2O nanostructures, where they show good performance and high photoelectrochemical stability. Finaly, a heterojunction design ($Cu_2O\big/n-ZnO_{(NW)}\big/ZnO_{(NS)}$) was proposed and exanimated under the different electrodeposition approaches. Whereas, $n-ZnO_{(NW)}\big/ZnO_{(NS)}$ is the conductive layer in the heterojunction and $p-Cu_2O$ is the absorber layer.

Dedication

I dedicate this thesis

To my beloved parents, for their constant support

and unconditional love!

Meriem

Acknowledgements

A doctoral thesis is often described as a solitary endeavour; however the long list that follows definitely proves the opposite!

All the praises and thanks be to **ALLAH**, the most beneficent and merciful, for giving me this opportunity to increase my scientific knowledge, and his help in giving patience to complete this work. **ALLAH** says: " For should you try to count Allah's blessings, you could never compute them" (An-Nahl 16:18).

" وَإِنْ تَعُدُّوا نِعْمَةَ اللَّهِ لا تُحْصُوها إِنَّ اللَّهَ لَغَفُورٌ رَحِيمٌ (١٨) " { النحل:١٨ }

At first, I would like to express my gratitude for the continuous support, insight and patience of my supervisor ***Pr. Loubna MENTAR***. Thanks to her for accepting to advisor me in my thesis. For guidance and valuable suggestions over the past years. All my gratitude to my co-supervisor ***Pr. Abdelkrim BENIAICHE*** , for his motivation for encouraging me to work in new domain quite far from what I did before during my career until the Master. Thanks to his help, advices and support.

Foremost, I am grateful to the Laboratory of Chemistry, Molecular Engineering and Nanostructures (LCEMN), in particular, laboratory director ***Pr. Amor AZIZI*** for his support and the technical assistance during the past years.

I am very grateful to ***Pr.Nabil BELKHIR*** , professor at the University of Farhat ABBES, Sétif 1, I am sensitive to the honor he gave me by agreeing to read this manuscript

and for agreeing to serve as chairman of the panel. I would like to thank all members of the examining committee of this PhD thesis. Thanks to ***Pr.Ameur ZEGADI***, professor at University of Farhat ABBES, Sétif 1 and ***Pr.Mohamed redha KHELLADI***, professor at University Mohamed El Bachir El Ibrahimi, BBA. For accepting the evaluation of my work, and for the time they spent reading and commenting my thesis.

I say big thanks to ***Dr. Halla LAHMAR*** for the serious supervision in the first year of my project, for her many pieces of advice and discussion. Where she charring her time to taught me a lot of things and new basics in this area of research.

I wish to extend my heartfelt thanks to all the members of Ege University Institute of Nuclear Sciences, Izmir-TURKEY. I am deeply grateful to ***Pr. Sabrye YUSAN*** , and ***Pr. Sule AYTAS*** for accepting my scientific visit for five weeks, their useful discussions and technical assistance, which made it possible for me to spend the precious time. I'll never forget the very beautiful moments with them. Thanks to their social support and very kind behavior.

My sincere thanks also goes to our laboratory members. Whome provided me an opportunity to work with them, and who gave access to the research facilities.

I am extremely thankful to my professors of IOMP since 2010, for teaching me new things, they kept me informed about topical research on optics and for those specific human qualities. I learned from them how to behave in research life, Thanks to their many pieces of advice and discussion and their availability all the time that I need them, and the big encouragement they gave.

I especially thank my beloved friends and familly members, for supporting me during my good and bad moments. They help me all the time with their unconditional love and positive advices, and invocations.

I am deeply thankful to my friend and sister ***Dr.Saoussene CHABOU*** for her help, for the invocations and encouragement in the moments of weakness, during the preparation of this thesis.

Special thanks to my sincere husband, ***Dr.Abdeldjalil BENSTITI*** has been a true and great supporter. He has been non-judgmental of me and instrumental in instilling confi-

dence. He has faith in me and my intellect, even when I felt like digging hole and crawling into on other, because I did not have faith in myself. My endless gratitude goes to My hard-working parents have sacrificed their lives for us. their extreme attention to my education and their extreme emotional support, encouragement, provided unconditional love and care, for their endless support. My mother ***Fatiha ARZANI*** was the first teacher to me, she made me an educated girl in all fields and I did not exceed 8 years: in literature, poetry, languages, geography and history. she made me a very distinguished girl among my colleagues. My father ***Mohamed ALOUI*** was a safety that made me feel like a queen wherever I was . His pride made me confident of myself and I have a high ambition to seek knowledge. I love them so much, and I would not have made it this far without them.
Also thanks so much for my beloved brothers; ***Imad, Yasser, Iyad AbdElmouhaimen*** , and ***Siradj Eddine***. Once I remember being in my life I smile. I'm grateful to my only sister ***Randa*** , she has been my best friend all my life, I thank her for all her advice, support, invocations and encouragement.

I know I always have my family to count on when times are rough.

Contents

Abstract i

Dedication ii

Acknowledgements iii

Contents vi

List of Figures x

List of Tables xv

List of Symbols xvii

List of Publications xix

List of Conferences xx

Introduction 1

1 Backgrounds and literature review 4
1.1 Generalities . . . 4
1.1.1 Semiconductors . . . 4
1.1.1.1 Theory of semiconductors . . . 4
1.1.1.2 $p-n$ junctions . . . 7
1.1.2 Photovoltaic device . . . 9
1.2 Solar cells . . . 9
1.2.1 Solar cell principle . . . 9
1.2.1.1 Function of a solar cell . . . 9
1.2.1.2 Losses in solar cells . . . 11
1.2.1.2.1 Optical losses . . . 11

1.2.1.2.2 Electrical loss . . . 11
1.2.2 Thin-film solar cells . . . 13
1.2.2.1 History of thin film solar cells . . . 13
1.2.2.2 Possible configuration of solar cell . . . 14
1.2.2.3 A material based on friendly and abundant elements in nature . . . 15
1.2.2.4 $p-n$ homojunction solar cells . . . 16
1.2.2.5 Homojunctions and heterojunctions . . . 17
1.3 Metallic oxides . . . 18
1.3.1 Zinc oxide . . . 18
1.3.2 Cuprous oxide . . . 20
1.3.3 $p-Cu_2O/n-ZnO$ heterojunction . . . 20

2 Materials and methods **22**
2.1 Principle and conditions of electrochemical deposition method . . . 22
2.1.1 Electrodeposition . . . 22
2.1.2 Electrochemical approaches of elaboration . . . 24
2.1.2.1 Potentiostatic approach . . . 24
2.1.2.2 Galvanostatic approach . . . 25
2.1.3 Conditions of elaboration . . . 25
2.1.3.1 Substrate preparation . . . 25
2.1.3.2 Electrolyte preparation for the deposition of ZnO nanostructures . . . 26
2.1.3.3 Electrolyte preparation for the deposition of Cu_2O nanostructures . . . 27
2.2 Electrochemical methods . . . 28
2.2.1 Cyclic voltammetry . . . 28
2.2.2 Chronoamperometry . . . 29
2.2.3 Chronopotentiometry . . . 30
2.2.4 Mott-Schottky measurements . . . 30
2.2.5 Photocurrent analysis . . . 32
2.3 Physical characterization instruments . . . 34
2.3.1 Autolab: Potentiostat/Galvanostat . . . 34
2.3.2 Scanning electron microscope (SEM) . . . 35
2.3.3 Atomic Force Microscope (AFM) . . . 36
2.3.4 X-ray diffractometer (DRX) . . . 37
2.3.5 UV-Vis spectrophotometer . . . 38
2.3.6 Stylus profilometer . . . 39
2.3.7 Current-Voltage characterization in the dark (I-V measurement) . . . 40

3 Electrochemical parameters effect on the ZnO nanostructures properties **43**
3.1 Introduction . . . 43
3.2 Galvanostatic electrodeposition of ZnO nanostructures: Current density effect . . . 45
3.2.1 Electrochemical analyses . . . 45

3.2.1.1 Deposition mechanism of ZnO nanostructures 45
3.2.1.2 Mott-scottky Measurements 47
3.2.1.3 Photocurrent analysis 49
3.2.2 Structural characterization 51
3.2.3 Topographical characterization 52
3.2.4 Optical characterization 53
3.3 Galvanostatic, and potentiostatic electrodeposition of ZnO nanostructures: comparative study for two different morphologies 56
3.3.1 Electrochemical analyses 57
3.3.1.1 Deposition mechanism of ZnO nanostructures 57
3.3.1.2 Mott-scottky Measurements 59
3.3.1.3 Photocurrent analysis 60
3.3.2 Structural characterization 61
3.3.3 Optical characterization 64
3.3.4 Morphological characterization 65
3.4 Conclusion 67

4 Electrochemical parameters effect on the Cu_2O nanostructures properties 68
4.1 Introduction 68
4.2 Galvanostatic of Cu_2O nanostructures: Current density effect 69
4.2.1 Electrochemical analyses 70
4.2.1.1 Deposition mechanism of Cu_2O nanostructures 70
4.2.1.2 Mott-scottky Measurements 72
4.2.1.3 Photocurrent analysis 73
4.2.1.4 Electrochemical impedance spectroscopy (EIS) analysis . . 74
4.2.2 Structural characterization 76
4.2.3 Optical characterization 79
4.2.4 Photoelectrochemical (PEC) stability of Cu_2O nanostuctures for water splitting 81
4.3 Galvanostatic, and potentiostatic electrodeposition of Cu_2O nanostructures: comparative study in two different pH 83
4.3.1 Electrochemical study 83
4.3.1.1 Cyclic voltammetry 83
4.3.1.2 Mott-Schottky measurements 85
4.3.1.3 Photocurrent analysis 86
4.3.2 Structural characterization 88
4.3.3 Optical characterization 90
4.3.4 Morphological characterization 91
4.4 Conclusion 94

5 Additives effect on the Cu_2O nanostructures properties 95
5.1 Introduction 95

5.2 Ammonium chloride effect on Cu_2O nanoparticles properties, galvanostaticlly electrodeposited . . . 97
5.2.1 Cyclic voltammetry . . . 97
5.2.2 Morphological characterization . . . 98
5.2.3 Structural characterization . . . 100
5.2.4 Photocurrent analysis . . . 101
5.2.5 The photoelectrochemical (PEC) stability of Cu_2O 26−facet polyhedral particles . . . 103
5.3 Potassium chloride effect on Cu_2O nanoparticles properties, galvanostaticlly electrodeposited . . . 104
5.3.1 Morphological characterization . . . 104
5.3.2 Structural characterization . . . 106
5.3.3 Electrochemical measurements . . . 108
5.3.3.1 Photocurrent analysis . . . 108
5.3.3.2 Mott–Schottky (M–S) measurements . . . 109
5.3.4 Optical characterization . . . 111
5.4 Conclusion . . . 112

6 Potentiostatic and galvanostatic electrodeposition of $p-Cu_2O/n-ZnO_{(NW)}/ZnO^{(g)}_{(NS)}$ heterojunction 114
6.1 Introduction . . . 114
6.2 pH effect as function of the elaboration mode on $p-Cu_2O/n-ZnO^{(p)}_{(NW)}/ZnO^{(g)}_{(NS)}$ heterojunction . . . 116
6.2.1 Deposition mechanism of Cu_2O nanostructures on $n-ZnO^{(p)}_{(NW)}/\ ZnO^{(g)}_{(NS)}$ films . . . 116
6.2.2 Structural characterization . . . 117
6.2.3 Optical characterization . . . 118
6.2.4 Morphological characterization . . . 119
6.2.5 I-V characterization . . . 120
6.3 Elaboration mode effect on $p-Cu_2O/n-ZnO^{(g)}_{(NW)}/ZnO^{(g)}_{(NS)}$ heterojunction . . . 122
6.3.1 Structural characterization . . . 122
6.3.2 I-V characterization . . . 123
6.4 Conclusion . . . 124

Conclusions 125

Bibliography 128

List of Figures

1.1 Band structure at 0°K of: a) insulator, b) semiconductor and c) metal (a metal can have either overlapping bands or partially filled conduction band. 5
1.2 direct and indirect band gaps [32] 5
1.3 Fermi levels for intrinsic, p- doped and n-doped semiconductors. 6
1.4 Formation of the depletion zone within a $p-n$ junction[36] 7
1.5 Energy band diagram of a $p-n$ junction at thermal equilibrium. 8
1.6 a) The $p-$type material has a higher concentration of holes, and the $n-$type material has a higher concentration of electrons. When the two are brought into contact this gives rise to diffusion of carriers, which in turn gives rise to a potential difference across the junction [31]. b) $p-n$ junction diode reverse bias circuit diagram. 8
1.7 Illustration of a PV function 10
1.8 Absorption of different photons by a semiconductor material 10
1.9 Real solar cell with the resistors Rs and R_{sh} 12
1.10 Possible configuration of thin film solar cells. a) superstrate configuration. b) substrate configuration 14
1.11 Relative abundance of the elements. 15
1.12 Band diagram and dark and illuminated I - V characteristics of a $p-n$ homojunction, ZnO based [51]. 16
1.13 A heterojunction between a wide band gap $n-$type window layer and a narrow band gap $p-$type absorber with a discontinuity spike in the conduction band[54]. 18
1.14 The mismatch between the lattices causes dangling bonds at the interface[53]. 18
1.15 ZnO wurtzite structure model with various crystal planes with tetrahedral coordination [67]. 19
1.16 Cu_2O cubic structure model with various crystal planes. 20

2.1 Electrodeposition experimental setup; (1) Three electrodes cell, (2) Potentiostat/galvanostatt (Autolab), (3) Computer, (4) Thermostatic bath . . 23
2.2 Three electrodes cell 23
2.3 Experimental setup under potentiostatic mode 24
2.4 Experimental setup under galvanostatic mode 25

2.5 Cyclic voltammograms recorded in $0.05M$ of $CuSO_4$ at 70 °C, in pH of 11. Potential scan rate is $100mV/s$. (1) and (2) are the oxidation peaks. (3) and (4) are the reduction peaks. (3) corresponds to the formation of Cu_2O 28
2.6 Chronoamperometric curve obtained during the electrodeposition under potentiostatic mode with the different formation steps 29
2.7 Chronopotentiometric curve obtained during the electrodeposition under galvanostatic mode with the different formation steps 30
2.8 Mott–Schottky plots. a) for ZnO thin films ($n-$type semiconductor) , b) for Cu_2O thin films ($p-$type semiconductor). 31
2.9 Photocurrent interaction principle in semiconductor/electrolyte interface . 33
2.10 Circuit diagram of a typical three-electrode potentiostat circuit[107]. 34
2.11 Illustration of a schematic principle of the Scanning Electron Microscope. . 35
2.12 Illustration of the AFM schematic principle 36
2.13 Illustration of the principles behind an XRD. The detector moves and registers the reflected intensity at different angles (2θ). 37
2.14 Illustration of UV-Vis spectrophotometry schematic principle 38
2.15 The schematic principle of a stylus profilometer. 40
2.16 I-V characterization of CZTS/ZnS hetero-junction and the equivalent circuit of an ideal diode. 41
2.17 Semi logarithmic scale of the current as function of applied voltage of a diode. 42

3.1 Chronopotentiograms obtained during deposition of ZnO nanosheets at different current densities: -0.5, -1, -2, -3 $mA.cm^{-2}$ from an electrolyte containing 80 mM $Zn(NO_3)_2$ and 100 mM (KNO_3) at 70 °C for150 $sec.$. 46
3.2 Mott–Schottky plots of ZnO nanosheets at different current densities: -0.5, -1, -2, -3 $mA.cm^{-2}$. The corresponding flat band potential values are indicated for the different plots. 48
3.3 Photocurrent measured from ZnO nanosheets at different current densities: -0.5, -1, -2, -3 $mA.cm^{-2}$. Inset: the variation of the average photoresponse as function of the deposition current density. 50
3.4 XRD patterns of ZnO nanosheets at different current densities: -0.5, -1, -2, -3 $mA.cm^{-2}$ on FTO. (*) Indicate diffraction peaks corresponding to the FTO substrate. 51
3.5 Tapping mode 2D AFM images ($10 \times 10\mu m^2$) of ZnO nanosheets electrodeposited at different current densities: a) -0.5,b) -1, c) -2 and d) -3 $mA.cm^{-2}$. The roughness for each sample was also indicated. 53
3.6 a) Transmittance spectra ZnO nanosheets at the different current densities. b) Dependence of $(\alpha h\nu)^2$ versus photon energy (eV) for ZnO nanosheets. Inset: the variation of the optical gap values as a function of the deposition current density 54
3.7 a) Chronoamperograms and Chronopotentiograms obtained during deposition of ZnO nanosheets b) Chronopotentiograms and Chronoamperograms obtained during deposition of ZnO nanowires from an electrolyte containing $1mM$ $Zn(NO_3)_2$ and $100mM KCl$ at 70 °C for $15min$. 58

3.8 Mott–Schottky plots for ZnO nanostructures elaborate under potentiostatic, and gavanistatic modes. a) nanosheets, b) nanowires. The corresponding flat band potential values are indicated for the different samples 59
3.9 Photocurrent measured from for ZnO nanostructures elaborated under potentiostatic, and gavanistatic modes. a) nanosheets, b) nanowires. 61
3.10 XRD patterns of ZnO nanostructures elaborate under potentiostatic, and gavanistatic modes (a nanosheets, b) nanowires. (*) Indicates diffraction peaks corresponding to the FTO substrates. 63
3.11 Transmittance spectra of the electrodeposited ZnO nanostructures elaborated under potentiostatic, and gavanistatic modes a) nanosheets, b) nanowires. 64
3.12 SEM images of ZnO nanostructures elaborated under potentiostatic, and gavanistatic modes for nanosheets and nanowires; $a_1)$ $ZnO^{(p)}_{(NW)}$, $a_2)$ $ZnO^{(g)}_{(NW)}$, $b_1)$ $ZnO^{(g)}_{(NS)}$, $b_2)$ $ZnO^{(p)}_{(NS)}$. 66

4.1 Chronopotentiograms obtained during deposition of Cu_2O thin films at different current densities: -0.2, -0.3, -0.4 and $-0.5 mA.cm^{-2}$ from an electrolyte containing $0.05M$ $CuSO_4$ and $0.06M$ citric acid, at 70°C during $15min$. 70
4.2 Mott–Schottky plots of Cu_2O thin films at different current densities: -0.2, -0.3, -0.4 and $-0.5 mA.cm^{-2}$. The corresponding flat band potential values are indicated for the different plots. 73
4.3 Photocurrent measured from of Cu_2O thin films at different current densities: $-0.2, -0.3, -0.4$ and $-0.5 mA.cm^{-2}$. 74
4.4 Nyquist plots (Z imaginary versus Z real) measured in $0.5M$ of Na_2SO_4 of Cu_2O thin films at different current densities: $-0.2, -0.3, -0.4$ and -0.5 $mA.cm^{-2}$. 75
4.5 a) XRD patterns of Cu_2O thin films at different current densities: -0.2, -0.3, -0.4 and $-0.5 mA.cm^{-2}$ on FTO. b) Texture coefficients ($I_{(111)}/I_{(200)}$) and $I_{(111)}/(I_{(111)}+I_{(200)})$) as a function of the applied current density. (111) and (200) are the main diffraction peaks from the deposited Cu_2O nanostructures. c) The roughness as function on the applied current density. . . 77
4.6 a) Transmittance spectra of Cu_2O nanostructures at different current densities: $-0.2, -0.3, -0.4$ and $-0.5 mA.cm^{-2}$. b) Absorbance spectra of the different Cu_2O nanostructures. c) Dependence of $(\alpha h\nu)^2$ versus photon energy (E_{ph}) (eV) for Cu_2O thin films. d) The corresponding absorption coefficient. 79
4.7 Photoelectrochemical (PEC) water splitting measurements of Cu_2O nanostructures at different current densities (-0.2, -0.3, -0.4 and $-0.5\ mA.cm^{-2}$), in distilled water, applied potential is $-0,5\ V/SCE$ for 20 minutes. . . . 82
4.8 Cyclic voltammograms recorded in 0.05M of $CuSO_4$ at 70 °C, in pH of 11 and 12. 84
4.9 Mott–Schottky plots for Cu_2O thin films elaborated under potentiostatic, and gavanistatic modes a) bath pH=11, b) bath pH=12. The corresponding flat band potential values are indicated for the different samples. 86

4.10 Photocurrent measurements of Cu_2O thin films grow under potentiostatic, and gavanistatic modes. a) bath pH=11, b) bath pH=12. 87
4.11 XRD patterns of Cu_2O thin films elaborate under potentiostatic, and gavanistatic modes (a pH 11, b) pH 12. (*) Indicate diffraction peaks corresponding to the FTO substrates. The corresponding texture coefficients: c) $(I_{(111)}/I_{(200)})$. d) $I_{(111)}/(I_{(111)} + I_{(200)})$. (111) and (200) are the main diffraction peaks from the Cu_2O films. The line in the graph shows the intensities ratio according to the (JCPDS no. 00-005-0667). 89
4.12 Absorption coefficient spectra of Cu_2O thin films elaborate under potentiostatic, and gavanistatic modes. a) bath pH=11. Inset. The corresponding dependence of $(\alpha h\nu)^2$ versus photon energy (eV). b) bath $pH = 12$. Inset. The corresponding dependence of $(\alpha h\nu)^2$ versus photon energy (eV). 90
4.13 Tapping mode 2D AFM images ($10 \times 10\mu m^2$) of Cu_2O thin films. a) $Cu_2O^{(11)}_{(p)}$ b) $Cu_2O^{(11)}_{(g)}$ c) $Cu_2O^{(12)}_{(p)}$ d)$Cu_2O^{(12)}_{(g)}$. 92
4.14 SEM images of of Cu_2O thin films. a) $Cu_2O^{(11)}_{(p)}$ b) $Cu_2O^{(11)}_{(g)}$ c) $Cu_2O^{(12)}_{(p)}$ d)$Cu_2O^{(12)}_{(g)}$ 93

5.1 Cyclic voltammogram recorded in $0.003M$ of $Cu(NO_3)_2$ and $0.1M$ of KCl at 70 °C, and in the same conditions with addition of $0.0015M$ Of NH_4Cl. Potential scan rate is $100mV/s$. 98
5.2 SEM images of the Cu_2O particles. a, b, c, d) without NH_4Cl. e, f, g, h) with $0.0015M$ NH_4Cl. 99
5.3 a) XRD pattern of Cu_2O nanoparticles electrodeposited on FTO substrate with and without NH_4Cl. (*) Indicate diffraction peaks corresponding to the FTO substrate.b) Zoom of XRD spectra of obtained films at different diffraction peak regions 101
5.4 a) Photocurrent measured from Cu_2O nanoparticules. For the measurement, the applied potential is $0V/SCE$. The solution contains 0.5 M Na_2SO_4. The sample was illuminated with a 500 W white-light source. b) with $0.0015MNH_4Cl$. 102
5.5 Photoelectrochemical (PEC) water splitting measurements, applied potential is $-0,5V/SCE$ in distillate water. 103
5.6 SEM images of the Cu_2O nanostructures (a) without KCl (b) 0.001M KCl (c) 0.1M KCl. In the corner of each image, a higher magnification of the respective nanostructures is shown. 105
5.7 a) XRD patterns of Cu_2O nanostructures electrodeposited on FTO without and with different concentrations of KCl. b) Texture coefficients: b_1) f parameter of X-ray diffraction peaks as a function of the concentrations of KCl. $b2$) $I_{(111)}/I_{(200)}$) as a function of the concentrations of KCl. (111) and (200) are the main diffraction peaks from the Cu_2O films. 107
5.8 Photocurrent measured from Cu_2O nanostructures deposited , without KCl, with $0.001MKCl$ and $0.1MKCl$. 109
5.9 Mott–Schottky plots for Cu_2O nanostructures deposited (a) without KCl, (b) with $0.001MKCl$, (c) with $0.1MKCl$. The corresponding flat band potential values are indicated for the different plots. 110

5.10 a) Absorbance spectra of the electrodeposited Cu_2O nanostructures without and with different concentrations of KCl. b) The Tauc plots as function of the the KCl concentration. 112

6.1 Processing steps for the fabrication of $p-Cu_2O\Big/n-ZnO^{(p)}_{(NW)}\Big/ZnO^{(g)}_{(NS)}$ and $p-Cu_2O\Big/n-ZnO^{(g)}_{(NW)}\Big/ZnO^{(g)}_{(NS)}$ heterojunctions for solar cell application. 115

6.2 a) Schematic design of the sythesized $p-Cu_2O/n-ZnO_{(NW)}/ZnO^{(g)}_{(NS)}$ heterojunction. b) Energitic diagram before and after contact 116

6.3 a) Chronoamperograms obtained during deposition of Cu_2O thin films on $n-ZnO^{(p)}_{(NW)}/ZnO^{(g)}_{(NS)}$ at 70 °C and different pH media during $15min$, from an electrolyte containing $0.05M$ $CuSO_4$, $0.06M$ citric acid,and $NaOH$ to adjust the pH b) The correponding Chronopotentiograms in identical conditions. 117

6.4 a) XRD pattern of ZnO nanowires electrodeposited potentiostatically. b) XRD pattern of the obtained $p-Cu_2O/n-ZnO^{(p)}_{(NW)}/ZnO^{(g)}_{(NS)}$ heterojunctions 118

6.5 a) Absorbance spectra of the electrodeposited Cu_2O nanostructures within different pH media and under different deposition approches. b) Absorbance spectra of the corresponding $p-Cu_2O/n-ZnO^{(p)}_{(NW)}/ZnO^{(g)}_{(NS)}$ heterojunctions 119

6.6 SEM images of a)Joc1, b)Joc2, c)Joc3, and d) Joc4. 120

6.7 Current density–voltage characteristics of $p-Cu_2O/n-ZnO^{(p)}_{(NW)}/ZnO^{(g)}_{(NS)}$ heterojunctions in the dark. Inset of the figure illustrates the corresponding heterojunction design. 121

6.8 a) XRD pattern of ZnO nanowires electrodeposited galvanostatically. b) XRD pattern of the obtained $p-Cu_2O/n-ZnO^{(g)}_{(NW)}/ZnO^{(g)}_{(NS)}$ heterojunctions 122

6.9 Current density–voltage characteristics of $p-Cu_2O/n-ZnO^{(g)}_{(NW)}/ZnO^{(g)}_{(NS)}$ heterojunctions in the dark. 123

List of Tables

2.1 Different chemical species used within the electrolytes to grow ZnO nonosheets and ZnO nanowires. . . . 27
2.2 Different chemical species used within the electrolytes to grow Cu_2O nanostructures and Cu_2O nanoparticles. . . . 28

3.1 Current density effect $(-0.5, -1, -2, -3 mA.cm^{-2})$ of ZnO nanostructures on the donor density charge (N_D), the flat band potential(E_{fb}), the depletion zone thickness (W), and the effective density of states in the conduction band $(E_{cb} - E_F)$. . . . 49
3.2 Current density effect $(-0.5, -1, -2, -3\ mA.cm^{-2})$ of ZnO nanostructures on the transmittance in different optical domains. . . . 55
3.3 Current density effect $(-0.5, -1, -2, -3\ mA.cm^{-2})$ of ZnO nanostructures on the physical and electrochemical properties. . . . 56
3.4 Mode effect on the donor density charge and the flat band potential of ZnO nonosheets and ZnO nanowires. . . . 60
3.5 Mode effect on the film thickness, and structural properties of ZnO nonosheets and ZnO nanowires. . . . 63

4.1 Current density effect $(-0.2, -0.3, -0.4$ and $-0.5 mA.cm^{-2})$ on the growth parameters of Cu_2O nanostructures. . . . 71
4.2 Current density effect $(-0.2, -0.3, -0.4$ and $-0.5\ mA.cm^{-2})$ on the electrical properties of Cu_2O nanostructures. . . . 76
4.3 Current density effect $(-0.2, -0.3, -0.4$ and $-0.5 mA.cm^{-2})$ on the structural properties of Cu_2O nanostructures. . . . 78
4.4 Current density effect $(-0.2, -0.3, -0.4$ and $-0.5 mA.cm^{-2})$ on the optical properties of of Cu_2O nanostructures. . . . 81
4.5 Current density effect $(-0.2, -0.3, -0.4$ and $-0.5 mA.cm^{-2})$ on the Photoelectrochemical (PEC) stability of Cu_2O nanostructures for water splitting application. . . . 83
4.6 Mode effect on the structural properties of Cu_2O nonostructures. . . . 89
4.7 Mode effect on the optical properties of Cu_2O nonostructures 91

5.1 KCl's concentration effect on the structural properties of Cu_2O nanostructures. . . . 108
5.2 KCl concentration effect on the charge density of Cu_2O nanostructures. . . . 111

6.1 Different designs of the elaborated heterojunctions based on ZnO and Cu_2O nanostructures. 115

List of Symbols

E_g	Gap energy
E_F	Fermi level
V_{oc}	Open circuit voltage value
PV	Photovoltaic
FTO	Polycrystalline fluorine-doped tin oxide
C	Space charge capacitance
e	Electron charge
N_D	Donor concentration
ϵ_0	Vacuum permittivity
ϵ	Dielectric constant
K	Boltzmann constant
E	The applied potential
E_{fb}	Flat-band potential
N_A	Acceptor concentration
e^-/h^+	Electron-hole pair
D	The average crystallite size
λ	The wavelength
β	Full width at half maximum (FWHM)
α	The absorption coefficient
L	The optical path (in our case is the film thickness)

T	The transmittance
R	The reflectance
A	The absorbance
$h\nu$	photon energy
I_s	Saturation current
q	Elementary electronic charge
N_c	Effective density of states in the conduction band
m^*	Electron effective mas
W	Depletion zone thickness
RMS	Root mean square
$ZnO^{(g)}_{(NS)}$	ZnO Nanosheets by galvanostatic mode
$ZnO^{(p)}_{(NS)}$	ZnO Nanosheets by potentiostatic mode
$ZnO^{(g)}_{(NW)}$	ZnO Nanowires by galvanostatic mode
$ZnO^{(p)}_{(NW)}$	ZnO Nanowires by potentiostatic mode
$Cu_2O^{(11)}_{(p)}$	Cu_2O Nanostructures elaborated in pH=11 under potentiostatic mode
$Cu_2O^{(11)}_{(g)}$	Cu_2O Nanostructures elaborated in pH=11 under galvanostatic mode
$Cu_2O^{(12)}_{(p)}$	Cu_2O Nanostructures elaborated in pH=12 under potentiostatic mode
$Cu_2O^{(12)}_{(g)}$	Cu_2O Nanostructures elaborated in pH=12 under galvanostatic mode

List of Publications

1. **M. Aloui**, L. Mentar, A. Beniaiche, and A. Azizi, "Electrochemical and physical properties of zno nanosheets and ZnO nanowires, under different applied current densities and deposition approaches," Applied Physics A, vol. 128, no. 4, pp. 1–14, 2022.

2. **M. Aloui**, L. Mentar, A. Beniaiche, and A. Azizi, "NH_4Cl and KCl effect on the structural, morphological, optical and electrochemical properties of Cu_2O nanoparticles and Cu_2O nanostructures, galvanostatically electrodeposited," Journal of Solid State Chemistry, p. 123435, 2022.

List of Conferences

International

1. **Meriem Aloui**, Ouidad Baka, Halla Lahmar and Loubna Mentar. "Elaboration of n-type Cu_2O Nanostructures for Heterojuction solar cell Applications", CEE'9, poster communication, Batna university, October, 02-04, 2016

2. **Meriem Aloui**, Halla Lahmar,Loubna Mentar and Abdelkarim Beniaiche. " Elaboration et caractérisation des couches de ZnO et Cu_2O pour une application photovoltaïque", ICO2016, poster communication, setif university, December, 04-05, 2016.

3. **Meriem Aloui**, Ibrahim Yaacoub Bouderbala, Halla Lahmar and Loubna Mentar. "Electrodeposition and caracterisation of Cu_2O nanostructures for photovoltaic application", ENTECH'16, poster communication, Istanbul university, December, 15, 2016.

4. Abdelmadjid Herbadji, Ibrahim Yaacoub Bouderbala, **Meriem Aloui** and Loubna Mentar. "Electrochemical deposition of Cu_2O thin films for solar cell application", ICAS, poster communication, Istanbul university, september, 13-15, 2017.

5. Loubna Mentar, Ibrahim Yaacoub Bouderbala,**Meriem Aloui**, Abdelmadjid Herbadji and Amor Azizi. "Electrochemical growth of Zinc and cuprous oxides nanostructures", ACRICE'3, oral communication, setif university, October, 08-11, 2017.

National

1. **Meriem Aloui** and Loubna Mentar "Galvanostatic electrodeposition and characterization of ZnO nanosheets for optoelectronic application", EAME 2016, poster communication, setif university, November, 27-28, 2017.

Introduction

We cannot solve our problems
with the same thinking we used
when we created them
"Albert Einstein"

THE renewable energies include the conversion of sunlight, wind, nuclear power and thermal earth heat into electric energy which could meet the most needs of energy in the world. In 1952 four thousand people died in London because of the high concentration of pollution [1]. Recently in 2012 the World Health Organization (WHO) reported around 7 million of people died because of air pollution exposure [2]. The air pollution became the biggest environmental health risk in the world. The solar energy is unlimited and environmentally friendly, direct conversion of solar energy into electric energy using photovoltaic devices is considered as an ideal solution to reduce the abasement of the climate. In the other hand, the advances that have been made in the miniaturization field of electronics and optoelectronic devices have far outpaced the corresponding development within the use of renewable energy sources. The most suitable candidate materials to achieve this purpose are earth-abundant metal oxides semiconductors. So far, they possess a wide range of properties which make them preferred for many applications; such as photovoltaics[3–5], organic reaction catalyst [6, 7], water splitting under visible light [8], solar energy conversion [9], metal-insulator-metal resistive switching memory[10], chemical template [11], and negative electrode material for lithium-ion battery [12]. Among

them, are ZnO and Cu_2O; ZnO is an n-type semiconductor with high electron mobility, a large gap of $3.3eV$ [13], and a relatively high exciting binding energy of $59meV$. Furthermore, the ZnO emission range is in the near ultraviolet at ambient temperature. Cuprous oxide Cu_2O is an abundant, nontoxic, and low-cost[14, 15] semiconductor. It is generally exhibits p-type conductivity [16–18] , with direct band gap ($Eg = 2.0eV$) [19]. The Cu_2O remains an interesting alternative to various metal oxide semiconductors thanks to the high theoretical efficiency of Cu_2O based solar cell (18–20% [20]). Whereby, in recent years, electrochemical deposition has taken the attention of scientists, which offers excellent possibilities for controlling the properties of the deposited material. In which, many efforts have been made to use its advantages; making large-area films using chemical solutions at low-temperature [21]. So that, electrochemical deposition is considered the easiest and the least expensive method for the deposition of high quality films, which could be used for device applications. It is an interesting technique that provides a facile control of critical parameters such as the deposition current, potential, temperature, precursor concentration, and pH. The electrodeposition process can be carried out either potentiostatically or galvanostatically, involving respectively, applied constant potential where a current density varying with time during the film growth or applied constant current density where a potential varying with time. The main advantage with the potentiostatic approach is that, the film morphology can be determinate naturally. Whoever, the rate of the deposition can be precisely controlled in the galvanostatic mode. Whereas, the potentiostatic mode is the preferred generally. Since 2010, galvanostatic mode has taken attention of scientists to control different morphologies for such materials: CdS/SnS heterostructure [22], aluminium nano-rods[23], ZnO thin films[24], Carbon nanotube [25], bismuth telluride thin films[26], Bi_2O_3 [27], Manganese Oxide [28], Cu_2ZnSnS_4 thin film[29], cadmium telluride films [30]. It's worthnoting that the Galvanostatic approach makes the electrodeposition more simple and effective, thanks to the elimination of the reference electrode. To date, there is consequently very little information regarding the influence of the current density on the structural and the morphological properties of deposits.

The Ph.D. project focuses on enhancing the features of ZnO and Cu_2O elaborated through

electrochemical deposition. In order to achieve this goal, we implemented many strategies to study the key parameters effect on the electrochemical, structural, optical, and morphological properties of the synthesized nanostructures. The thesis manuscript is organized as follows:

Chapter 1 presents an introduction to the basics of semiconductors, $p-n$ junctions and devices. In particular, a literature review on ZnO and Cu_2O properties and Cu_2O/ZnO heterojunction development limitation.

Chapter 2 presents, as a first part, the electrodeposition principle and its conditions of elaboration, as a second part, the different methods and the experimental conditions followed to grow ZnO and Cu_2O. Finally, we show the electrochemical and physical instruments used to characterize the synthesized ZnO and Cu_2O nanostructures, as well as the working principle of each method.

Chapter 3 studies, as a first part, the current density effect on ZnO nanosheets formed through electrochemical deposition. Where the films are elaborated galvanostatically in a nitrate solution. And as a second part, the mode effect onto the ZnO nanosheets ($ZnO_{(NS)}$) and ZnO nanowires ($ZnO_{(NW)}$).

Chapter 4 studies, as first part, the current density effect on the Cu_2O nanostructures using electrodeposition through the galvanostatic approach, as a second part, the effect of the elaboration mode within two different pH media.

Chapter 5 studies, the additives effect on the Cu_2O properties. As first part, we study the Ammonium chloride (NH_4Cl) effect on Cu_2O nanoparticles. As second part, we study the potassium chloride (KCl) on the Cu_2O nanostructures.

Chapter 6 proposes, as application of the synthesized ZnO and Cu_2O nanostructures, an architecture design of $p-n$ heterojunction
($p-Cu_2O\big/n-ZnO_{(NW)}\big/ZnO_{(NS)}$). Where, we present a comparative study in order to investigate the mode and pH effects on the heterojunction performance.

The thesis is resumed by a general conclusion and future perspectives.

Chapter 1

Backgrounds and literature review

1.1 Generalities

1.1.1 Semiconductors

1.1.1.1 Theory of semiconductors

EVERY atom has different discrete energy states, and from the pauli exclusion principle two electrons can not be in the same state at the same time. When many atoms are brought together in a solid, continuous bands are formed by the adjusted energy levels with a forbidden band between them. At 0°K an insulator or semiconductor has a band structure where a completely empty conduction band is separated from a filled valence band by the forbidden gap, see Fig. (1.1) [31]. When the allowed energy states are plotted against the wave vector ($\overrightarrow{k}$)-space the lowest excitation energy is between the lowest point in the conduction band and the highest point in the valence band. When these points are located at the same place along the k-axis, it is called a direct band gap, while when they are not, it is called an indirect band gap. Direct band gaps are associated with optical transistions, because photon momentum is very small.

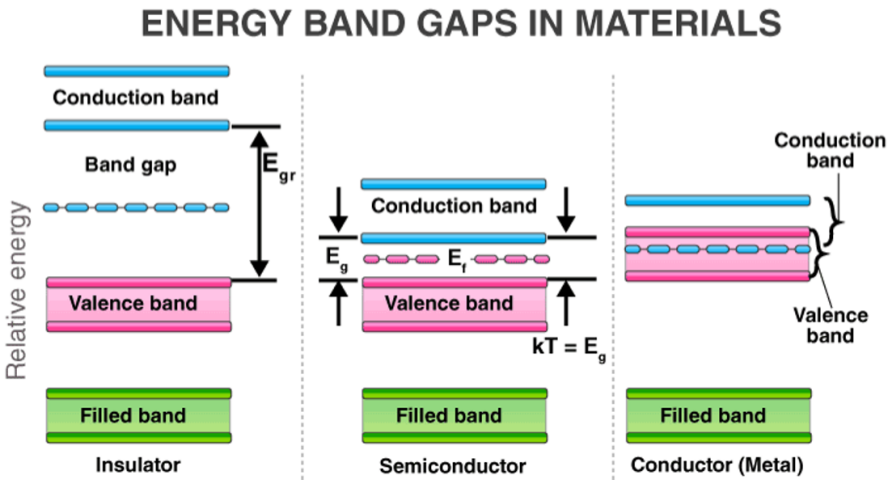

Figure 1.1: Band structure at 0°K of: a) insulator, b) semiconductor and c) metal (a metal can have either overlapping bands or partially filled conduction band.

In an indirect band gap material, a phonon (carrying momentum) is required for transition between the bands, as shown in Fig. (1.2). A phonon also carries energy. The electron may go via a defect state within the band gap to get to the appropriate position for direct excitation/recombination; this state is called a virtual state, and the electron waits in this state for a phonon of the right energy.

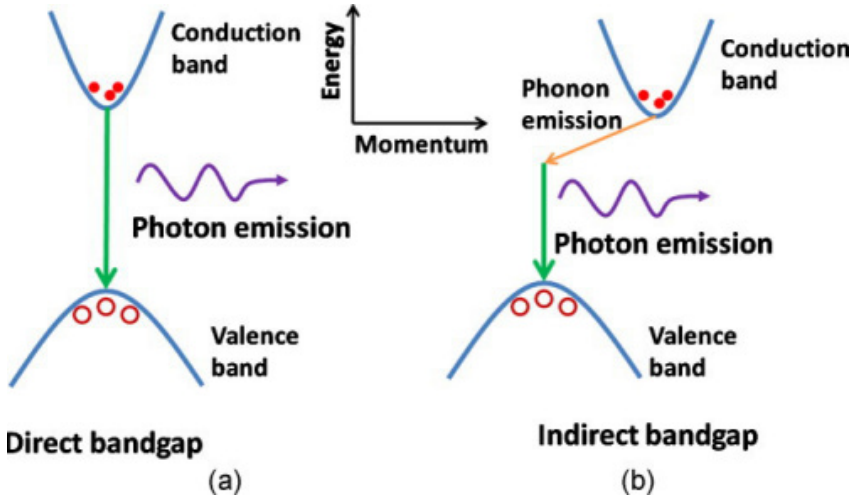

Figure 1.2: direct and indirect band gaps [32]

The two-step excitation process decreases the transition probability compared to a direct band gap one-step transition [33], thus decreasing the optical response of the ma-

terial. A semiconductor is like an insulator, but with a smaller band gap, typically less than $3eV$. An undoped semiconductor is called intrinsic. By insertion of impurities, a semiconductor can be doped, creating an extrinsic semiconductor [34].

The Fermi level is the potential energy level where a (hypothetical) electron state would have a 50% probability of being occupied at thermal equilibrium. Where its position is shown in Fig. (1.3).

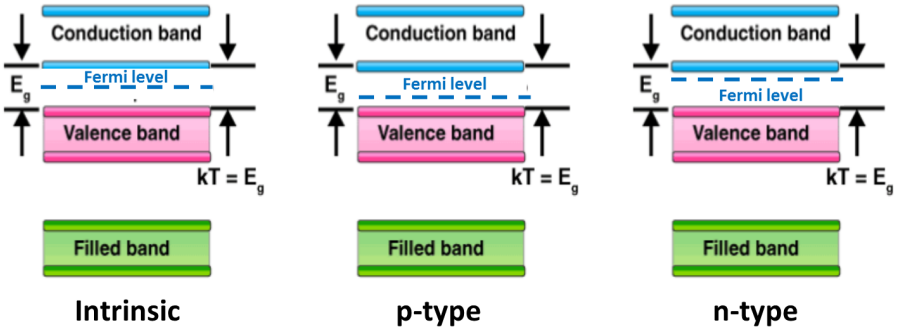

Figure 1.3: Fermi levels for intrinsic, p- doped and n-doped semiconductors.

For an intrinsic semiconductor the Fermi level is in the middle of the band gap, as the number of occupied states in the conduction band equals the number of unoccupied states in the valence band. If the semiconductor is doped, the concentration of holes in the valence band or of electrons in the conduction band can be made higher. The two types of doping are called $p-$ and $n-$doping, respectively. The p-side is a semiconductor doped with a material with fewer occupied electron states than the original material (e.g. B in Si), which gives rise to free electron states called "holes". A hole moves by being occupied by a neighboring electron, leaving an empty state behind in the electron's previous location (now a hole). $n-$type material is created by doping the semiconductor with a material with one more occupied electron state (e.g. P in Si). Electrons move by occupying neighboring unoccupied states. This means that a $p-$type material has high a concentration of mobile holes in the valence band and a low electron concentration in the conduction band while the opposite is true for an $n-$type material. The $p-$ and $n-$ type materials are however not electrically charged [31]. Some materials are spontaneously $n-$

or $p-$type due to structural defects acting as dopants, for example is ZnO $n-$type because of Zn interstitials and O vacancies [35]. The Fermi level moves closer to the valence band when the material is $p-$doped, and closer to the conduction band for a $n-$ doped material to compensate for the doping-induced changes in concentration of occupied states [31].

1.1.1.2 $p-n$ junctions

A $p-n$ junction is the juxtaposition of $n-$type and $p-$type semiconductors, because of the gradient of majority carrier's concentration the holes from the p-side diffuse to the n-side and the electrons from the $n-$side diffuse to the $p-$side. This gives rise to a diffusion current across the junction. When an electron diffuses from the $n-$side to the p-side, an ionized donor is left behind on the $n-$side, which is immobile. Similarly, when a hole goes from the $p-$side to the $n-$side, an ionized acceptor is left behind in the $p-$side. Thus, the created zone without mobile carriers (ionized atoms) is called the space charge region (SCR) or depletion zone as seen in Fig. (1.4).

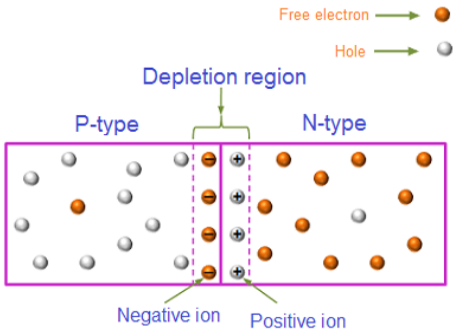

Figure 1.4: Formation of the depletion zone within a $p-n$ junction[36]

Holes diffuse from the $p-$type material into the $n-$type material and electrons from the $n-$type into the $p-$type material. The diffusion causes the regions closest to the junction on both sides to be electrically charged. This difference in charge in turn gives rise to an electric field across the junction. The electric field then counters the diffusion caused by difference in hole and electron concentration. The diffusion of carriers does not stop until the drift current balances the diffusion current, thereby reaching thermal equilibrium as indicated by an alignment of Fermi level (E_F) which induces a curvature

of the bands as well as a potential barrier VD as seen Fig. (1.5). And the illustration of this process is shown in Fig. (1.6)

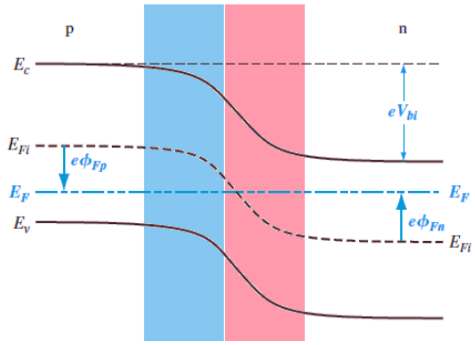

Figure 1.5: Energy band diagram of a $p-n$ junction at thermal equilibrium.

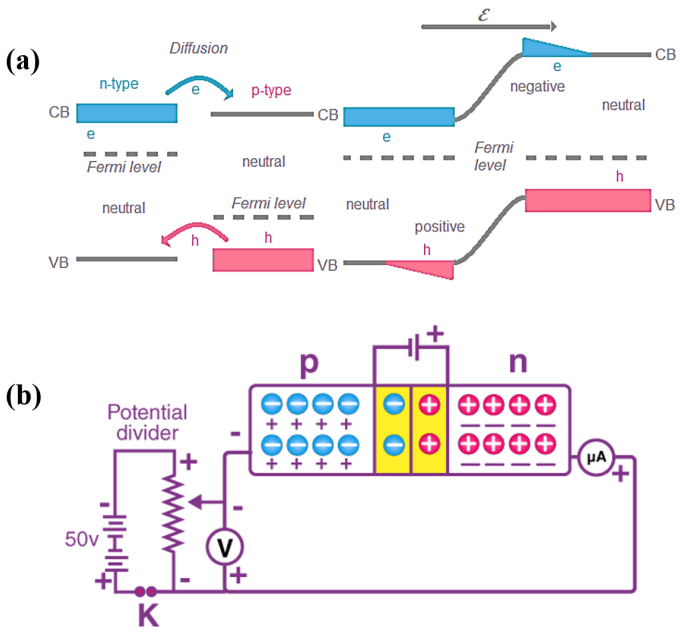

Figure 1.6: a) The $p-$type material has a higher concentration of holes, and the $n-$type material has a higher concentration of electrons. When the two are brought into contact this gives rise to diffusion of carriers, which in turn gives rise to a potential difference across the junction [31]. b) $p-n$ junction diode reverse bias circuit diagram.

The Fermi levels align, because when there is thermal equilibrium which can only be one Fermi level. Thus a junction is formed. A homojunction is a junction where the $p-$ and $n-$sides are the same material, and a heterojunction is a junction where they are of different materials [31].

1.1.2 Photovoltaic device

The photovoltaic device (or The solar cell) is one of the technologies that allow us to convert the enormous amount of solar energy directly into electricity. Therefore, the solar cell acts like a diode in dark and generates photo-voltage under illumination without the influence of any external voltage source. In principle, a solar cell is a junction device obtained by placing two electronically different materials together with a thin electronic barrier in between, to separate charges [37]. The photovoltaic conversion occurs under the light through three successive processes [38]:

1. The semiconductor absorbs the light and converts the photons to electron-hole pairs.

2. The collection and the separation of these carriers by an internal electric field ($p-n$ junction).

3. The distribution of electricity to an external load.

1.2 Solar cells

1.2.1 Solar cell principle

1.2.1.1 Function of a solar cell

A solar cell is a device in their function principal it uses photovoltaic effect to convert the sun radiation into electricity when it is exposed directly to light (Fig. (1.7)).

The production of electricity by PV photovoltaic system follows three mechanisms:

1. Absorption of photons Solar radiation is an electromagnetic wave that can be assimilated to particles (photons) whose energy is inversely proportional to the associated wave length. The absorption of these photons is done by a semiconductor, called an absorber, having the capacity to absorb the energy ($h\nu$) of the incident photons of energy greater than or lower to the energy of its gap (Eg).

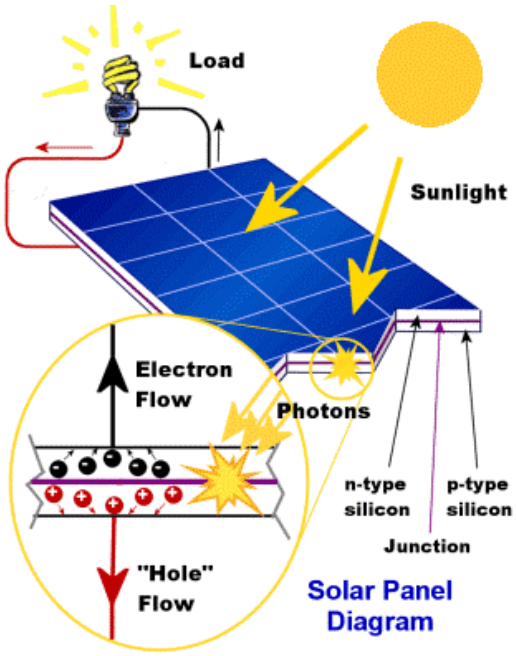

Figure 1.7: Illustration of a PV function

The loss of energy in the absorber, known by Queisser Schottky limit is due to: •If $h\nu \geq Eg$: the energy of the incident photons is enough to excite the electrons of the valence band and make them pass to the conduction band leaving a hole behind them. The remaining energy $(h\nu - Eg)$ is lost by thermalization of the electron in the conduction band $\sim$ 47%, which has the effect of heating the material •If $h\nu < Eg$: the energy of the incident photons is less than the energy of the band gap (Eg) of the material so the excited electrons can't jump the forbidden band and remain in the valence band. The transmission loss of lower photon energy $\sim$ 18%. As shown in Fig. (1.8)

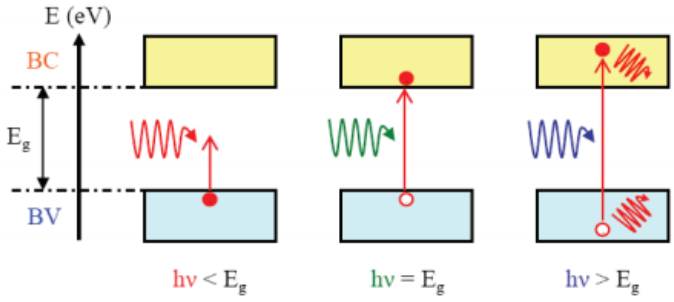

Figure 1.8: Absorption of different photons by a semiconductor material

2. Separation of charges: The separation of free charges (electrons and holes) and

their extraction towards the collecting electrodes is achieved by $p-n$ junction as described before.

3. Collection of porter: The electric field in the space charge region will separate the photo-generated carriers in this zone and extract them to the zone of majority carriers, where the probability of recombination is very low. The generated charges are collected and injected into an external circuit via the conductive electrodes.

1.2.1.2 Losses in solar cells

In a solar cell many reasons can cause the loss in their performance such as optical or electrical losses as described below:

1.2.1.2.1 Optical losses are due to non-absorption, thermalization, reflection, and transmission. The non-absorption happens when the energy of the incident photon is lower than the gap energy of the absorber material.

1. Thermalization: When the coming photon energy is greater than the gap energy of the absorber, the excess energy is dissipated as heat, this heat increases the temperature of the solar cell which increases the reverse saturation current due to the increase in carriers concentration and diffusion length of minority carriers which caused a decrease of the open circuit voltage value (V_{oc}) [39].

2. Reflection loss: The reflection is due to the blocking of the light by the top contact, reflection from the top surface and reflection from the back contact without proper absorption [40].

3. Transmission loss: This is due to the small thickness of cell and the low absorption coefficient of the absorber layer.

4. Area loss: This loss is due to metal grid design or by metal electrode coverage [41]. These type of optical losses can be reduced by using an antireflective coating (ARC) of quarter wavelength thick on the top surface.

1.2.1.2.2 Electrical loss are due to Collection losses, Recombination losses, Series resistance (R_s)

1. Collection losses: These losses are due to surface and bulk recombination at metal or

semiconductor contact and recombination in depletion region. These recombination losses mainly affect the open circuit voltage. Impurities, crystalline defects and incomplete chemical bond on semiconductor acts as traps for photo-excited carriers, and recombination on these traps cause the reduction of photocurrent. The reduction in the concentration of impurities and defects can increase the diffusion length of minority carriers and this can decrease the recombination losses in a solar cell [42].

2. Recombination losses: can be reduced by creating a heavily doped metallic region which acts as back contact, by chemical treatment of the materials or by using a thin layer of passivating oxides.

3. Series resistance (R_s): The Photovoltaic cell is never perfect. To properly translate the behavior of a cell PV, two resistors are added on the equivalent diagram (Fig. (1.9)). The first important lost in solar cells is because of the series resistance which regroups the back and front metal contacts resistances, the semiconductors bulk resistances and the interfaces resistance. To obtain a high record efficiency the series resistance must be as low as possible because of their negative effect on the photo-generated current.

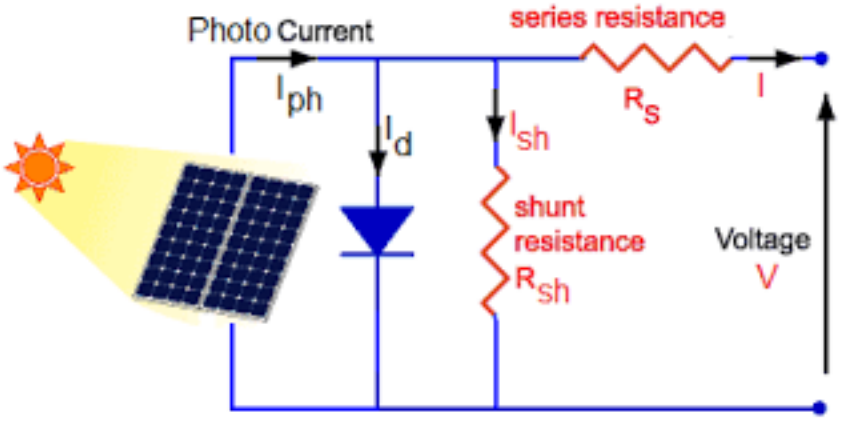

Figure 1.9: Real solar cell with the resistors Rs and R_{sh}

4. Shunt resistance (R_{sh}) The second and important loss in solar cell is due to the shunt resistance (R_{sh}) which is due mainly to the presence of defects in the bulk of semiconductors and at interfaces. It is estimated from the reverse bias of the $I-V$ characteristics. Shunt resistance reduces the open circuit voltage (V_{oc}). It should be as high as possible in order to prevent losses[43] which arerecognized in parallel with the diode and the generated current as seen in Fig. (1.9).

1.2.2 Thin-film solar cells

A thin-film solar cell ($TFSc$) is the name given to the second generation of solar cells, which is realized by the deposition of one or more thin layers of photovoltaic material on a substrate (glass, plastic or metal). Thin-film solar cells are commercially used in several technologies, including amorphous thin-film silicon ($a-Si, TF-Si$), cadmium telluride ($CdTe$), and copper indium gallium selenide ($CIGS$). In this technology of solar cells, the film thickness varies from a few of nanometers (nm) to tens of micrometers (μm), different to the first generation of solar cell which uses silicon wafers with a thickness up to 200 μm, the other drawback of silicon is their indirect band gap energy, however the probability of absorption of a photon is much lower than the semiconductor with direct band gap energy, whereas semiconductor used in thin film solar cells have direct band gap energy and characterized by a high absorption coefficient, and low cost of fabrication.

1.2.2.1 History of thin film solar cells

In 1963, Cusano reported 6% efficiency polycrystalline thin-film solar cells consisting of $Cu_{2-x}Te-CdTe$ hetero-junctions [44]. In 1969 Andirovich et al. reported a thin-film solar cell consisting of a hetero-junction between $n-$type CdS and $p-$type CdTe which was deposited on SnO_2-coated glass [45]. Even though, the efficiency of this cell was only 1% at that time. In 1974, Wagner et al. fabricated a heterojunction for photovoltaic application, it consisted of an $n-$type CdS window layer which was vacuum-deposited on a $p-$ type $CuInSe_2$ single crystal. In the following year, the same group reported a solar cell which had the same hetero-structure and exhibited a high value of efficiency about 12% [46]. In 1976 Kazmerski et al. developed the first thin-film solar cell consisting of $CuInSe_2$ with an efficiency of $4-5\%$ [47]. In 1978 Konagai et al. developed a 13.5% efficiency solar cell consisting of an $n-$type (Ga, Al) As $/p-$type $GaAs$ hetero-junction [48]. Recent progression $CZTS$ based thin-film solar cell technology is remarkable, despite the fact that the semiconducting properties of $CZTS$ and its photovoltaic effect were not known of until 1988. Gunawan and coworkers at IBM Thomas J. Watson Research Center have succeeded in achieving over 10% efficiency CZT (S, Se) thin-film solar cells using

solution-based processing in this decade [49, 50].

1.2.2.2 Possible configuration of solar cell

A thin film solar cell has two possibilities of fabrication from top to down or down to top. the two configurations are called superstrate and substrate as seen in Fig. (1.10).

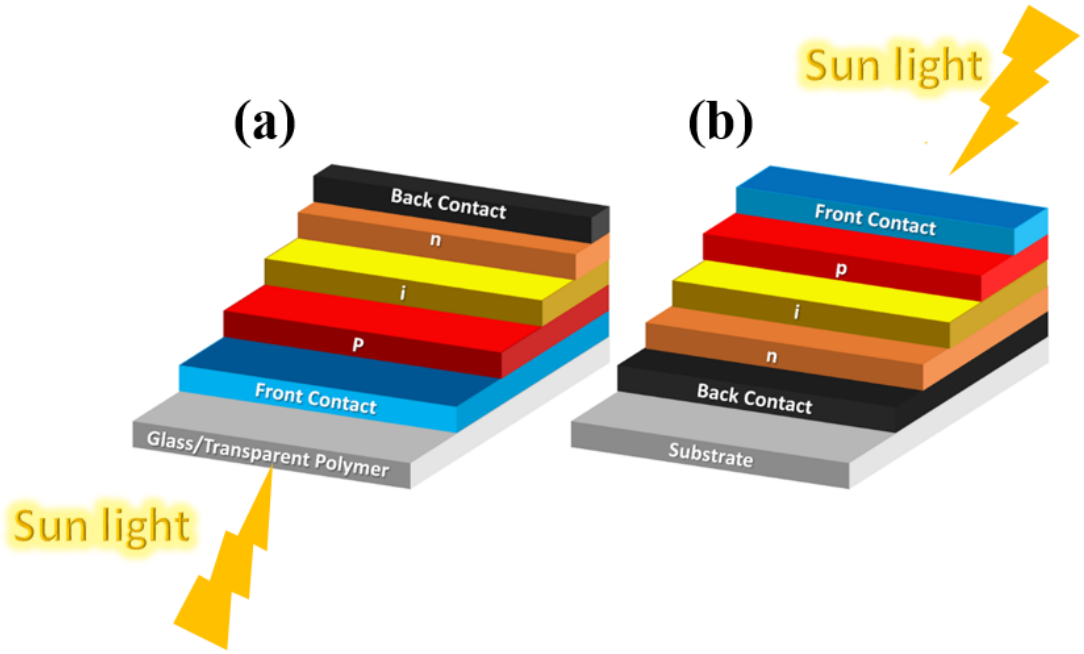

Figure 1.10: Possible configuration of thin film solar cells. a) superstrate configuration. b) substrate configuration

The different between them is that, in superstrate configuration the light goes through the superstrate material before reaching the $p-n$ junction, while in substrate configuration the light reaches the $p-n$ junction without going through the substrate so why we can use different type of substrate, this is the advantage of the first configuration on which we can use different types of substrate.

1.2.2.3 A material based on friendly and abundant elements in nature

CZTS is a metallic chalcogenide composed of copper (Cu), zinc (Zn) tin (Sn), and sulfide (S). Fig. (1.11) illustrate the content and the world trading price of the elements used for thin film solar cells.

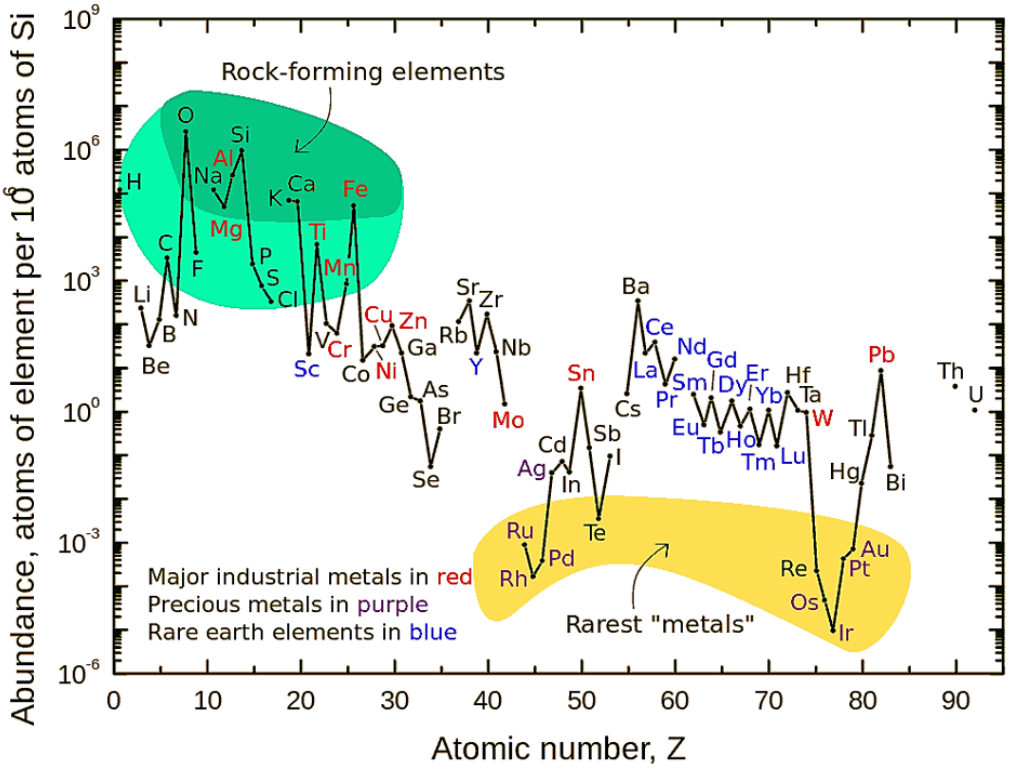

Figure 1.11: Relative abundance of the elements.

These elements are widely present in the earth's crust, particularly in contrast to the indium and gallium compounds that form the $CIGS$. The indium (In) is a rare element with an estimated abundance in the earth's crust making it a very expensive metal. Gallium (Ga) is a metal difficult to produce because it is only in the state of trace amounts in aluminum and zinc ores. Additionally, the metals composing the $CZTS$ are between 25 and 400 times cheaper than indium and gallium. Beyond the price which represents only a small part of the cost of PV panels, these 2 elements are already widely used in the electronics industry, which could procurement for a very large scale PV industry development. However, the abundance and low prices of copper, zinc, and tin make this material very interesting for the PV conversion in the recent years.

1.2.2.4 $p-n$ homojunction solar cells

When light shines onto a semiconductor it can be either reflected, transmitted or absorbed. If it is not reflected from the surface, it will enter the semiconductor. In general, photons with energy higher than the semiconductor band gap will be absorbed, whereas the rest will be transmitted.

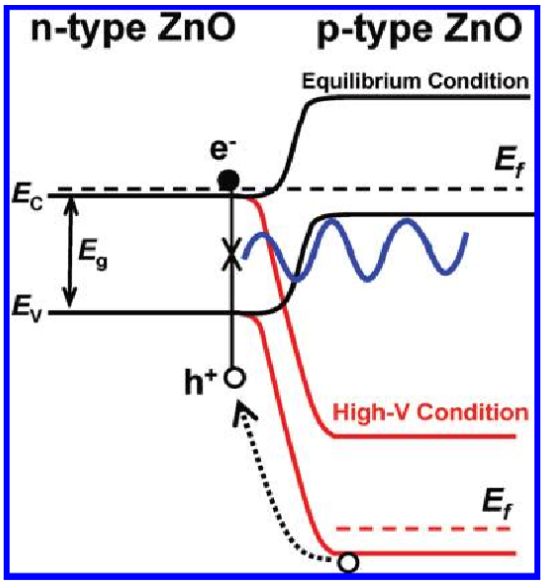

Figure 1.12: Band diagram and dark and illuminated I - V characteristics of a $p-n$ homojunction, ZnO based [51].

When a photon with sufficiently high energy enters a semiconductor, it will be absorbed by exciting an electron from the valence band to the conduction band, thus creating an electron-hole pair. When the electron-hole pair is created it must not be allowed to recombine directly, as this would only create another photon and possibly heat, instead of electrical energy. The built-in electric field of the $p-n$ junction can separate them spatially. A current is created if the separated charge carriers diffuse towards the contacts. When the device is illuminated, the light-generated current causes the $I-V$ curve to be displaced downward (more negative current). The dark characteristics of a $p-n$ Junction solar cell are those of a $p-n$ junction diode. The light generated current is collected within a minority carrier diffusion length of the $p-n$ junction depletion region for ZnO homojunction [51]

1.2.2.5 Homojunctions and heterojunctions

Homojunctions typically need a shallow junction in order to achieve short wavelength response. To reduce the series resistance in the top layer it needs to be heavily doped, as doping increases the number of charge carriers. This in turn will reduce the minority carrier diffusion length by increasing the recombination in this layer. Recombination at the surface occurs due to surface states [33]. The most common commercial solar cells are made of silicon, which is an indirect band gap semiconductor [31]. In order to develop a non-toxic, effective type of $p-n$ solar cells, new materials are being explored. Not all these materials can conveniently be doped both $p-$ and $n-$type, and in order to make a $p-n$ junction with the desired compounds it is sometimes necessary to create a heterojunction. A heterojunction cell consists of two different semiconductors with different band gaps, here generalized as material A and material B. Material A has the wider band gap and acts as a window layer where all photons with energy below the material A band gap are passed through. These photons are in turn absorbed in the depletion region or close to it in material B, the absorption layer [33]. The window layer does not absorb any photons itself. The primary function of this layer is to allow as much light as possible to pass through to the junction and material B [52]. The junction and the absorption layer perform the absorption. A good absorption material should have a high absorption coefficient, because only the excitons created in or near the junction can be harvested. The band gap should be small and direct, and the two materials should have a minimum of interface defects [52]. Because material A and B are different there is a difference in structure, lattice spacing and band gaps. The difference in band gaps creates discontinuity spikes in the conduction and valence bands (see Fig. (1.13)) [53]. These spikes can both create extra barriers for the electrons to overcome or tunnel through, and may also work as potential wells with discrete energy states [31]. The lattice mismatch causes dangling bonds at the interface (see Fig. (1.14)). These dangling bonds become intermediate energy states, acting as recombination centers at the interface. They may also provide sites for quantum mechanical tunneling across the junction [31]. It is important to use semiconductors with very similar lattice structures, in order for the heterojunctions to have as near ideal properties as possible.

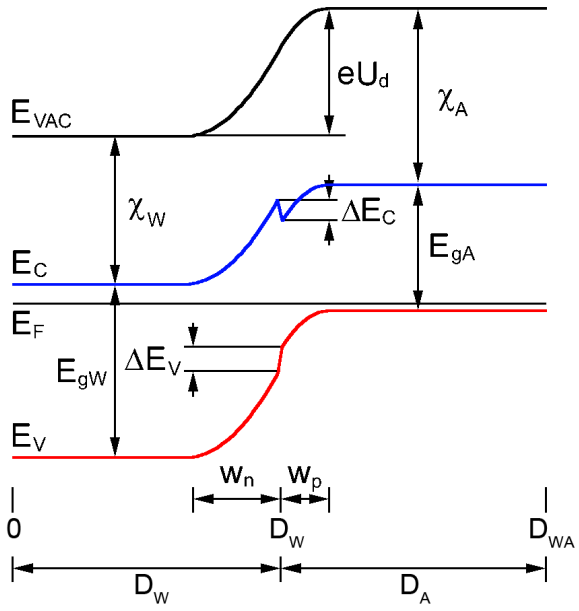

Figure 1.13: A heterojunction between a wide band gap $n-$type window layer and a narrow band gap $p-$type absorber with a discontinuity spike in the conduction band[54].

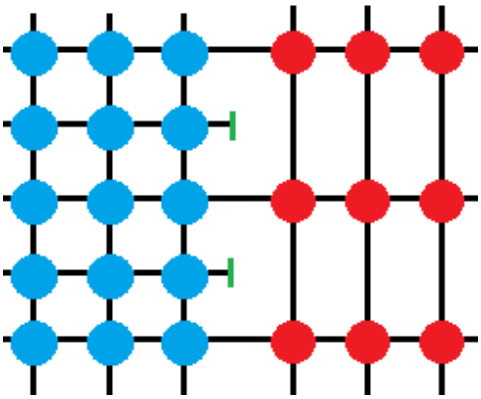

Figure 1.14: The mismatch between the lattices causes dangling bonds at the interface[53].

1.3 Metallic oxides

1.3.1 Zinc oxide

Zinc oxide (ZnO) has fascinating physical properties by which is considered a promising material for transparent optoelectronic devices[55–57]. It is used in various systems such as solar cells [58, 59] and light-emitting diodes [60]. Among its remarkable properties: quantum electron transport, tunable bandwidth, mechanical flexibility, high thermal and

chemical stability, and extremely high optical transparency [61, 62], thanks to its direct and wide band gap, stability under the wet-chemical etching and the high energy radiation [63, 64]. ZnO is an $n-$type semiconductor with high electron mobility, a large gap of $3.3eV$ [13], and a relatively high exciting binding energy of $59meV$. Furthermore, the ZnO emission range is in the near ultraviolet at ambient temperature. Since ZnO electrochemical deposition method was taking place from earlier, by Izaki et al.[13], and Lincot et al., [65] detailed studies have been devoted to the formation of morphologically controlled ZnO films. It crystallizes in three structures: wurtzite, zinc blende, and the rarely observed rocksalt. The wurtzite structure is most stable and thus most common at ambient conditions, compared with other possible crystal structures. The zinc blende form can be stabilized by growing ZnO on cubic structured substrates. In both cases, the zinc and oxide centers are tetrahedral. The rocksalt phase is only observed at relatively high pressures 10 GPa [66]. The wurtzite structure has a hexagonal unit cell with two lattice parameters; a = 3.25 $\mathring{A}$ and c = 5.20 $\mathring{A}$, in the ratio c/a = 1.633 $\mathring{A}$ and belongs to the P63mc space group. It can be simply described as a number of alternating planes composed of tetrahedrally coordinated O^{2-} and Zn^{2+} ions, stacked alternately along the $c-$axis direction as depicted in Fig. (1.15) [67].

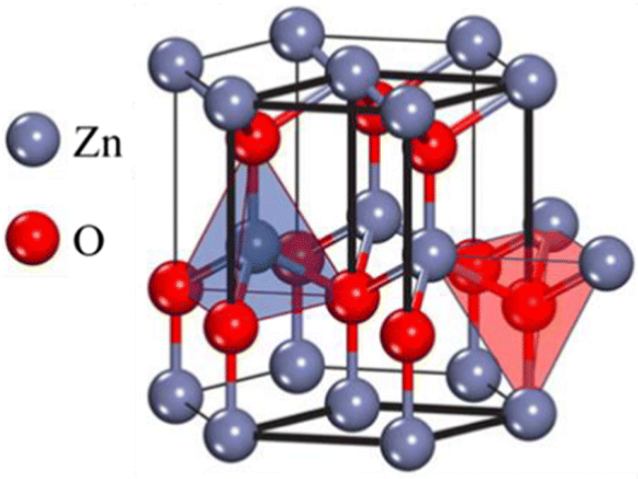

Figure 1.15: ZnO wurtzite structure model with various crystal planes with tetrahedral coordination [67].

1.3.2 Cuprous oxide

The cuprous oxide (Cu_2O) remains an interesting alternative to various metal oxide semiconductors thanks to the high theoretical efficiency of Cu_2O based solar cell. Thus, Cu_2O has been studied as a photocathode for the fractionation of water[68] and as absorber layer in heterojunctions for photovoltaic device[69, 70]. P-type Cu_2O gave correlated results for the majority of these applications[71]. thanks to its large range of conductivity (10^{-13} to $10^{-3}\Omega^{-1}cm^{-1}$) [16, 17] and the high absorption coefficient in the visible range[72–74]. Cu_2O semiconductor has been chosen, as it is nontoxic and low-cost[14, 15]. It is generally exhibits p-type conductivity [16–18, 75], with direct band gap (Eg = 1.9–2.2eV) [72, 73, 76–78]. The Cu_2O has cubic structure (Fig. (1.16)) with a lattice constant of $4.2696\mathring{A}$ [79]. It is easily reduced by hydrogen when heated it undergoes disproportionately in acid solutions producing copper(II) ions and copper. The copper atoms arrange in a FCC sublattice, the oxygen atoms in a BCC sublattice. One sublattice is shifted by a quarter of the body diagonal.

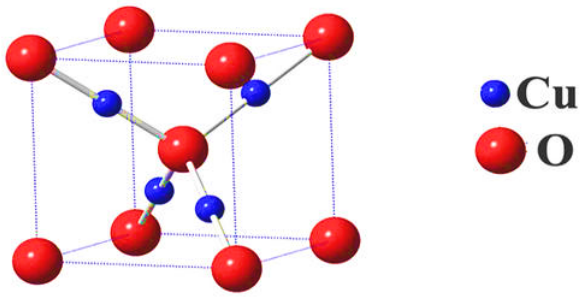

Figure 1.16: Cu_2O cubic structure model with various crystal planes.

1.3.3 $p - Cu_2O/n - ZnO$ heterojunction

An example of a heterojunction solar cell is a Cu_2O/ZnO cell, where the Cu_2O is spontaneously $p-$type and ZnO is $n-$type. The junction is supposed to work reasonably well because the conduction band edges of Cu_2O and ZnO align well, making the discontinuity spike seen in Fig. (1.13) small. Cu_2O is a good absorption layer material, and ZnO

nanowires allow for good charge transport as well as high band gap and large interface, the latter allowing for thicker films and thus higher absorption [80]. Crystallographic orientation is important for achieving a good photoresponse from a $p-Cu_2O/n-ZnO$ cell [72]. A ZnO/Cu_2O heterojunction cell deposited by electrodeposition has open circuit voltage $0.19V$, short circuit current $2mA.cm^{-2}$, fill factor 0.295, and conversion efficiency 0.117% [81]. The conversion efficiency for a cell with Cu_2O deposited at optimum conditions (50%C with high pH) was 0.41% [82]. By rf-magnetron sputtering the above values were $0.26V$, $2.8mA.cm^{-2}$, 0.55, and 0.4% respectively [72]. The efficiency is still very low. The introduction of an interface layer might improve the efficiency, but [80] report no success from using an interface layer of TiO_2. With ZnO being a good window layer, due to its high band gap and ease to form nanowires, combined with the Cu_2O being a good absorber and the good lattice match, the poor performance of these cells is disappointing. An example of a heterojunction solar cell is a Cu_2O/ZnO cell, where the Cu_2O is spontaneously p-type and ZnO is $n-$type. The junction is supposed to work reasonably well because the conduction band edges of Cu_2O and ZnO align well, making the discontinuity spike seen in Fig. (1.13) small. Cu_2O is a good absorption layer material, and ZnO nanowires allow for good charge transport as well as high band gap and large interface, the latter allowing for thicker films and thus higher absorption [80]. Crystallographic orientation is important for achieving a good photoresponse from a $p-Cu_2O/n-ZnO$ cell [72]. A ZnO/Cu_2O heterojunction cell deposited by electrodeposition has open circuit voltage 0.19V, short circuit current $2mA.cm^{-2}$, fill factor 0.295, and conversion efficiency 0.117% [81]. The conversion efficiency for a cell with Cu_2O deposited at optimum conditions (50%C with high pH) was 0.41% [82]. By rf-magnetron sputtering the above values were 0.26V, $2.8mA.cm^{-2}$, 0.55, and 0.4% respectively [72]. The efficiency is still very low. The introduction of an interface layer might improve the efficiency, but [80] report no success from using an interface layer of TiO_2. With ZnO being a good window layer, due to its high band gap and ease to form nanowires, combined with the Cu_2O being a good absorber and the good lattice match, the poor performance of these cells is disappointing.

Chapter 2

Materials and methods

In the first part of this chapter, we will present the principle and the conditions of the electrochemical deposition method used in the PhD project. The experimental condition used for the deposited of ZnO and Cu_2O nanostructures with different morphologies and features we will be illustrate as well. In the second part, we will cite the characterization techniques used for studding the different properties of the synthesized ZnO and Cu_2O thin films.

2.1 Principle and conditions of electrochemical deposition method

2.1.1 Electrodeposition

The electrochemical deposition of crystalline metallic oxides from aqueous precursor solutions has several advantages over the other deposition techniques[13, 65, 83], such as chemical vapor deposition [84], or radiofrequency magnetron sputtering [85, 86]. This efficient procedure just needs low temperatures < 100 °C to prevent the damages of the sensitive substrates and the active materials. This technique is based on a solution close to chemical equilibrium without requiring subsequent annealing, and regardless of the substrate shape and size. The Experimental setup using three electrodes cell is shown in Fig. (2.1)

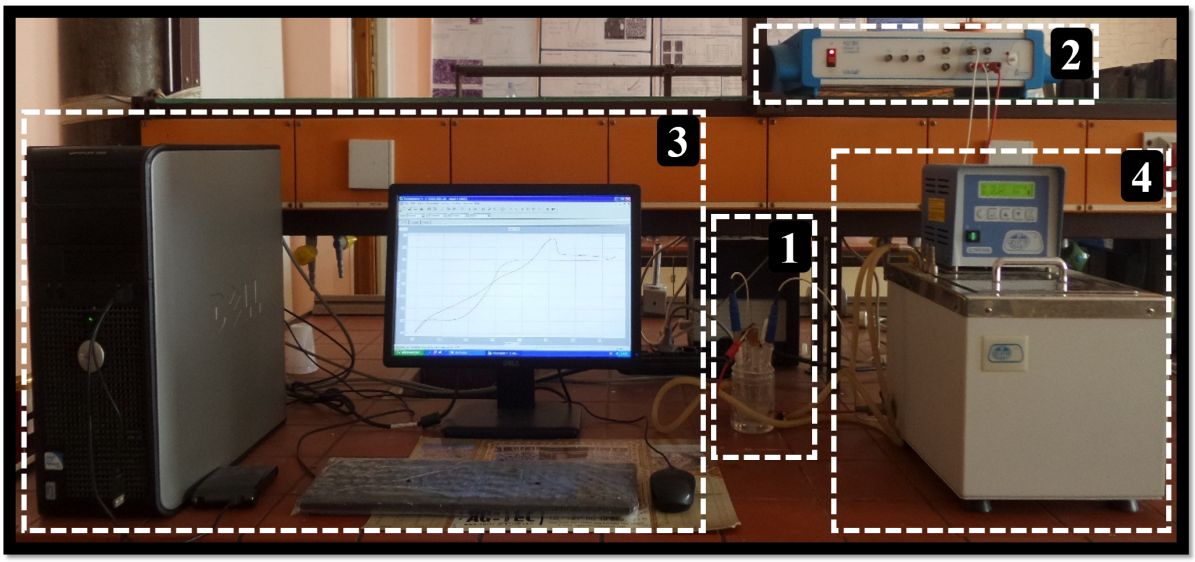

Figure 2.1: Electrodeposition experimental setup; (1) Three electrodes cell, (2) Potentiostat/galvanostatt (Autolab), (3) Computer, (4) Thermostatic bath

The electrochemical cell is composed generaly of three electrodes (see Fig. (2.2)):

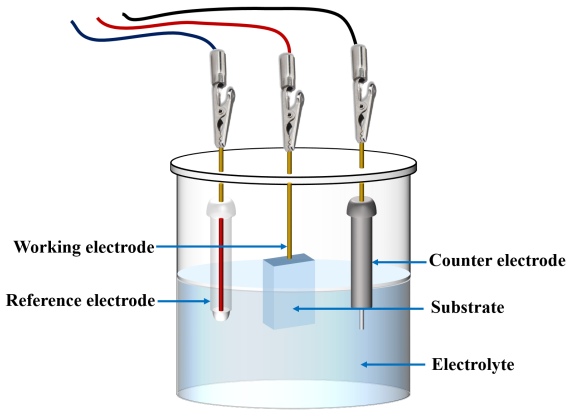

Figure 2.2: Three electrodes cell

• Reference electrode: depending on the material to be deposited, different reference electrodes can be used.In our work, saturated calomel electrode was used (SCE, $+0.241V$ vs. SHE) for deposition of zinc oxide (ZnO) and cuprous oxide (Cu_2O).

• Counter electrode: platinum or silver metal can be used as auxiliary electrode (counter electrode) depending on the electrolyte used and the substrate nature. In our work,

platinum foil was used during the deposition of ZnO and Cu_2O nanostructures.

• Working electrode: It is well known that the electrochemical deposition technique needs a conductive substrate. In our work, oxydes transparent conducteurs is nessacery, where polycrystalline fluorine-doped tin oxide (FTO)-coated glass substrate was used with an exposed area of $1 \times 1\ cm^2$ and sheet resistance $10 - 20\ \Omega.cm^{-2}$.

2.1.2 Electrochemical approaches of elaboration

The electrodeposition method can be carried out either using the potentiostatic approach, or using the galvanostatic approach.

2.1.2.1 Potentiostatic approach

The potentiostatic approach carried out by applying a constant potential, where the current density varying with time during the film growth. Theoretically, it is considered that the potential decides the deposition reaction, [87], for that the scientific community still prefers the electrochemical deposition through potentiostatic mode, and most of the reports on the electrochemically induced growth using potentiostatic control [88–90]. The potentiostatic mode is performed in three electrode cell as shown in Fig. (2.3)

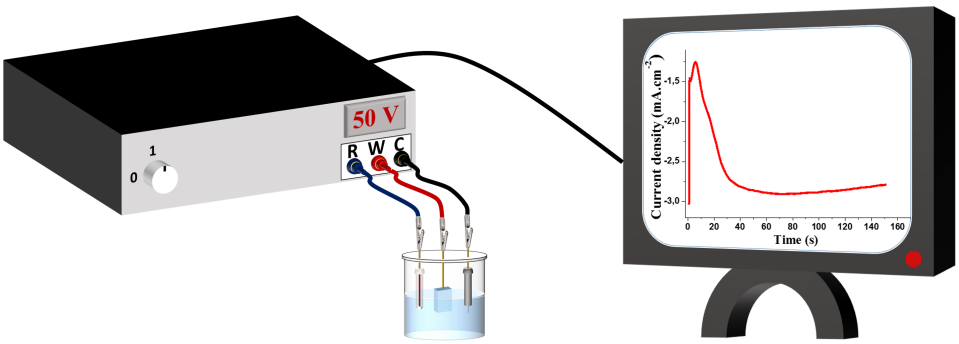

Figure 2.3: Experimental setup under potentiostatic mode

2.1.2.2 Galvanostatic approach

The galvanostatic approach carried out by applying a constant current density, where the potential varying with time during the film growth. This makes the electrodeposition more simple and effective, thanks to the elimination of the reference electrode. sometimes, it is so difficult to link directly the potential to the reaction for such insulating nanostructures[91]. On the other hand, using galvanostatic deposition can provide a constant growth rate of the crystals, where the morphology and the optical properties can be easily adjusted[24, 92]. Although, during the galvanostatic control, the measured potential at the working electrode requires attention, as different redox reactions can take place [93]. To date, such analysis has not yet been provided in detail for the galvanostatic deposition process. Which is performed in two electrode cell as shown in Fig. (2.4)

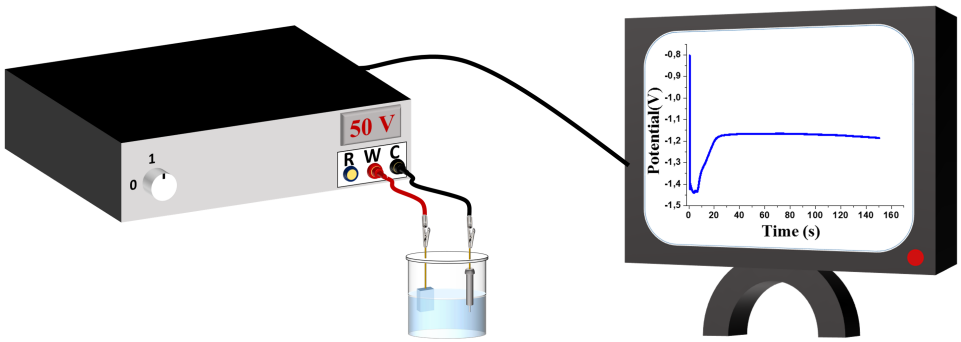

Figure 2.4: Experimental setup under galvanostatic mode

2.1.3 Conditions of elaboration

2.1.3.1 Substrate preparation

Polycrystalline fluorine-doped tin oxide (FTO)-coated glass substrates are used in work for the deposition of different metallic oxides. The FTO-coated glass slide was cut into pieces $1 \times 2\ cm^2$. The condition of the surface and the cleanliness of the substrate are essential parameters. Indeed, the presence of impurities on the substrate can considerably influence the nucleation and growth of germs during the electrodeposition of films, which

leads to the modification of the properties of the deposits thus obtained [94]. An ultrasonic cleaning procedure has been established during the preparation of the substrates in order to eliminate these impurities and initiate the nucleation of germs. Prior to each deposition the substrate was cleaned ultrasonically at 50 °C in ethanol, acetone, and then rinsed in distilled water for $15min$ in each step.

2.1.3.2 Electrolyte preparation for the deposition of ZnO nanostructures

The objective behind this part is to elaborate ZnO nanowires with high stability and well orientation. Abbasi et al.[95] have studied the precursor nature effect on the ZnO growth. They have observed that it affects the morphology and the size of the different nanostructures, where zinc nitrate ($Zn(NO_3)_2$) anions yield the nanorods and zinc sulfate anions yield the nano-flakes. On the other hand, ZnO nanosheets can be elaborated successfully from different mediums. However, Barreto et al. [96] have recommended using $Zn(NO_3)_2$ as a precursor to obtain a very pure phase of ZnO of high density.
In the present work, ZnO nanowires (1D growth) and ZnO nanosheets (2D growth) were successfully elaborated by obeying some conditions. It is reported before by Pradhan,D [97] that the concentration of the precursor ($[Zn^{2+}]$) in the electrolyte is important to control the dimensionality and the morphology of nanostructures. The precursor concentration should be less than $0.01M$ for the formation of nanospikes and one-dimensional (1D) nanowires. Whereas, it should be more than $0.05M$ for the two-dimensional (2D) nanosheets and nanodisks. We have d two different baths: chloride medium and nitrate medium with different precursor ($Zn(NO_3)_2$) concentrations. In the nitrate medium, we use $0.08M$ ($> 0.05M$) of $Zn(NO_3)_2$ to elaborate 2D ZnO nanosheets, while in the chloride bath, we use $0.001M$ ($< 0.01M$)of $Zn(NO_3)_2$ to grow 1D ZnO nanowires. In the other hand, the supporting electrlyte has an important effect on the final morphology, the structural and optoelectronical properties. That's why, using the KCl as a supporting electrolyte to grow ZnO nanowires is to ensure a good conductivity of the aqueous solution. Besides, Tena-Zaera et al.[98] have reported that the chloride concentration plays an important role on the ZnO morphology, where high chloride concentrations (higher than $1M$) induce a decrease in the rate of O_2 reduction, leading to favor lateral growth of

ZnO on 2D dimension and formation of ZnO nanowires with a large diameter of 300nm. However, the impediment of the lateral growth, to improve the growth in 1D dimension, can be achieved by decreasing the KCl concentration to $0.1M$, which increases the rate of the O_2 reduction. furthermore, to obtain high aspect ratio ZnO nanowires, very low precursor concentration is necessary[97] ($[Zn^{2+}] \ll [Cl^{-}]$ [99]). The different chemical species which have been used are summarized in Tab. (2.1)

Table 2.1: Different chemical species used within the electrolytes to grow ZnO nonosheets and ZnO nanowires.

Chemical specie	Chemical formula	Molar mass (g/mol)
Zinc nitrate tetrahydrate	$Zn(NO_3)_2.4H_2O$	261.45
Potassium nitrate	KNO_3	101.1
Potassium chloride	KCl	74.5513

2.1.3.3 Electrolyte preparation for the deposition of Cu_2O nanostructures

Different Cu_2O nanostructures morphologies were successfully elaborated in this thesis. Thus different solution and media were prepared. Firstly, Cu_2O nanostructures in Chapter 4 were grown in bath containing a $0.05M$ copper sulfate ($CuSO_4$), $0.06M$ citric acid, and a $NaOH$ adjusting the pH at 11 and 12. However for Cu_2O nanostructures in Chapter 5, KCl has been added to the electrolyte with two different concentrations ($0.001M$ and $0.1M$) to study its effect on the final properties. Secondly, Cu_2O nanoparticles in Chapter 5 were prepared from a $0.003M$ of copper nitrate ($Cu(NO_3)_2$) with a $0.1M$ of potassium chloride (KCl). To study the additive effect on the features of the Cu_2O nanoparticles, a $0.0015M$ of ammonium chloride (NH_4Cl) was added to the electrolyte. The different chemical species which have been used are summarized in Tab. (2.2)

Table 2.2: Different chemical species used within the electrolytes to grow Cu_2O nanostructures and Cu_2O nanoparticles.

Chemical specie	Chemical formula	Molar mass (g/mol)
Copper sulfate pentahydrate	$CuSO_4.5H_2O$	249,6
Citric acid Anhydrous	$C_6H_8O_7$	192,12
Potassium chloride	KCl	74.5513
Sodium hydroxyde	NaOH	39,997
copper nitrate	$Cu(NO_3)_2$	187.56
Ammonium chloride	NH_4Cl	53.491

2.2 Electrochemical methods

2.2.1 Cyclic voltammetry

Cyclic voltammetry was used to determine promising voltages for deposition.

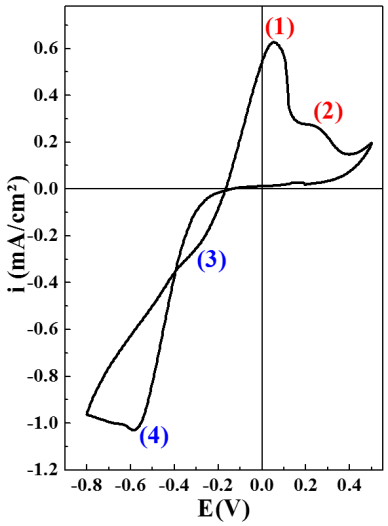

Figure 2.5: Cyclic voltammograms recorded in $0.05M$ of $CuSO_4$ at 70 °C, in pH of 11. Potential scan rate is $100mV/s$. (1) and (2) are the oxidation peaks. (3) and (4) are the reduction peaks. (3) corresponds to the formation of Cu_2O

The plots may also show voltages where stripping of an existing film takes place, as large current peaks with abrupt endings indicate there being no more material to strip. Different peaks sometimes correspond to depositions of different compounds, such as Cu_2O or metallic Cu or ZnO. A peak shows the highest deposition rate for each material. A good deposition voltage should be in the voltage range of the desired deposition, without any other compound being deposited, and with a measurable current. Fig. (2.5) shows the cyclic voltammetry plots in order to check the peak corresponding to Cu_2O deposition potential.

2.2.2 Chronoamperometry

Chronoamperometry is the electrochemical technique used under ptentiostatic approach, which consists to apply a constant potential chosen from cyclic voltammetry between the working electrode and the reference electrode, and plotting the variation in the current density flowing between the working electrode and the counter electrode as a function of time. The chronoamperometric curve as well as the different electrodeposition steps are shown in Fig. (2.6)

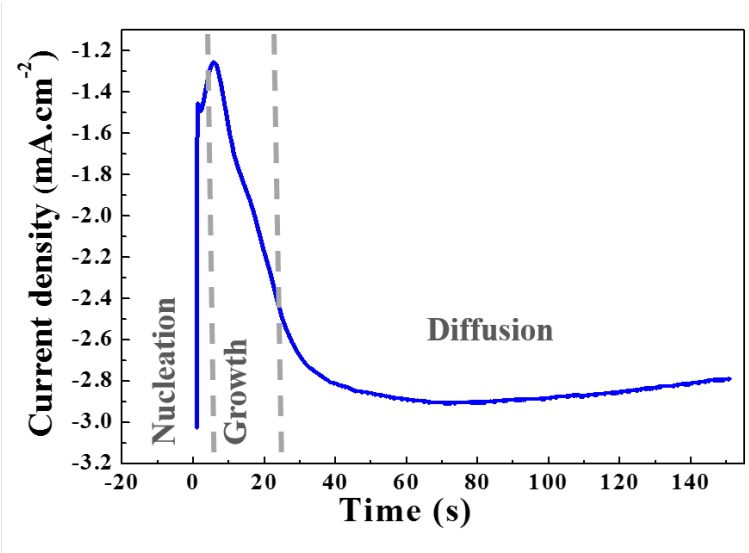

Figure 2.6: Chronoamperometric curve obtained during the electrodeposition under potentiostatic mode with the different formation steps

- 1^{st} Stage (nucleation): Corresponds to the formation of the first germs on the surface of the working electrode (FTO in our case).
- 2^{nd} Stage (Growth): Corresponds to the growth of germs.
- 3^{rd} Stage (Diffusion): Corresponds to the diffusion of ions, which becomes the limiting step for the growth of the deposited film.

2.2.3 Chronopotentiometry

Chronoamperometry is the electrochemical technique used under galvanostatic approach, which consists to apply a constant current density at the working electrode, and plotting the variation in the over potential flowing between the working electrode and the counter electrode as a function of time. The chronopotentiometric curve as well as the different electrodeposition steps are shown in Fig. (2.7)

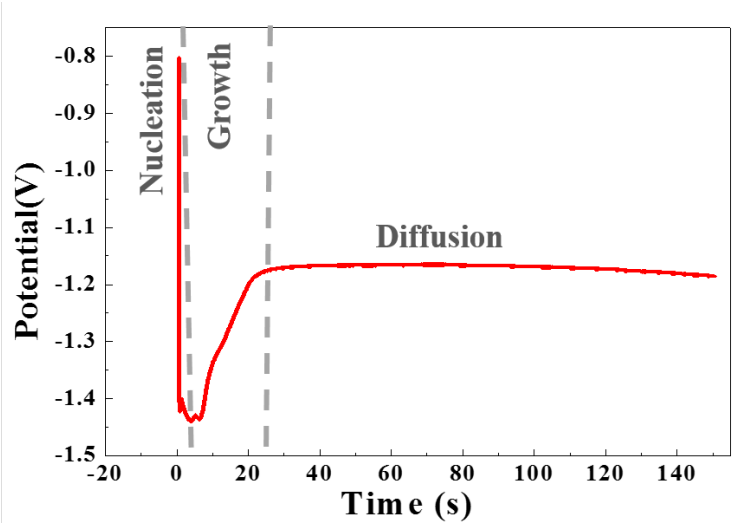

Figure 2.7: Chronopotentiometric curve obtained during the electrodeposition under galvanostatic mode with the different formation steps

2.2.4 Mott-Schottky measurements

The Mott-Schottky ($M-S$) measurement is used to investigate the electronic properties of semiconductor materials based on examining the semiconductor/electrolyte contacts and measuring the apparent capacitance as a function of the applied biases under depletion

conditions [100]. A defect is classified as a donor if it donates electrons to the conduction band and as an acceptor if it accepts an electron from the valence band and leaves behind a positively charged hole. $C^{-2} = f(E)$ [101] plots are presented in Fig. (2.8)(a) for $n-$type semiconductor (ZnO) and Fig. (2.8)(b) for $p-$type semiconductor (Cu_2O). Where the positive slope of the linear part confirms that the sample is $n-$type semiconductor (Fig. (2.8)(a)). However, the negative slope of the linear part confirms that the sample is $p-$type semiconductor (Fig. (2.8)(b)).

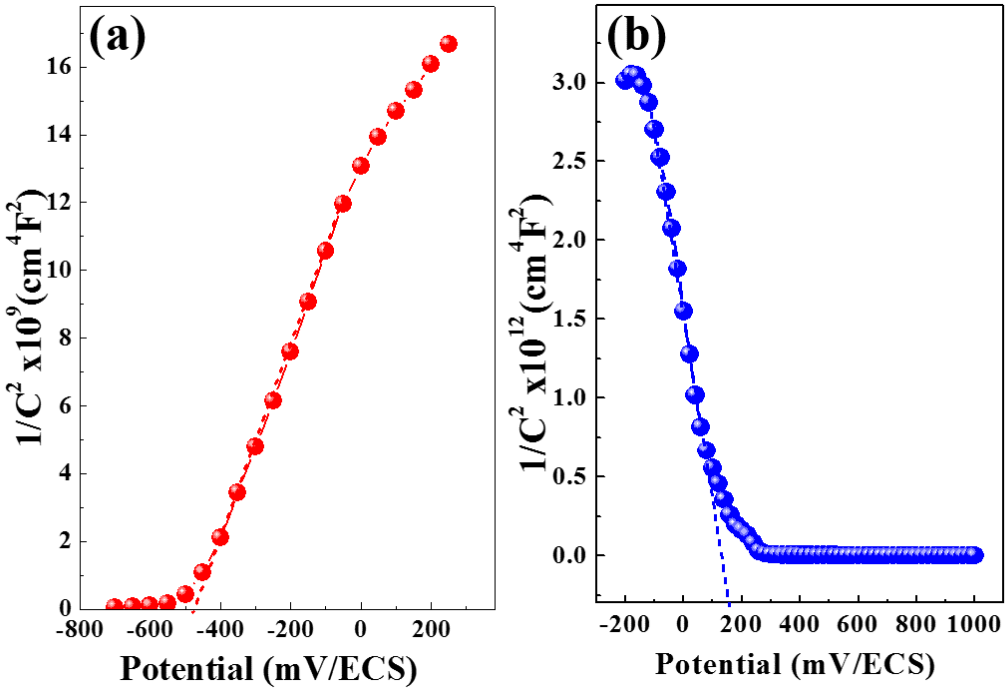

Figure 2.8: Mott–Schottky plots. a) for ZnO thin films ($n-$type semiconductor) , b) for Cu_2O thin films ($p-$type semiconductor).

The conduction type, the flat band (E_{fb}), and the acceptor densities of the deposited nanostructures can be determined by studying the semiconductor electrolyte interface using the Mott–Schottky ($M-S$) measurements. In which, the depletion layer capacitance $C^{-2} = f(E)$, at a fixed frequency, can be measured and presented as an $M-S$ plot following the equation Eq. (2.1)[102] and Eq. (2.2)[103] below. The Eq. (2.1) shows the relationship between the space charge capacitance and the defect density for $n-$type

semiconductor (ZnO)

$$\frac{1}{C^2} = \frac{2}{\varepsilon\varepsilon_0 \, N_D \, e} \left[(E - E_{fb}) - \frac{kT}{e} \right] \tag{2.1}$$

Where C is the space charge capacitance in the interface of ZnO semiconductor, e is the electron charge, N_D is the donor concentration of ZnO $n-$type semiconductor, ε_0 is the vacuum permittivity, ε is the ZnO dielectric constant, k is the Boltzmann constant, T is the absolute temperature, and E is the applied potential. From the slope of $M-S$ plots which the line interpolates until $C^{-2} = 0$ gives the flat-band potential (E_{fb}). While the N_D of the different samples have been calculated thanks to this slope.

Eq. (2.2)showed the relationship between the space charge capacitance and the defect density for $p-$type semiconductor (Cu_2O) ,

$$\frac{1}{C^2} = \frac{2}{\varepsilon \, \varepsilon_0 \, N_A \, e} \left[(E - E_{fb}) - \frac{kT}{e} \right] \tag{2.2}$$

Where C is the space charge capacitance in the interface of Cu_2O semiconductor, e is the electron charge, N_A and is the acceptor concentration of a $p-$type semiconductor, ϵ_o is the vacuum permittivity, ϵ is the dielectric constant Cu_2O, k is Boltzmann constant, T is the absolute temperature, E is the applied potential.

2.2.5 Photocurrent analysis

Photocurrent (PC) analysis is another valuable measurement technique, typically employed in the physics of semiconductor materials and provides information about charges collection/separation and chemical reactions happening across the semiconductor/electrolyte contacts under dark and illuminated conditions. It rests on determining the quantity of charge on the basis of the time dependence of current flowing through the semiconductors. As a semiconductor photoelectrode is in contact with an electrolyte solution, a depletion layer is formed at the surface of the photoelectrode [104]. Since there are few free carriers available, the current (dark current) is very small. When light is shed on the surface of the semiconductor photoelectrode, electron-hole (e^-/h^+) pairs are generated and separated in the depletion region, and consequently, a photocurrent response is produced. The photocurrent generated increases if the density of free carriers

increased when illuminated by the light. The photocurrent reading will decay to the original value (dark current) when the light is blocked (see Fig. (2.9)). The magnitude of the photoresponse depends mostly on the semiconductor properties, applied potential, and electrolyte solution composition [104, 105]. For an $n-$type semiconductor electrode at an open circuit, the Fermi level energy of the semiconductor is typically higher than the redox potential of the electrolyte and the electrons as major carriers move towards the semiconductor/electrolyte interface to attain equilibrium (Fig. (2.9)). Therefore, a depletion layer is formed at the semiconductor surface, resulting in the upward bending of the band edges at the interface. Under light of energy greater than the band-gap, photons are absorbed and e^-/h^+ pairs are created. The holes move into the electrolyte and the electrons move into the semiconductor.

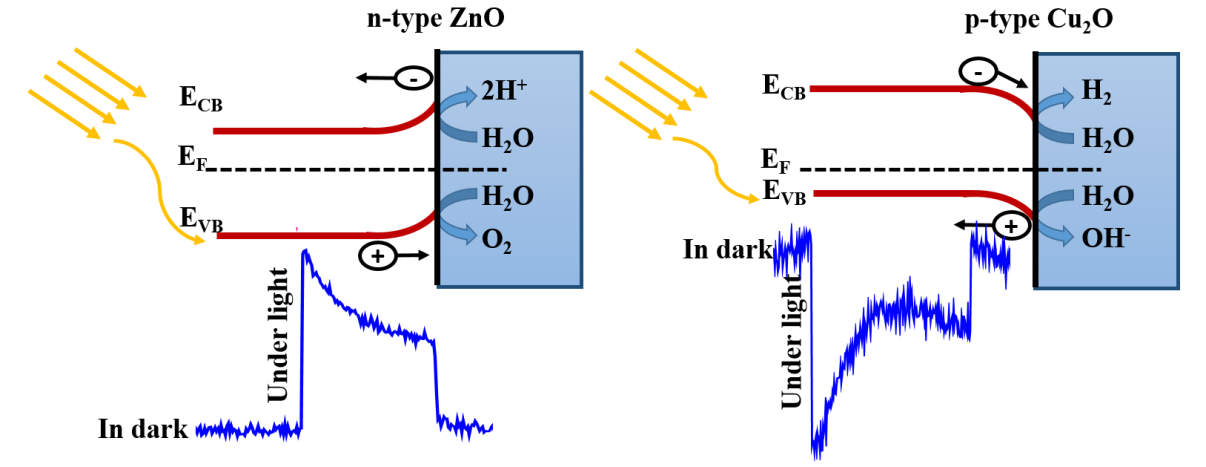

Figure 2.9: Photocurrent interaction principle in semiconductor/electrolyte interface

Therefore, the irradiation of $n-$type semiconductors will promote the anodic currents, i.e., positive currents than that in the dark conditions [106]. The behavior of $p-$type semiconductors is different from that of $n-$type semiconductors. In $p-$type semiconductors, the depletion layer is negatively charged as the holes are major carriers and move from the electrode to the electrolyte, causing a downward bending in the band edges. Under irradiation, the holes move into the electrode and the electrons move into the electrolyte, giving rise to generate cathodic currents, i.e., negative currents than that in the dark

conditions, as illustrated in Fig. (2.9).

2.3 Physical characterization instruments

2.3.1 Autolab: Potentiostat/Galvanostat

A potentiostat is an instrument that supplies a chosen voltage or current to a 3-electrode cell, and monitors the output current or voltage. In cyclic voltammetry, the supplied voltage oscillates between two different voltages at a constant scan rate. The current vs. voltage function is then plotted, showing rates of chemical deposition and stripping for the supplied voltages. Typical scan rates are $10 - 100\ mV/s$. The potentiostat may also supply a constant voltage, constant current, and voltage or current step functions. For supplied voltage the current is plotted, and for supplied current the voltage is plotted. It is important that both of the other electrodes have electric contact with the working electrode. If there is no contact with the counter electrode, no current can be passed through, and if there is no contact with the reference electrode, the amplification circuit inside the potentiostat acts as an oscillator, causing wildly oscillating voltage supply. A diagram of a typical potentiostat circuit is given in Fig. (2.10)

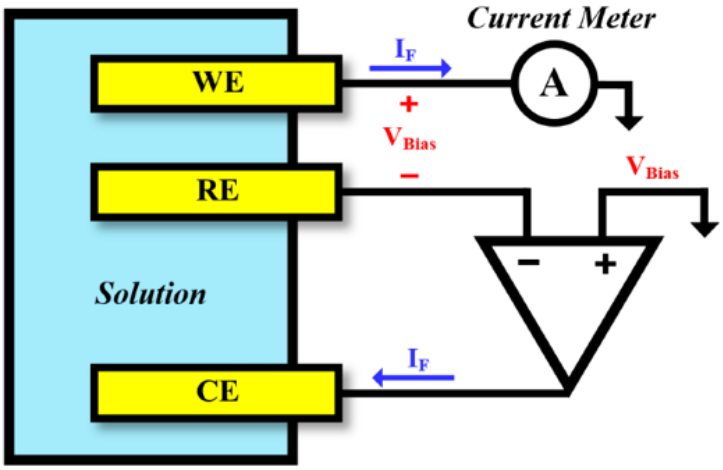

Figure 2.10: Circuit diagram of a typical three-electrode potentiostat circuit[107].

2.3.2 Scanning electron microscope (SEM)

A scanning electron microscope (SEM) is an instrument that directs an electron beam at the sample and collects the emitted secondary electrons to form an image. The secondary electrons are electrons that are re-emitted from the specimen, they form an image shows the morphology of the sample surface in great detail(high resolution). Back scattered (reflected) electrons can also be collected. The back scattered electron image shows the morphology and also composition. Back scattered electron intensity is dependent on the atomic number of the sample. The microscope consists of an electron gun, a condenser lens, scan coils, objective lens, the sample and an electron collector. The electron gun works by heating a filament slowly (to avoid fracturing) and accelerating the electrons using a voltage of $5-25kV$. Electrons are collected and the intensity data is coupled with the scanning coils to create an image of the surface. The instrument works in a vacuum to increase the mean free path of the electrons in order for as many as possible to reach the appropriate detector [108]. A typical SEM is shown in Fig. (2.11). In this thesis a SEM-FEG (JEOL LSM-6701F) technique from secondary electrons (SE) images at $20kV$ was used.

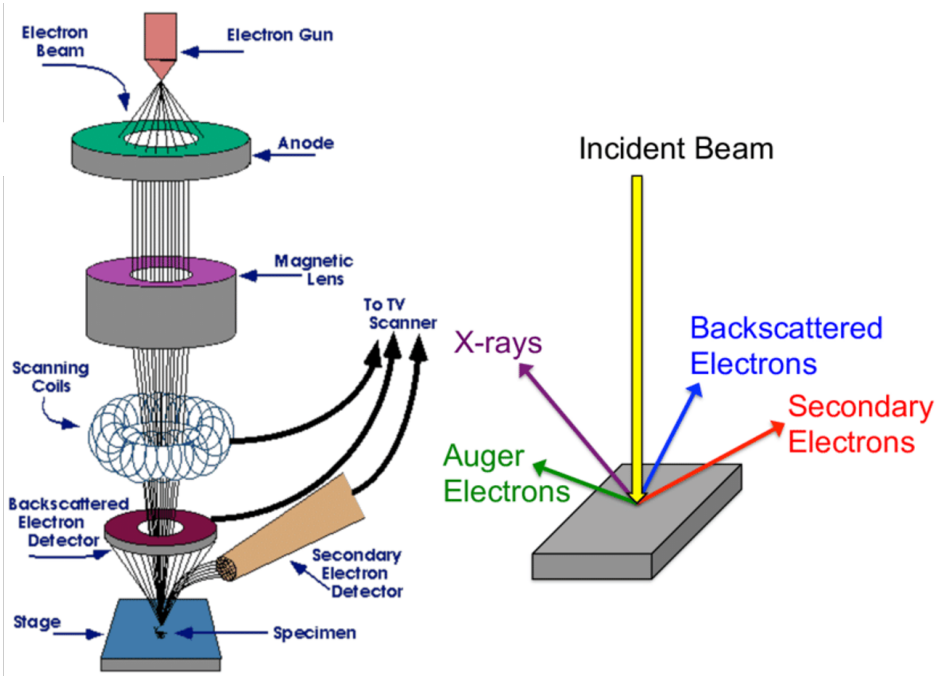

Figure 2.11: Illustration of a schematic principle of the Scanning Electron Microscope.

2.3.3 Atomic Force Microscope (AFM)

Characterization by AFM constituted a non-destructive method of analyzing the topography of a given sample. So, we can have additional information on the film topography of the surface by 2D or 3D views and also the roughness of the analyzed surface. The mode of operation of the surface of the sample by a lever-tip can be moved along the$X$, Y and Z directions. Under the action of Van der Waals forces, electrostatic, magnetic, chemical, etc., the lever can be deflected. In order to measure the deflection of the lever, a laser diode is used. The laser beam emerging from the diode is focused on the end of the lever and then it is reflected towards the photodetector. As a result, deflection of the lever causes the reflected beam movement [109]. The operation of an AFM can be done either, through contact mode, or non-contact mode. Fig. (Fig. (2.12) shows a schematic principle for the AFM. The images of the surface are thus obtained by horizontal and vertical displacements of the tip relative to the sample. In non-contact mode, AFM images are obtained by detecting the deflection of the fixed stiffness lever at any point during the surface scan. PicoScan 5.3 from molecular imaging has been used in this thesis.

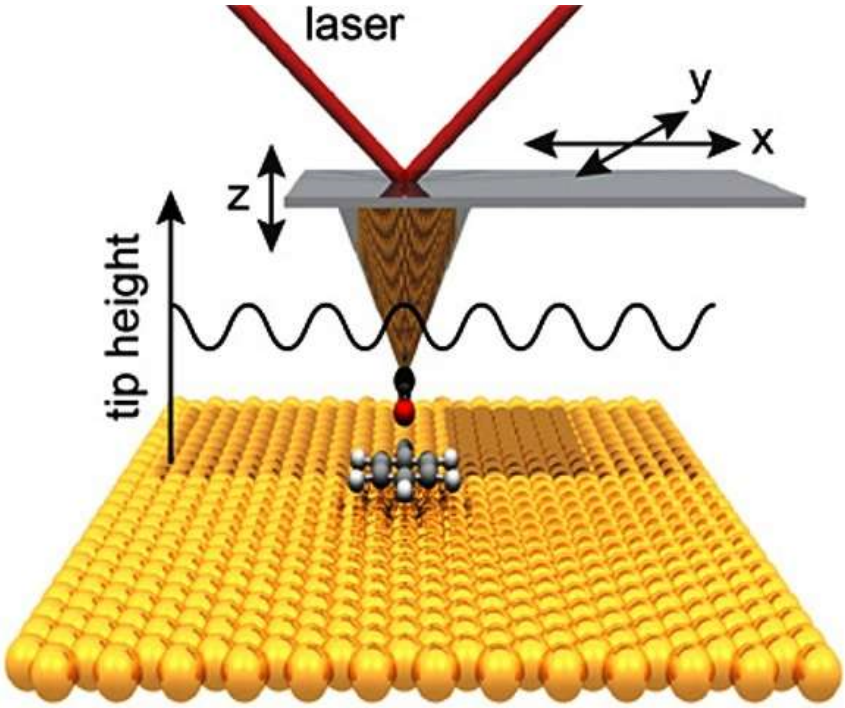

Figure 2.12: Illustration of the AFM schematic principle

2.3.4 X-ray diffractometer (DRX)

X-ray diffraction is a technique used to determine the lattice parameter of a mono or polycrystalline structure by reflecting x-rays off the surface and analyzing the diffraction pattern. In order to create the diffraction pattern, the emitted x-rays must be of the same energy. This is achieved by bombarding a certain material (Cu and Mo are common materials) resulting in $K\alpha$ radiation. These rays are further monochromatized by passing them through a filter or a single crystal. This monochromatic beam of x-rays then hits the sample, which reflects the radiation. The lattice structure of the sample, if there is one, then causes constructive interference in some directions [34]. This means the diffraction pattern will be mostly noise for amorphous structures, but for crystalline samples there will be a characteristic set of intensity peaks for the crystal orientations for each substance. The diffraction pattern is found by moving the detector around the sample while mapping the x-ray intensities, see (Fig. (2.13)). Typically, the x-ray source angle is called θ, and the detector angle is called 2θ. In this thesis we have used a Siemens D5000 X-ray diffractometer with a $CuK\alpha$ radiation, the 2θ range of (20 °C-75 °C) was recorded at a rate of 0.02° 2θ per $0.5s$

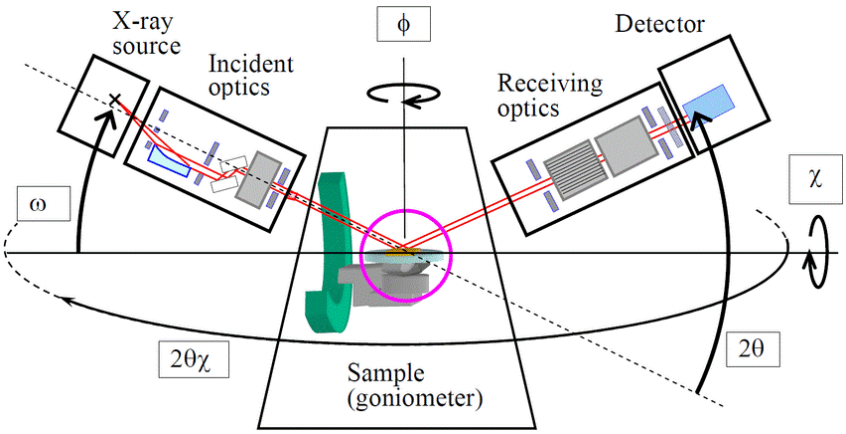

Figure 2.13: Illustration of the principles behind an XRD. The detector moves and registers the reflected intensity at different angles (2θ).

The average crystallite size (D) can be calculated using Scherrer's Formula Eq. (2.3).

$$D = 0.9\frac{\lambda}{\beta cos\theta} \tag{2.3}$$

Where D is the average crystallite size (nm), λ is the X-rays wavelength ($\lambda_{cu} = 1.5406\mathring{A}$), θ is Bragg's angle, and β is the FWHM (Full width at half maximum) in radians.

2.3.5 UV-Vis spectrophotometer

Because the substrates were transparent, the optical properties of the films were found by measuring the transmitting light when the film was exposed to light of a certain energy spectrum. UV-Vis spectrophotometry analysis refers to the study of optical properties of sample materials over a wavelength range corresponding to the visible and the adjacent ultraviolet and near-infrared ranges. This technique is based on the quantification of the light absorbed or transmitted by a sample. In its simplest form, a sample is placed between a light source and a photodetector, and the intensity of a beam of UV-Vis light is measured before and after passing through the sample as depicted in Fig. (2.14). These measurements are compared at each wavelength to quantify the sample's wavelength-dependent absorbance or transmittance spectrum and each spectrum is background corrected using a buffer blank to guarantee that spectral features from the buffer blank are not included in the spectrum of the sample material. In this thesis spectrophotometer 2401 PC type SHIMADZU was used.

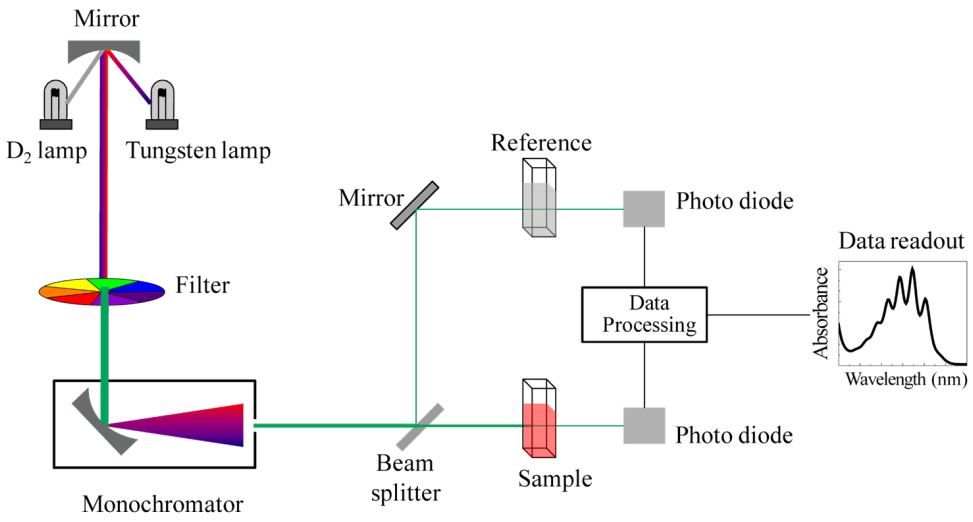

Figure 2.14: Illustration of UV-Vis spectrophotometry schematic principle

The absorption coefficient was calculated from Beer-Lambert's low as follows:

$$\alpha = \frac{-\ln\left(\frac{T}{(1-R)}\right)}{L} \tag{2.4}$$

Where α is the absorption coefficient, L is the optical path (in our case is the film thickness), T is the transmittance, R is the reflectance, and A is the absorbance ($A = \alpha L$). During the measurement, the incident field was perpendicular to the film surface means the reflectance was null. The $(\alpha h\nu)^2$ versus the photon energy ($h\nu$) plotted using Tauc relation Eq. (2.5) [110], in order to determin the optical band gap for the deposits. Theoretically, the optical band gap can be obtained by extrapolating downwards to the photon energy axis for the corresponding straight lines [110].

$$(\alpha h\nu) = A(h\nu - Eg)^n \tag{2.5}$$

Where α and A are the absorption coefficient and the absorption factor (the absorbance), respectively. $h\nu$ is the photon energy as a function of the light frequency, E_g is the band gap energy of the material, and n depends on the nature of the transition. In direct band gap absorption without phonon mediation $n = 1/2$.

2.3.6 Stylus profilometer

The stylus instrument is most commonly used, through half a century of development, is one of the most widely used techniques for surface morphology measurements [111, 112]. The stylus profilometer can be used to measure surface morphology with a diamond stylus probe that touches the surface. Height variations are measured as either the stylus or the sample is being moved. The mechanical movements of the stylus are converted to electrical signals, which are then amplified to give DC output signals. Most modern stylus systems use digital data recording methods. All of the stylus profilometry techniques have many components and a data acquisition system, as shown in Fig. (Fig. (2.15). The pickup comprises the stylus, stylus holder mechanism, transducer, and any signal conditioning associated with the transducer. The pickup is driven by a gear box, which draws the stylus over a surface at a constant speed. As the system is scanned across a sample, the

z-axis displacements of the stylus are sensed by the transducer (usually a linear variable differential transformer), which converts linearly the mechanical motion to the electrical signal. The signal, after being magnified by an electronic amplifier, is collected by a data acquisition system to generate the surface profile.

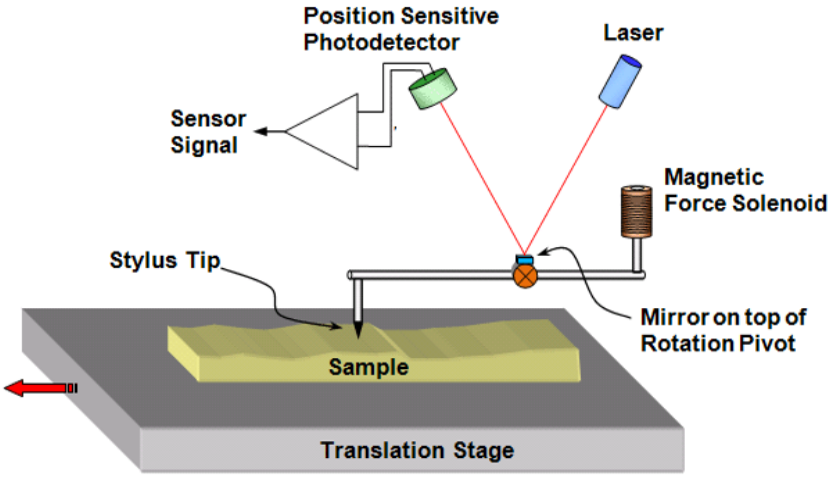

Figure 2.15: The schematic principle of a stylus profilometer.

2.3.7 Current-Voltage characterization in the dark (I-V measurement)

$I-V$ measurements in the dark are very useful for examining the properties of the $p-n$ junction, the diode is a $p-n$ junction connected to two contacts, the variation of the applied voltage across the hetero-junction creates a current varied exponentially with the voltage as shown in Fig. (Fig. (2.16). The current across the hetero-junction varies exponentially with the applied voltage and its variation can be described by the standard Schottky diode equation Eq. (2.6)[113].

$$I\left(V\right)=Is\left(\exp\left(\frac{qV}{KTn}\right)-1\right) \tag{2.6}$$

Where: Is: saturation current, n is the ideality factor and V applied voltage, k is the Boltzmann constant, T is the absolute temperature, q is the elementary electronic charge.

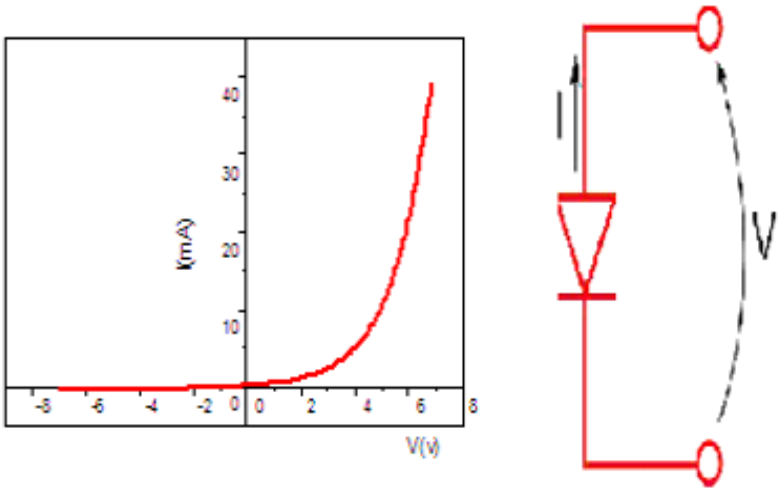

Figure 2.16: I-V characterization of CZTS/ZnS hetero-junction and the equivalent circuit of an ideal diode.

The $(I-V)$ characterization is an important tool to study and analyze the electrical properties of the diode by the determination of the diode parameters such as the ideality factor (n), and saturation current (Is). The ideality factor n is an important parameter of the diode which shows how close the realized diode to the ideal diode of Schottky. It is used to determine the dominate transport mechanism of the current across the hetero-junction. The ideality factor (n) can be calculated from the variation of the slope of the linear portion of $\ln(I)-V$ as shown in Fig. (2.16) and it can be expressed as the following formula Eq. (2.7):

$$n = \frac{\mathrm{q}}{\mathrm{KT}} \left(\frac{\mathrm{dV}}{\mathrm{d}(\ln(\mathrm{I})} \right) \tag{2.7}$$

The saturation current (Is) is activated by the activation energy EA and represent the diode leakage current in the absence of light, as seen in Fig. (2.17). Is is due to the diffusion of minority carriers in quasi neutral region (electron in the n region and holes in p region) and refer also to the generation of free carriers in the space charge region. Saturation current and ideality factor can be determined from the semi logarithmic plot of the current as function of the applied voltage.

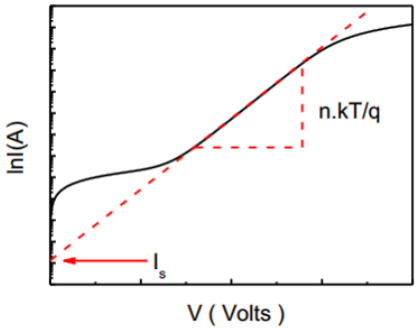

Figure 2.17: Semi logarithmic scale of the current as function of applied voltage of a diode.

Chapter 3

Electrochemical parameters effect on the ZnO nanostructures properties

3.1 Introduction

BY modifying the electrodeposition parameters; such as the concentration of the Zn^{2+} precursor in the electrolyte, the potential applied during processing, the temperature of the bath, and the nature of the additives used. Various ZnO morphologies have been produced, including nanowires[114], nanopiles [115], nanoplastic [116], nanoparticles pradhan2008controlled [97], nanowalls, nanodisks, nanospikes, nanopillars [97] and epitaxial films [117]. Most of them were deposited in aqueous solutions, under ambient atmosphere (60 °C- 90 °C). Among them are nanowires, which drew the attention of scientists because of their capacity to serve as a fundamental 1D architecture for applications in solar cells [118], light-emitting diodes[119], and chemical sensors [120]. The electrochemical deposition of crystalline ZnO from aqueous precursor solutions has several advantages over the other deposition techniques[13, 65, 83]; such as chemical vapor deposition [84], or radiofrequency magnetron sputtering [85, 86]. This efficient procedure just needs low temperatures <100 °C to prevents the damages of the sensitive substrates and the active materials. This technique is based on a solution close to chemical equilibrium without requiring subsequent annealing; and regardless of the substrate shape, it will guide us to a variety of optional feature geometries. Among the different morphologies of ZnO

nanostructure; ZnO nanosheet, which is characterized by its unique structure used in many devices; such as the dye sensitized solar cell [87, 121], the gas sensor [122], the photodetector [123, 124], and the piezoelectric nanogenerator [125]. The control of the morphology of the ZnO nanosheets in terms of density, height, and porous structure, etc, is therefore important to improve the device's performance. To make nanosheets grow on a conductive substrate by an electrochemical method provides a simple means of obtaining an excellent material-substrate bond which ensures good electronic transport required by the electronic devices.

In order to investigate the effect of the elaboration key parameters; the applied current density and the approach, on the electrochemical, structural, optical, and morphological proprieties, this chapter is taking place, in which we elaborate ZnO nanostructures with varied morphology directly on FTO-coated glass substrates at 70 °C, using a simple electrochemical deposition technique. It is reported before by Pradhan,D [97] that the concentration of the precursor $Zn(NO_3)_2$ in the electrolyte is important to control the dimensionality and the morphology of nanostructures, where for the formation of nanospikes and one-dimensional (1D) nanopillons, the precursor is less than $0.01M$ while for the two-dimensional (2D) nanodiffes and nanodisks are more than $0.05M$. In this work, we trace back two different baths: chloride medium and nitrate medium with different concentrations. In the nitrate medium, we use $0.08M$ as a precursor concentration to elaborate the ZnO nanosheets while in the chloride bath, we use $0.001M$ to grow the ZnO nanowires. In the first part, we study the current density effect for the ZnO nanosheets through galvanostatic mode with two electrodes system of unique characteristics; where the current provided in a constant way, leads to a constant crystal growth rate, which gives better control. In the second part, we compare the optimal current density for ZnO nanosheet, obtained in the previous part by the galvanostatic mode, with another obtained by potentiostatic mode, keeping the same experimental conditions. Furthermore, in chloride electrolyte, two samples of ZnO nanowires are prepared using different approaches.

3.2 Galvanostatic electrodeposition of ZnO nanostructures: Current density effect

In order to investigate the current density effect on the properties of ZnO nanosheets, Different current densities were applied, $-0.5, -1, -2$ and $-3\ mA.cm^{-2}$ for 2 min. The deposition process was performed in electrolyte contains 0.08 M Zinc nitrate ($Zn(NO_3)_2$), and 1 M potatium nitrate (KNO_3). When, the deposition temperature held constant at 70 °C.

3.2.1 Electrochemical analyses

3.2.1.1 Deposition mechanism of ZnO nanostructures

Fig. (3.1) shows the potential as function of time. The curves recorded during electrodeposition of ZnO nanosheets at different current densities on FTO substrate at 70 °C for 150 sec. Starting by the development of OH^- resulting from the reduction of nitrate anions (NO_3^-)to nitrite (NO_2^-),the ZnO layer was formed by a multi-step process

$$NO_3^- + H_2O + 2e^- \rightarrow NO_2^- + 2OH^- \tag{3.1}$$

$$Zn^{2+} + 2OH^- \rightarrow Zn(OH)_2 \tag{3.2}$$

$$Zn(OH)_2 \underset{T=70°C}{\rightarrow} H_2O + ZnO \downarrow \tag{3.3}$$

According to this mechanism above Eq. (3.1)-Eq. (3.3), the precipitation of $Zn(OH)_2$ on the working electrode (FTO in our study), caused by the generation of OH ions, which spontaneously transforms into ZnO under tempreture higher than 50 °C [126]. In our case, the bath temperature was set at 70 °C to favor the third step. Regarding to the different electrocoating current densities ($-0.5, -1, -2, -3\ mA.cm^{-2}$), the general look for the Chronopotentiograms is typical of a 3D electrocrystallization growth [127]. It can be seen that all the curves reveal three regions; ($0 - 5\ sec$) the potential decrease sharply when the current was applied.

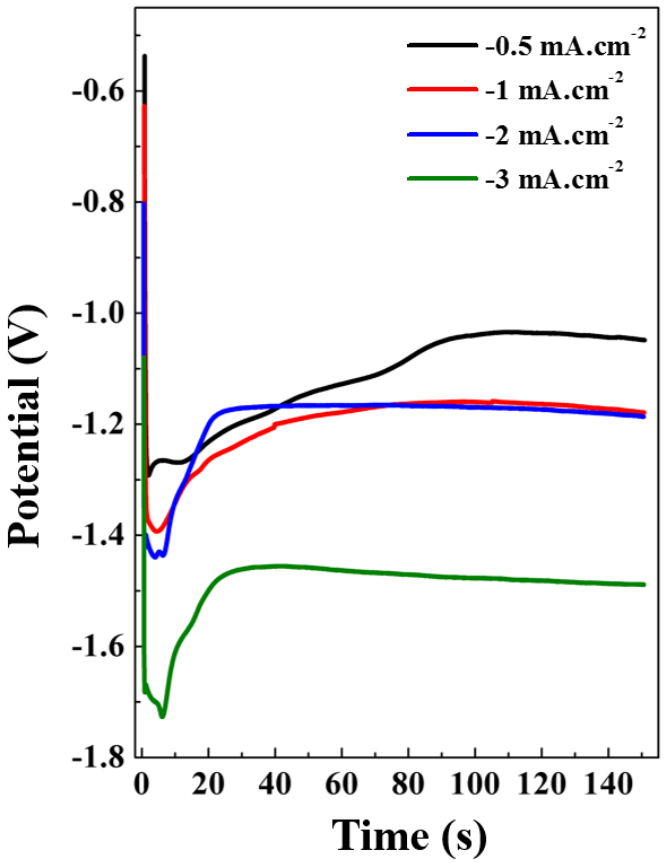

Figure 3.1: Chronopotentiograms obtained during deposition of ZnO nanosheets at different current densities: -0.5, -1, -2, -3 $mA.cm^{-2}$ from an electrolyte containing 80 mM $Zn(NO_3)_2$ and 100 mM (KNO_3) at 70 °C for150 sec.

At 5 sec, the potential get to minimum value, which indicate the initial growth stage (nucleation), which is clear that the minimum value of this inverted peak becomes less negative, when the current density decrease, that could be attributed to the generation of OH^- ions. Moreover, it is most probably due to the passivation effect in the first stage of ZnO formation, which causes a rise in the surface resistivity[24]. Second region ($5-85$ sec) for the films deposited for -0.5 and -1 $mA.cm^{-2}$, and ($5-23$ sec) for the films deposited for -2 and -3 $mA.cm^{-2}$, suggesting that the substrate becomes less conductive over time. The potential values start to increase, it can be interpreted by an initial growth stage and a completed nucleation process. Last state, a stabilization of the reaction following the constant growth of ZnO represented by a plateau favoring the deposition of ZnO films

of very good quality. The potential of deposition in the steady state decrease towards more negative values from -1 to 1.5 V when the current densitie goes from -0.5 to -3 $mA.cm^{-2}$. The best curves in terms of homogeneity of the ZnO nanostructures were obtained with -2 $mA.cm^{-2}$ and -3 $mA.cm^{-2}$. However, in the potentiostatic mode; -1.3 V/ECS was the optimum potential in the same conditions [128]. For that, the intermediate current density of -2 $mA.cm^{-2}$ could be the best result, from a compatibility point of view with galvanostatic mode compared with electrodeposited thin films at lower or higher current densities. In next parts of our study, this initial result will be confirmed.

3.2.1.2 Mott-scottky Measurements

Through Mott–Schottky ($M-S$) measurements; the conduction type, the flat band potential (E_{fb}), and the estimated of major charge carrier densities of ZnO semiconductor can be studied. This method is based on the Schottky barrier formation at the interface semiconductor/electrolyte. These electronic properties were determined by studying the semiconductor electrolyte interface. Fig. (3.2) shows the Mott-Schottky plots of ZnO nanostructures, obtained at different current densities ($-0.5, -1, -2, -3$ $mA.cm^{-2}$), in 0.5 M KNO_3 solution and fixed frequency of 20 KHz. Briefly, it is clear that the slope of the linear part of the curves of the capacitance as a function of the applied potential in the depletion zone shows positive slope. This confirms that the samples prepared for different current densities are $n-type$ semiconductors which is known from earlier for ZnO. The depletion layer capacitance $C^{-2} = f(E)$, at fixed frequency, was measured and presented as an $M-S$ plot following the Eq. (2.1) [102]. From the slope of $M-S$ plots which the line interpolate until $C = 0$ gives the flatband potential (E_{fb}). While the donor concentration (N_D) of the different samples have been calculated thanks to this slope. Since the donor density N_D is determinate, the diffence between Fermi level and the conduction band edge can be also calculated from Eq. (3.4):

$$d = E_{CB} - E_F = \frac{KT}{e}\, ln\left(\frac{N_C}{N_D}\right) \tag{3.4}$$

Where N_C is the effective density of states in the conduction band. It is assumed that all states below Fermi level (E_F) are completely filled and those above are vacant. Indeed, N_C can be calculated as follows

$$N_C = 2\left(\frac{2\pi m^* KT}{h^2}\right)^{3/2} \tag{3.5}$$

Where m^* is the electron effective mass, determinate by Enright and Fitzmaurice[129]. In the case of ZnO, $m^* = 0.27me$.

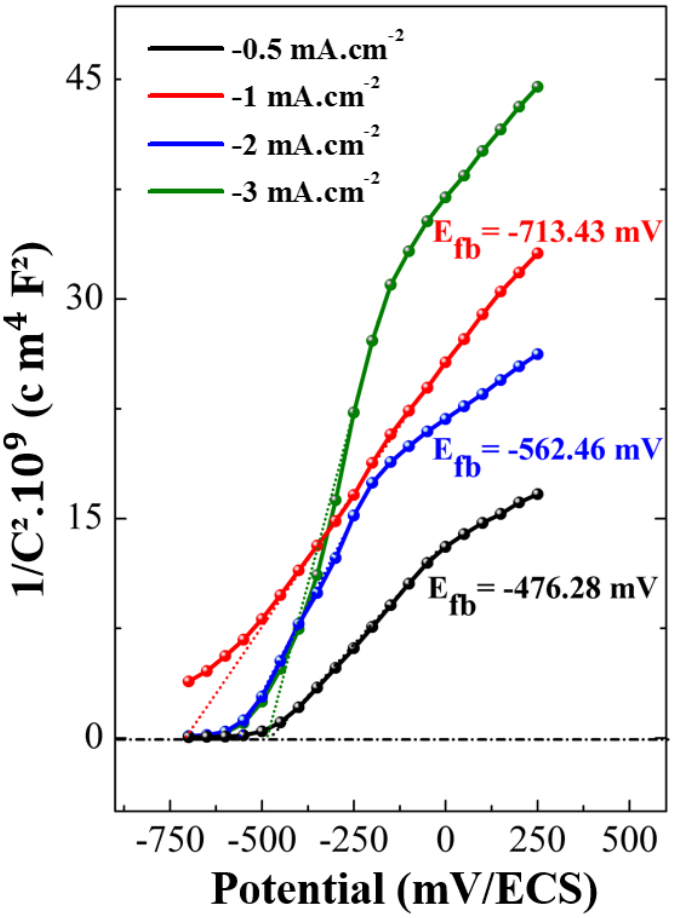

Figure 3.2: Mott–Schottky plots of ZnO nanosheets at different current densities: -0.5, -1, -2, -3 $mA.cm^{-2}$. The corresponding flat band potential values are indicated for the different plots.

The E_{fb}, N_D and d calculated from $M-S$ analysis are summarizes in Tab. (3.1). It is clear that E_{fb} is cathodic for different samples. From $I = -0.5mA.cm^{-2}$ to $-2mA.cm^{-2}$

the donor densities increase from 1.53×10^{20} to 5.82×10^{20} $cm-3$ when the cathodic current density applied decreases to more negative values. However, it decreases to 4.41×10^{20} $cm-3$ for $I = -3\ mA$. The resource of these carrier are the oxygen vacancies. The difference between Fermi level and the potential of the edge of the conductive band are in negative values, which means that Fermi level is inside the conduction band in the different samples. In the edge of the conduction band $N_C = N_D$, higher the number of carriers, the level of fermi begins to break into the conduction band (degenerate material). It's worthnoting, that these values are proportional with N_D in absolute value. The best sample across the Mott-Schottky analysis is about $-2mA.cm^{-2}$.

Table 3.1: Current density effect $(-0.5, -1, -2, -3mA.cm^{-2})$ of ZnO nanostructures on the donor density charge (N_D), the flat band potential(E_{fb}), the depletion zone thickness (W), and the effective density of states in the conduction band $(E_{cb} - E_F)$.

Sample	$\mathbf{E_{fb}}$**(mV/ECS)**	$\mathbf{N_D}(cm^{-3})$	**W(nm)**	$\mathbf{N_C}(cm^{-3})$	$\mathbf{E_{cb} - E_F}$**(eV)**
-0.5mA	-713.43	1.53×10^{20}	6.663	3.5×10^{18}	-97
-1mA	-562.46	3.36×10^{20}	3.994		-117
-2mA	-476.28	5.13×10^{20}	2.974		-131
-3mA	-480.98	4.41×10^{20}	3.224		-124

3.2.1.3 Photocurrent analysis

Photocurrent-Time measurements are performed to determine the conduction type and photoresponse of the deposited ZnO nanostructures. Fig. (3.3) shows the photocurrent of ZnO samples successfully elaborated with different current densities (-0.5, -1, -2, $-3\ mA.cm^{-2}$). In order to evidence photoeffects, the illumination was alternating light and dark using chopped mode. The measurement have been taken in $0.5M\ Na_2SO_4$ and without bias potential. The photocurrent in all the samples remains constant and very close to $0.0mA$ in the dark.

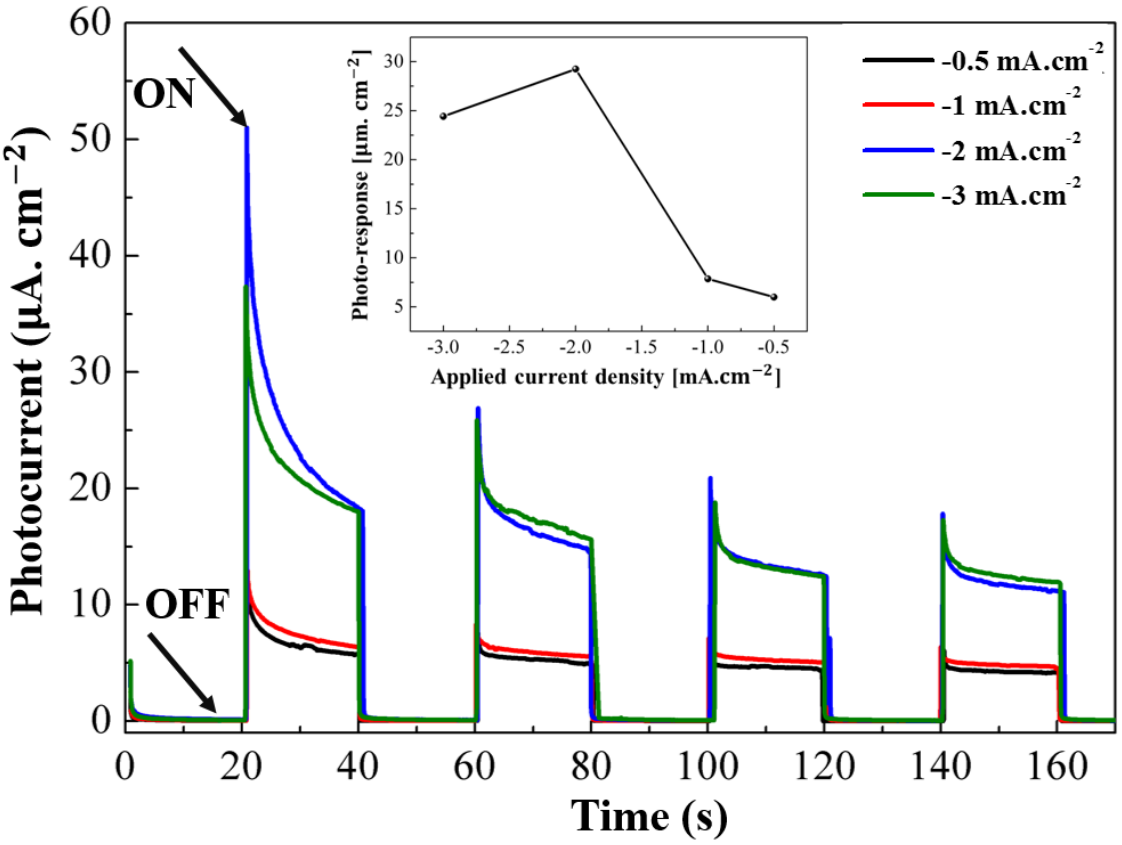

Figure 3.3: Photocurrent measured from ZnO nanosheets at different current densities: $-0.5, -1, -2, -3\ mA.cm^{-2}$. Inset: the variation of the average photoresponse as function of the deposition current density.

Rectangular responses have been observed under illumination with reproducible photocurrent with time, in which, increase in the current was noted (anothodic photocurrent), indicating that the deposited ZnO films behave as n-type semiconductor in different applied current density, this result confirms which that of reached through Mott-Schottky analyses. The average value of the photoresponse was calculated for each sample, which are: 6, 7.85, 29.25 and 24.42 μA, when the current density goes towards more negative values, as shown in the inset of Fig. (3.3). The highest photocurrent was obtained for $I = -2.0\ mA$ due to the high carrier concentration of this sample reported in Mott-Schottky results.

3.2.2 Structural characterization

The ZnO nanostructures electrodeposited over a current range from -0.5 to -3 $mA.cm^2$ were studied by XRD measurements to investigate their structural proprieties. Fig. (3.4) shows XRD spectra of ZnO films obtained on FTO substrate, where only peaks corresponding to the diffraction of ZnO thin layers were observed.

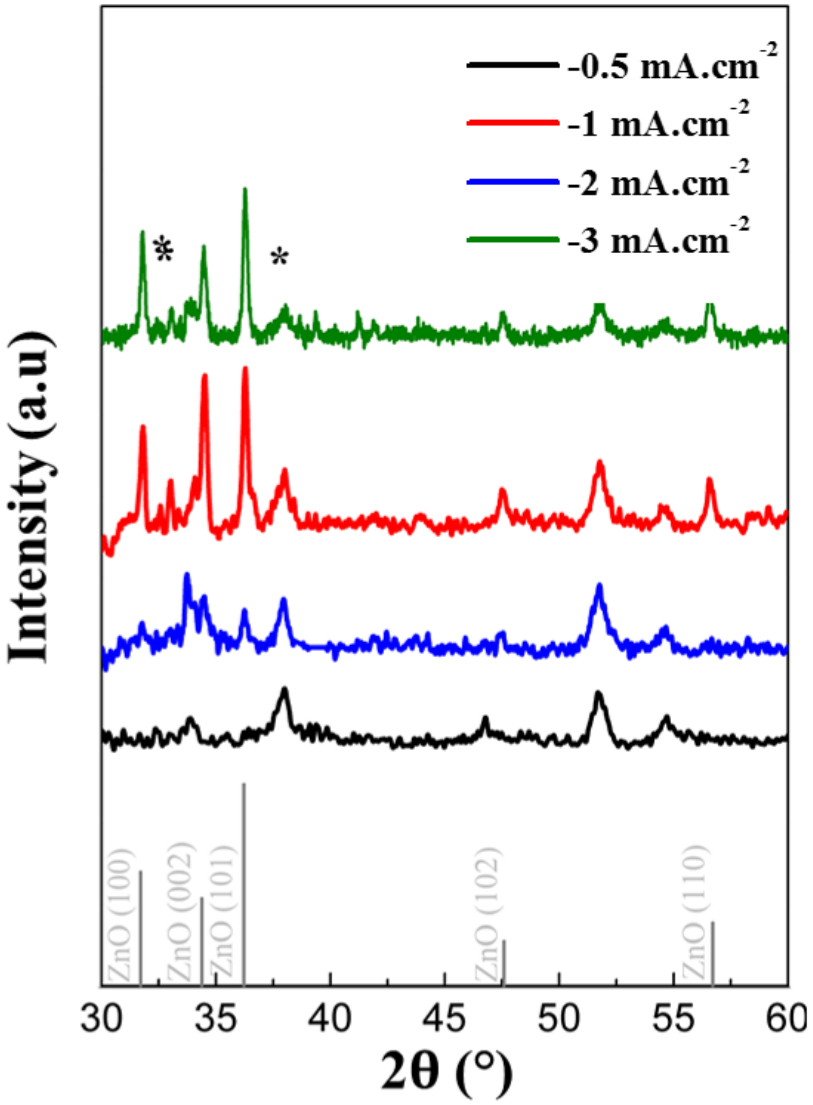

Figure 3.4: XRD patterns of ZnO nanosheets at different current densities: -0.5, -1, -2, -3 $mA.cm^{-2}$ on FTO. (*) Indicate diffraction peaks corresponding to the FTO substrate.

All these diffraction peaks can be assigned to those of wurtzite ZnO phase, while no

additional peak or impurities were seen according to (JCPDS no. $36-1451$). The asterisks are attributed to FTO substrates peaks. All the samples show (100) as preferential orientation, where the intensity of the peak is increased with increasing deposition current density from -0.5 to $-2\ mA.cm^{-2}$. However it decreased when the current density goes to more negative value. For the case of $I=-2\ mA$, the intensity of the peak is equal to that of (002) orientation along the c-axis which is normal to the FTO substrate surface. This is attributed to the ZnO deposition reaction, in which a competition between (002) and (101) orientations. It can be seen, from Fig. (3.4), that the texturation is closely related to the applied current density, and this goes well with M.Izaki results [130].

3.2.3 Topographical characterization

Through Atomic Force Microscopy (AFM), the topographies of the obtained ZnO films were characterized. Fig. (3.5) shows $2D$ AFM plots of ZnO samples deposited under different current density. It can be seen that the surface area becomes more field when the applied current goes to more negative values, which can be explained by the proportionality between the initial growth stage and the completed nucleation process of the ZnO films and the covered surface, this is in good agreement with the chronopototiometric plots. On the other hand, the root mean square (RMS) takes values of 61.960, 73.162, 88.586, and $78.800nm$ for $-0.5, -1, -2, -3\ mA.cm^{-2}$, respectively, where it is clear that the roughness increases with decreasing the current density from -0.5 to $-2.\ mA.cm^{-2}$, then decreases for higher applied current. This can be related to the texturation evaluation, in which the rougher surface corresponds to $-2\ mA.cm^{-2}$, when $I(101)=I(002)$.

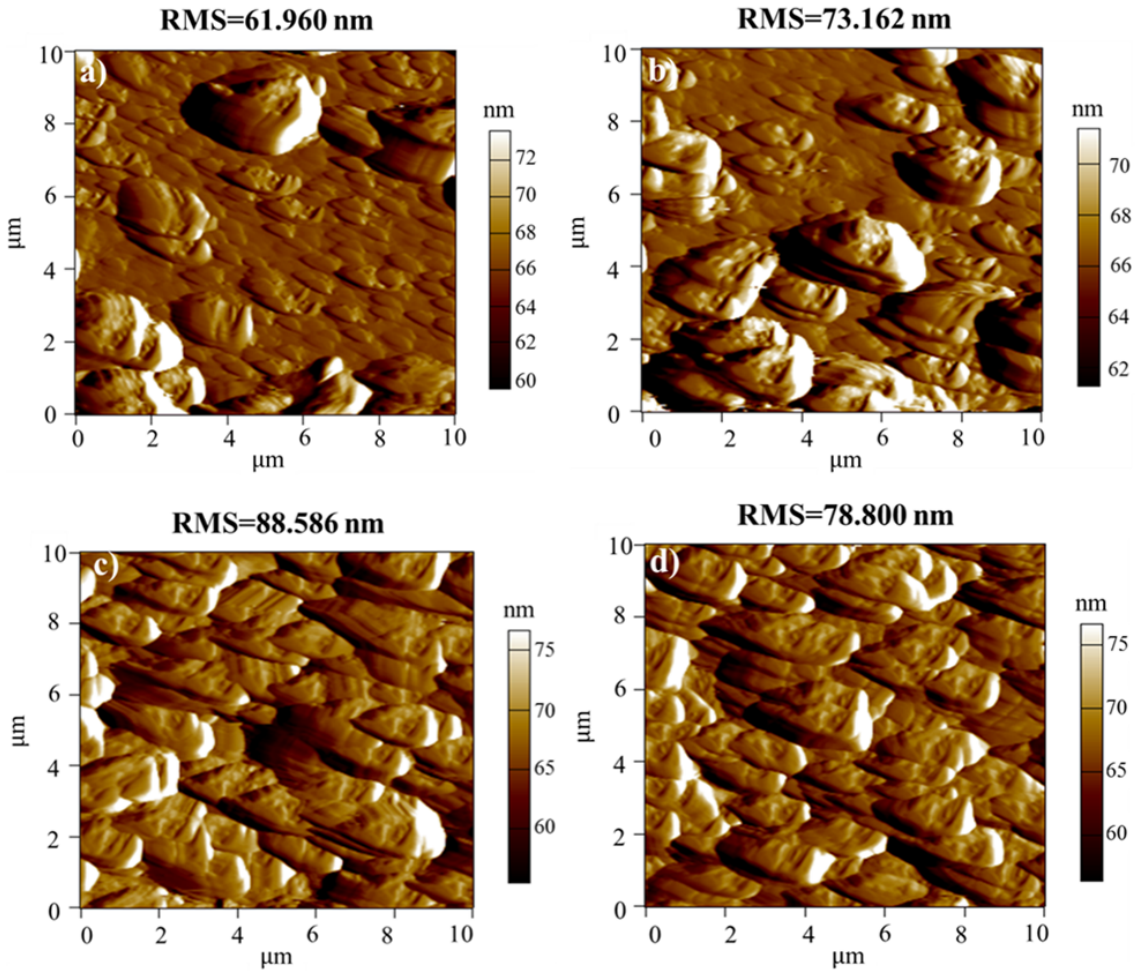

Figure 3.5: Tapping mode 2D AFM images ($10 \times 10\mu m^2$) of ZnO nanosheets electrodeposited at different current densities: a) -0.5,b) -1, c) -2 and d) -3 $mA.cm^{-2}$. The roughness for each sample was also indicated.

3.2.4 Optical characterization

Optical measurements, using UV-visible spectrophotometer, of ZnO films elaborated under different current densities were carried out at ambient temperature. The spectral of which extends over is from 200 to 1200 nm. Fig. (3.6)(a) shows the optical transmittance spectra of different samples. It can be clearly seen that the shape of the set of transmission spectra is identical whatever the applied current density. It seems that the light is totally absorbed in the range < 300 nm for the different spectra. Practically, the transmittance

increases rapidly from 300 nm, towards a maximum value (at 400 nm) due to wide band gap of ZnO, as the wavelength increases for all the samples, in which a minimal optical absorption can be occurred, because it is clear that the incoming photon energies are less than the band gap energy of ZnO thin films. In visible spectrum (400 nm − 800 nm) the transmittance is strongly depended on the applied current density during the films elaboration. The average values were recorded to 55, 45, 18, and 38% for $-0.5, -1, -2, -3$ $mA.cm^{-2}$ respectively, as shown in Tab. (3.2).

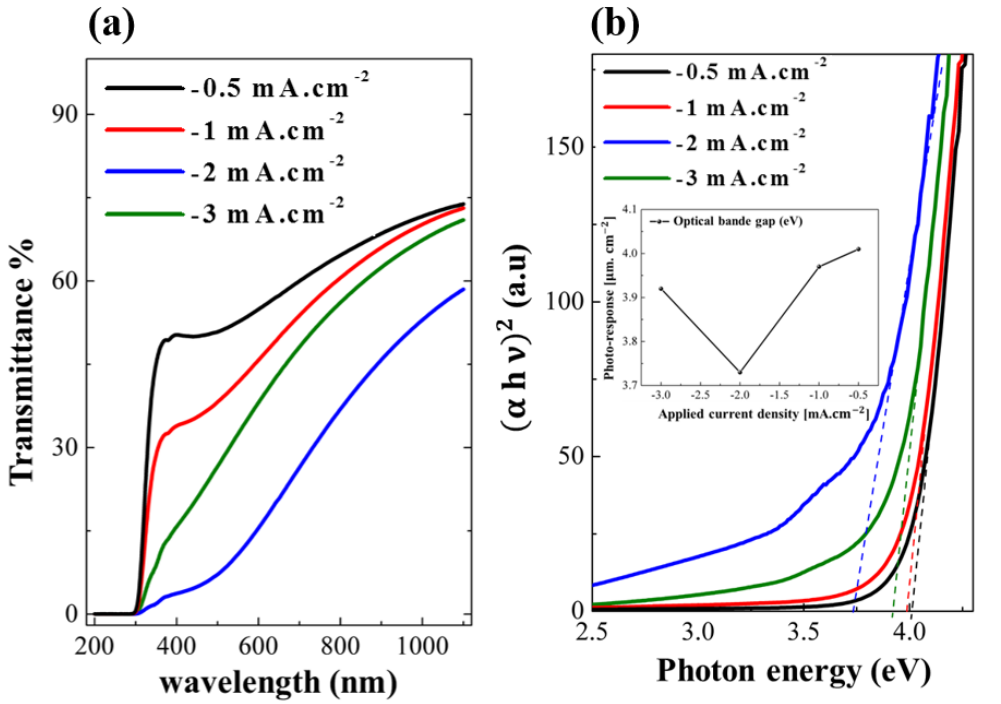

Figure 3.6: a) Transmittance spectra ZnO nanosheets at the different current densities. b) Dependence of $(\alpha h\nu)^2$ versus photon energy (eV) for ZnO nanosheets. Inset: the variation of the optical gap values as a function of the deposition current density

On the other hand, the transmittance can reach values around 72% in the near infrared range for $-0.5, -1$, and -3 $mA.cm^{-2}$. However, it does not exceed 58% in the case of -2 $mA.cm^{-2}$. This can be explain by the loss of energy at the entrance under the scattering phenomenon. Yamamoto et al.[131] stated that the optical transparency of ZnO films is rather strongly related to the roughness of the surface and to the existence of voids and pits as surface defects. This may be the reason for the lowest transmission factor

of the film prepared at $-2\ mA.cm^{-2}$, which has a rough surface. Thus, higher is the roughness, higher is the scattering, lower is the transmittance. It can be seen that, this result is in good agreement with AFM topography. The optimum film will be used just as a before layer for ZnO nanowires. So, roughness or weak transmittance it has nothing to do with the quality of film when it will not be used as a window layer (the superficial one). Fig. (3.6)(b) shows the $(\alpha h\nu)^2$ vs. the photon energy $(h\nu)$ to determinate the optical band gap for the different ZnO films. In order to investigate the effect of the applied current density to ZnO optical band gap energy, the Tauc relation (Eq. (2.5))[110] is used. The optical band gap can be also obtained by extrapolating downwards to the photon energy axis for the corresponding straight lines [110]. From the inset of Fig. (3.6)(b), we can see the variation of the band gap energy, for the different samples. It seems clear that Eg decreases from 4.01 to $3.73ev$ when the current density goes from $-0.5\ mA.cm-2$ to -2 $mA.cm^{-2}$. Moreover, it increases to 3.92 eV, for $-3\ mA.cm^{-2}$.

Table 3.2: Current density effect $(-0.5, -1, -2, -3\ mA.cm^{-2})$ of ZnO nanostructures on the transmittance in different optical domains.

Sample	**Optical domain**		
	UV region	**Visible region**	**Near infrared region**
	(300-400 nm)	(400-800 nm)	(800-1200 nm)
-0.5 mA	46.91%	55%	71.78%
-1 mA	30.59%	45%	69.78%
-2 mA	2%	18%	53%
-3 mA	8.86%	38%	66.93%

In summary, the different proprieties of ZnO nanostructures as function of the applied current density have been studied. The results were varying bikes focusing on the most important points including the deposit quality, the density of load carrier, the most intense orientation following the plan (002), and so on. We can note that the film developed under

the current $-2\ mA.cm^{-2}$ is the optimal film in this study based on the results of Tab. (3.3). In the second part of this work, this film will be compared with the another one developed under the same conditions by the potenstiostatic mode.

Table 3.3: Current density effect ($-0.5, -1, -2, -3\ mA.cm^{-2}$) of ZnO nanostructures on the physical and electrochemical properties.

Sample	**-0.5 mA**	**-1 mA**	**-2 mA**	**-3 mA**
Film thickness [nm]	389.3	470.8	803.3	366.9
Optical transmittance [%]	71.78%	69.78%	53%	66.93%
RMS [nm]	61.960	73.162	88.586	78.800
Band gap [eV]	4.01	3.97	3.73	3.92
Carrier charge density [cm^{-3}]	1.53×10^{20}	3.36×10^{20}	5.13×10^{20}	4.41×10^{20}
Photo-response [μA]	6	7.85	29.25	24.42

3.3 Galvanostatic, and potentiostatic electrodeposition of ZnO nanostructures: comparative study for two different morphologies

The optimum current density in the previous study (galvanostatic mode) will be compared with and another sample using potentiostatic mode where the applied potential is -1.3 V in the same conditions. ZnO nanowires were prepared using electrodeposition way on FTO substrate in bath contains 0.001 M Zinc nitrate ($Zn(NO_3)_2$), and 0.1 M potatium chloride (KCl). In order to investigate the elaboration mode effect on the structural, morphological and optical properties of ZnO nanostructures we apply a constant current density (galvanostatic mode) of about $-0.125\ mA$ for the first sample and constant potential (potentiostatic mode) of about $-1\ V$ for the second one, using computer-controlled potentiostat/galvanostat (Autolab) for 15 min. And the deposition temperature held

constant at 70 °C. For each ZnO morphology; ZnO nanosheets and ZnO nanowires, two films were elaborated. ZnO nanosheets by galvanostatic mode, ZnO nanosheets by potentiostatic mode, ZnO nanowires by galvanostatic mode, and ZnO nanowires by potentiostatic mode will be noted in the rest of this paper; $ZnO^{(g)}_{(NS)}$,$ZnO^{(p)}_{(NS)}$,$ZnO^{(g)}_{(NW)}$ and $ZnO^{(p)}_{(NW)}$ respectively.

3.3.1 Electrochemical analyses

3.3.1.1 Deposition mechanism of ZnO nanostructures

Fig. (3.7)(a) show the current density and the potential variation, for $ZnO^{(p)}_{(NS)}$ and $ZnO^{(g)}_{(NS)}$ as a function of time. The two curves are recorded during the electrodeposition of ZnO nanosheets at 70 °C for 150 sec, where the elaboration mechanism of ZnO is well detailed in the first part of this chapter, expressed by Eqs. (3.5)- (**??**). It can be seen from Fig. (3.7)(a) that the chronoamperogram is typical of a 3D electrocrystallization growth[128, 132]. Three region are clearly observed ($(0-5\ sec)$, $(5-40\ sec)$, and $(40-150\ sec)$), that can be corresponding to the sudden current increase when the potential of $-1.3\ V$ was applied, which are the initial growth stage, the completed nucleation process, and the reaction stabilization following the constant growth of the ZnO film, respectively. It is worthnoting that the current minimum, which could indicate the nucleation stage, is shown exactly at 5s. It is clear that the elaborated films by potentiostatic or galvanostatic Fig. (3.7)(a) mode had the same steps and practically the same duration for the itch stage. In elaboration terms, the two samples followed an identical path of formation. On the other hand, the electrochemical deposition of ZnO nanowires can be obtained at low temprature ($< 100\ ^{\circ}C$) by reducing the O_2 [65] in the electrolyte that occurs either by a two electron process Eq. (3.6) or by a four electron process Eq. (3.7), depending on the electrolyte nature and the FTO substrate properties [133, 134].

$$O_2 + 2H_2O + 2e^- \rightarrow H_2O_2 + 2OH^- \tag{3.6}$$

$$O_2 + 2H_2O + 4e^- \rightarrow 4OH^- \tag{3.7}$$

Literally, the generated OH^- ions, due to the electrochemical reduction of O_2, increase the local pH beside the substrate leads to the precipitation of ZnO nanowires on the FTO substrate resulting from the reaction between Zn^{2+} and OH^- ions Eq. (3.8)[135]

$$Zn^{2+} + 2OH^- \rightarrow ZnO + H_2O \tag{3.8}$$

The growth of ZnO nanowires needs a relatively slow diffusion of Zn^{2+} to the FTO substrate, in comparison to the reduction of O_2 to OH^- in the electrolyte. Fig. (3.7)(b) shows, the chronoamperogram and the chronopotentiogram for ZnO nanowires.

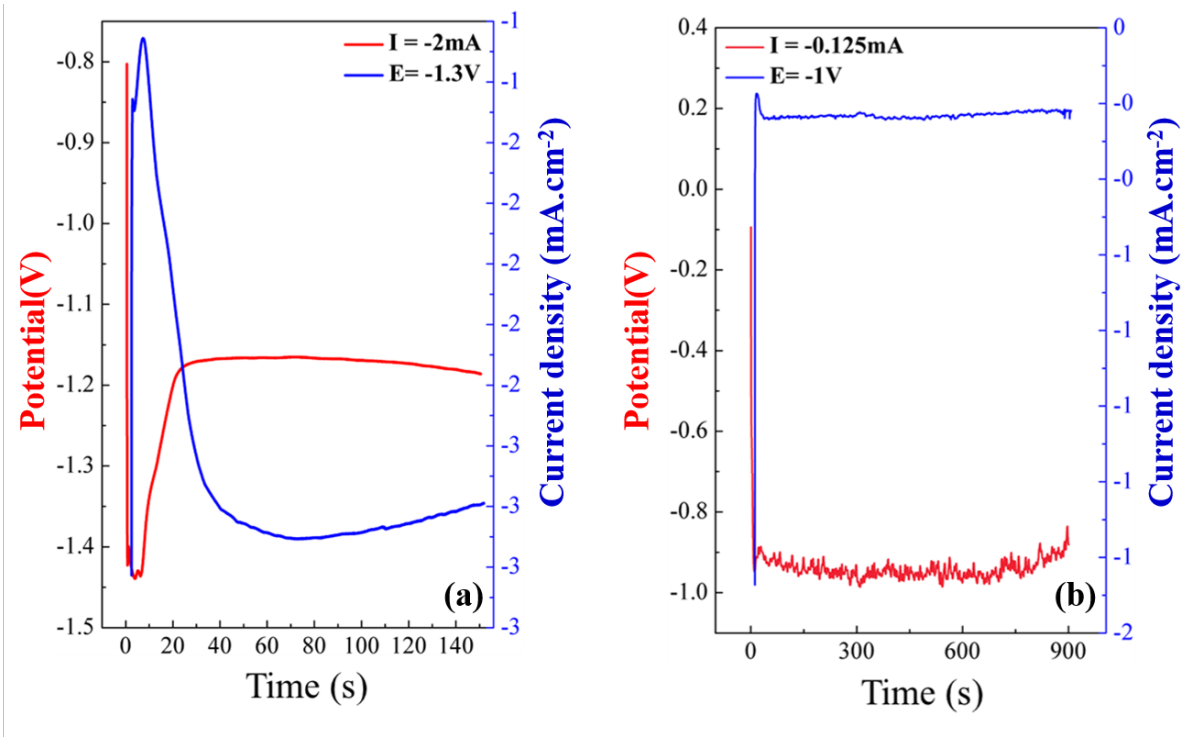

Figure 3.7: a) Chronoamperograms and Chronopotentiograms obtained during deposition of ZnO nanosheets b) Chronopotentiograms and Chronoamperograms obtained during deposition of ZnO nanowires from an electrolyte containing $1mM$ $Zn(NO_3)_2$ and $100mM KCl$ at 70 °C for $15min$.

Both of curves recorded during electrodeposition of ZnO films on an FTO substrate, and temperature kept at 70 °C for 900 sec. After studying their effect, $-1V$ vs. SCE and -0.125 $mA.cm^{-2}$ are, respectively, the chosen potential and current density for the $ZnO^{(p)}_{(NS)}$,$ZnO^{(g)}_{(NS)}$. These conditions favor the deposited ZnO quality[136]. As known in ZnO thin films, the formation multi-step process is starting by the development of OH^-

in the electrolyte resulting from the reduction of nitrate anions (NO_3^-) to nitrite (NO_2^-) , until the precipitation of ZnO nanowire on FTO substrate (Eqs. (3.6) - (3.8)). From Fig. (3.7)(b), it seems clear that, the two curves are typical of a 3D electrocrystallization growth [127, 132] and three steps are observed. It can be seen, at $(0-5\ sec)$, two identical, upside down peaks are observed, corresponding nucleation process. After that, a perfect stabilization of reaction following the constant growth of ZnO nanowires. Both films were passed by the same path of formation except the mode of excitation. However, will this influence the electrical, optical and structural properties of the films or not?

3.3.1.2 Mott-scottky Measurements

In order to investigate the mode effect into the electrical properties, Fig. (3.8) shows Mott-Schottky plots of different ZnO nanostructures.

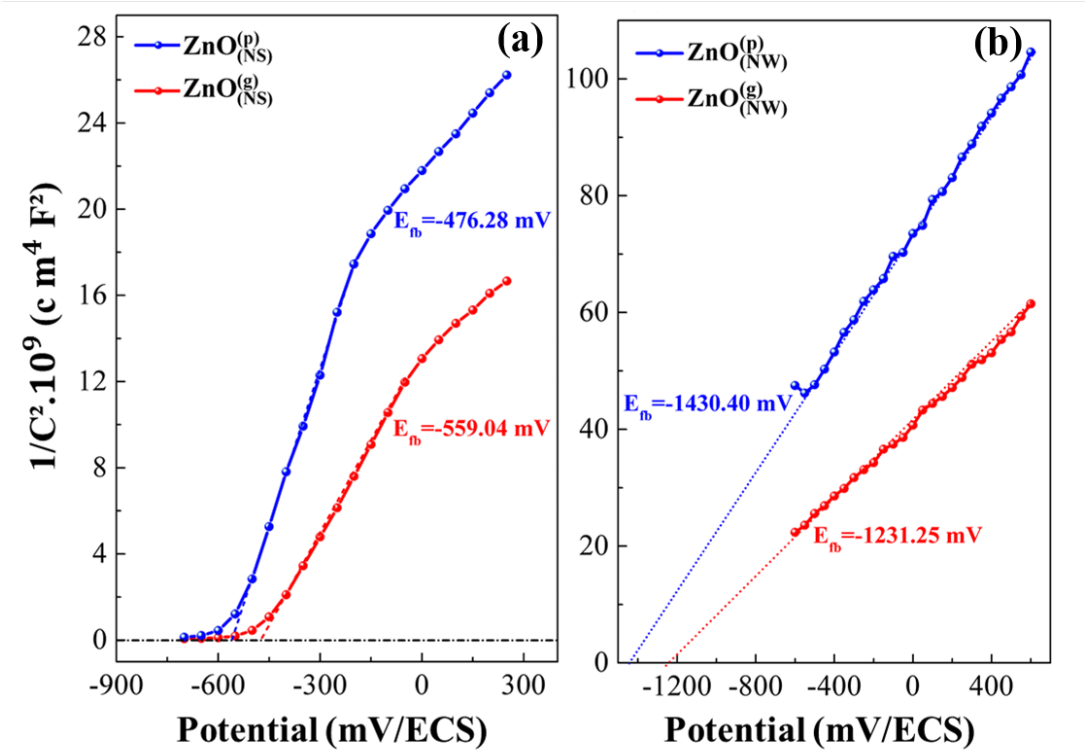

Figure 3.8: Mott–Schottky plots for ZnO nanostructures elaborate under potentiostatic, and gavanistatic modes. a) nanosheets, b) nanowires. The corresponding flat band potential values are indicated for the different samples

The measurements have been done in a 0.5 M Na_2SO_4 solution with a fixed frequency

of 20 KHz. Briefly, it looks clear that the slope of the linear part of the capacitance curves is exhibited positive for the different samples, which indicates $n-$type semiconductors that is early well known for ZnO. The estimated carrier concentration (N_D) for $ZnO^{(g)}_{(NS)}$, $ZnO^{(p)}_{(NS)}$, $ZnO^{(g)}_{(NW)}$ and $ZnO^{(p)}_{(NW)}$ have been calculated through Eq. (2.1). For both morphologies; ZnO nanosheets and ZnO nanowires, the electron carrier concentrations increase from 3.32×10^{20} to 5.13×10^{20} $cm-3$, and from 3.16×10^{20} to 5.43×10^{20} cm^{-3}, respectively, when the mode is transformed from potentio to galvano (see Tab. (3.4)). Moreover, the density order is in good agreement with the literature[137] for the different samples. It seems clear that the elaborated samples under constant current density had higher donor concentration and this could be due to the faster deposition rate of ZnO. It is well known that the ZnO faster growth can create some zinc interstitials or oxygen deficits[63].

Table 3.4: Mode effect on the donor density charge and the flat band potential of ZnO nonosheets and ZnO nanowires.

Sample	$\mathbf{E_{fb}}$**(mV/ECS)**	$\mathbf{N_D}$**(cm^{-3})**
$\mathbf{ZnO^{(NS)}_{(p)}}$	-559.04	3.32×10^{20}
$\mathbf{ZnO^{(NS)}_{(g)}}$	-476.28	5.13×10^{20}
$\mathbf{ZnO^{(NW)}_{(p)}}$	-1231,25	5.43×10^{20}
$\mathbf{ZnO^{(NW)}_{(g)}}$	-1430,40	3.16×10^{20}

3.3.1.3 Photocurrent analysis

In order to confirm the conduction type and to determine photoresponse of the ZnO films, photocurrent-time measurements are taking place in this part of study. $ZnO^{(g)}_{(NS)}$, $ZnO^{(p)}_{(NS)}$, $ZnO^{(g)}_{(NW)}$ and $ZnO^{(p)}_{(NW)}$ samples are recorded under chopped light in 0.5 M Na_2SO_4 and 0 V vs.SCE as an applied potential. Fig. (3.9)(a) shows the photocurrents response as a function of time for ZnO nanosheets formed by galvanostatic and potentiostatic mode. In the dark, the current remains constant, which is very close to 0.

While, under the light, anodic photocurrents are observed as rectangular responses form for both. This anodic photoresponse confirms the n-type behavior of semiconductors and that is in good agreement with Mott-Schottky analyses. The average value during the 180 *sec* of the generated photocurrent were; 29.425 and 30.627$\mu A.cm^{-2}$ for $ZnO^{(g)}_{(NW)}$ and $ZnO^{(p)}_{(NW)}$, respectively. Practically, no mode effect is observed for the photoresponse of ZnO nanosheets. Fig. (3.9)(b) presents recorded photoresponse as function of time under chopped light. The two curves confirms that both of ZnO nanowire samples are n-type semiconduction, when the average responses are2.85 and 2.79 $\mu A.cm-2$ for $ZnO^{(g)}_{(NW)}$ and $ZnO^{(p)}_{(NW)}$, respectively, which are practically similar. However, it looks clear that the photoelectrochemical stability of $ZnO^{(p)}_{(NW)}$ that elaborated by a constant potential is better than that elaborated by applying a constant current. It is worth noting that the high values of generated current by nanosheets compared to that of nanowires are may be due to the high absorbance of nanosheets caused by the thickness of films and not by the performance of the samples.

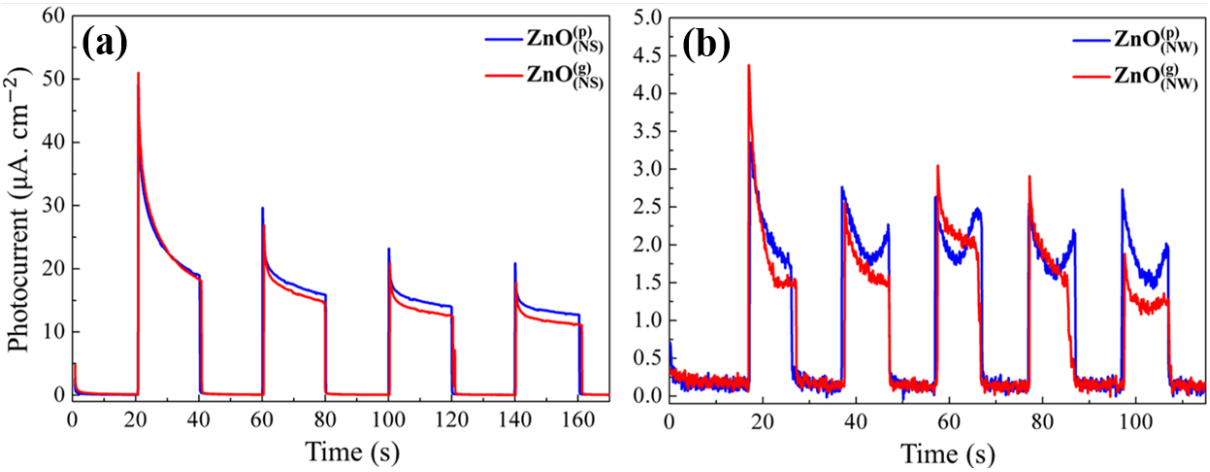

Figure 3.9: Photocurrent measured from for ZnO nanostructures elaborated under potentiostatic, and gavanistatic modes. a) nanosheets, b) nanowires.

3.3.2 Structural characterization

X-ray diffraction has been performed on the different layers, where the corresponding diffractograms are shown in Fig. (3.10). The microstructural evolution of ZnO nanosheets and ZnO nanowires were studied through this XRD spectra. To further ensure the cor-

rect identification for the different peaks, JCPDS cart had been used. The asterisks are attributed to FTO substrates peaks. In Fig. (3.10)(a), the two patterns of $ZnO^{(g)}_{(NS)}$ and $ZnO^{(p)}_{(NS)}$ shows clearly polycrystalline materials. Moreover, all orientations are in good accord with those of the wurtzite (hexagonal) pure ZnO structure (JCPDS no.$36-1451$). The intensest diffraction peak corresponds to (101) orientation plane, accompanied by the presence of (100), (002), (102), and (110) varying degrees. A similar disparity in peaks intensity has been reported elsewhere[97] for ZnO nanospikes. In order to quantify exactly the mode effect into the structural properties, average grain size and texturation coefficient have been calculated using Scherrer's Formula. The results were summarized in Tab. (3.5). Also, the XRD patterns of $ZnO^{(g)}_{(NW)}$ and $ZnO^{(p)}_{(NW)}$, that obtained directly on FTO substrates after 15 min of electrodeposition, are shown in Fig. (3.10)(b). Briefly, only the peaks corresponding to the ZnO diffraction have been observed without impurities according to (JCPDS no. $36-1451$). Furthermore, (002) is the most intense peak for both, which could cover the rest. That may illustrate that there is a growth of nanostructure perpendicular to the substrate surface. However, the $ZnO^{(p)}_{(NW)}$ substrate is well covered in comparison of that of $ZnO^{(g)}_{(NW)}$, because the peaks corresponding to the FTO are little observable. This could be explained that the elaboration rate was higher, in which the film is thicker. Here, it can be seen, that the texturation is not significantly related to the mode of elaboration in comparison to what it had been with the current density effect. In order to quantify the mode effect into the structural properties of the synthesized ZnO nanosheets and ZnO nanowires, the texture coefficient and the average crystallite size (D) were calculated and summarized in Tab. (3.5). Where D was achieved using Scherrer's Formula Eq. (2.3). It can be seen from Tab. (3.5) that the average crystallite size decreases a little bit by changing the mode from potentiostatic to galvanostatic. The results are inversely proportional to Mott-Schottky measurements. As well as The texture factor (f) as function of the ratio between the (002) and (101) peaks intensity was calculated through the following equation Eq. (3.9) [138]

$$f = \frac{\left(I^{(002)}/I^{(101)}\right) - \left(I_0^{(002)}/I_0^{(101)}\right)}{\left(I^{(002)}/I^{(101)}\right) + \left(I_0^{(002)}/I_0^{(101)}\right)} \tag{3.9}$$

Where the results are in Tab. (3.5). It can be seen that for $ZnO^{(g)}_{(NW)}$ and $ZnO^{(p)}_{(NW)}$, the texture factor is 90.36% and 86.53% respectively. Which shows a significant improvement on the nanowire crystallization.

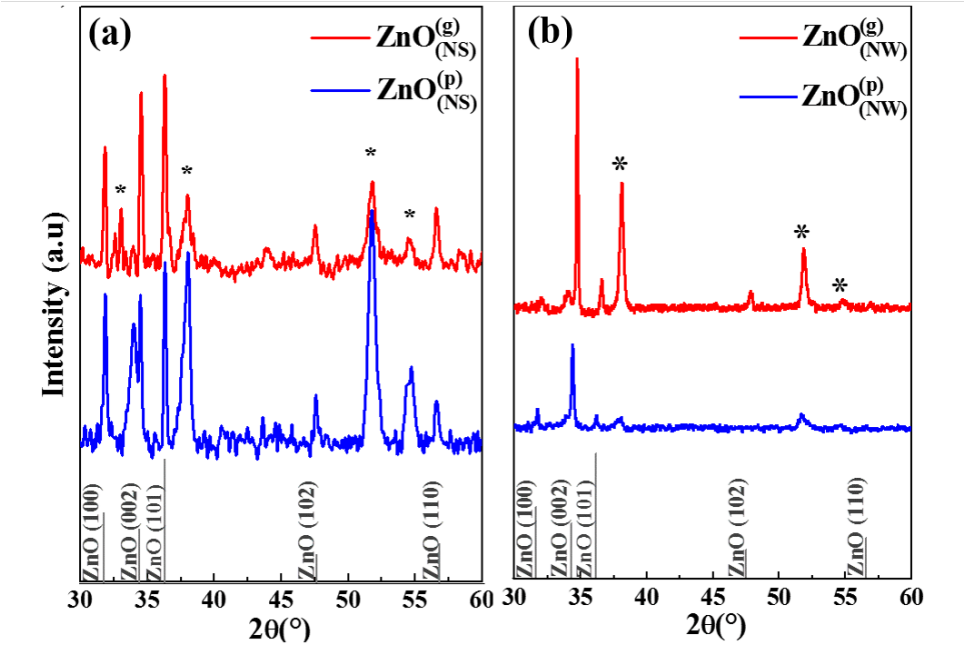

Figure 3.10: *XRD* patterns of *ZnO* nanostructures elaborate under potentiostatic, and gavanistatic modes (a nanosheets, b) nanowires. (*) Indicates diffraction peaks corresponding to the FTO substrates.

Table 3.5: Mode effect on the film thickness, and structural properties of *ZnO* nonosheets and *ZnO* nanowires.

Sample	$\mathbf{ZnO^{(NS)}_{(p)}}$	$\mathbf{ZnO^{(NS)}_{(g)}}$	$\mathbf{ZnO^{(NW)}_{(p)}}$	$\mathbf{ZnO^{(NW)}_{(g)}}$
Film thickness [nm]	667.0	803.3	1170.6	860.8
Texturation coefficient $f((002)/(101))$	0.29956	0.34827	0.86538	0.90626
Grain size [nm]	55.529	47.781	19.219	18.370

3.3.3 Optical characterization

To investigate the presence of the mode effect into the optical proprieties, the transmittance (%) of the different samples, in the range $(200 - 1200\ nm)$, have been measured. Fig. (3.11)(a) shows the optical transmittance spectra of ZnO nanosheets according to wavelength (nm). It looks clear, that both, $ZnO^{(g)}_{(NS)}$ and $ZnO^{(p)}_{(NS)}$, followed the same pace. At $< 300\ nm$, there is no passing light. While, at the incidence of the visible spectrum (400 nm), for $ZnO^{(p)}_{(NS)}$, a 15% of light is transmitted. Against, it did not exceed 4% for the other one. Then, the transmittance takes to increase for the two films, with a difference of 25% as an average between them, until they reached in the near Infra-Red (58.39 and 73.68% respectively). This difference may be due to the high scattering phenomenon from the $ZnO^{(g)}_{(NS)}$ surface. The optical transmittance versus wavelength for the ZnO nanowires was also measured, and plotted in Fig. (3.11)(b).

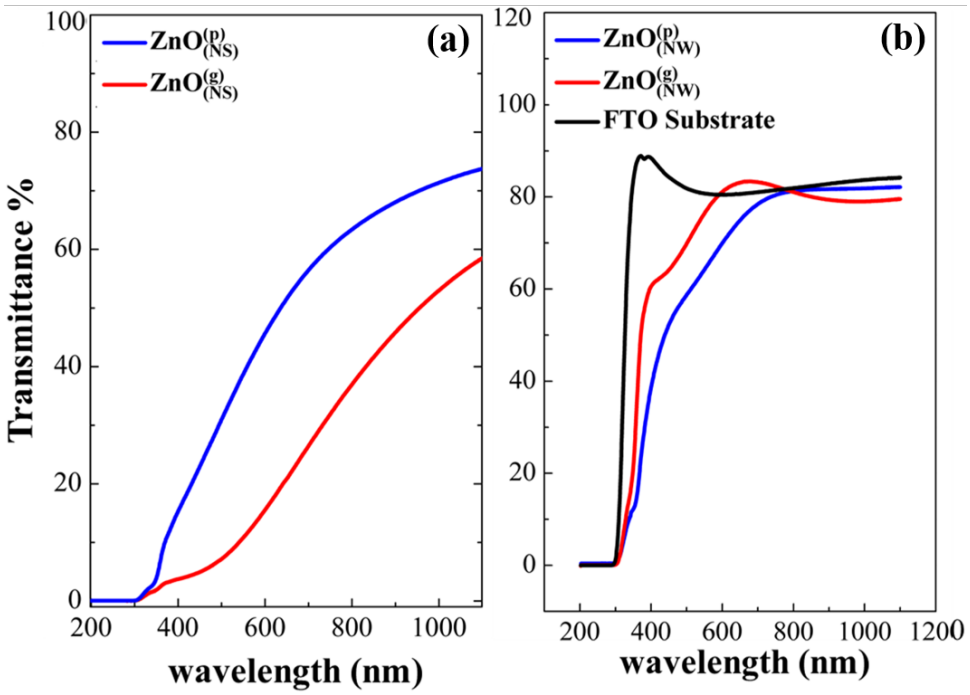

Figure 3.11: Transmittance spectra of the electrodeposited ZnO nanostructures elaborated under potentiostatic, and gavanistatic modes a) nanosheets, b) nanowires.

In the visible and near infra-red range, high values of transmittance ($> 80\%$) were obtained for both $ZnO^{(g)}_{(NS)}$ and $ZnO^{(p)}_{(NS)}$, where, $ZnO^{(p)}_{(NS)}$ curve was preceded by the other

one in the edge of the visible range showing a difference of 20% between them. After that, they became so closer. It can be seen that the transmittance remains almost constant for $ZnO^{(g)}_{(NW)}$ and $ZnO^{(p)}_{(NW)}$ about 80%, which corresponds to the stabilization of the FTO substrate. Practically, the samples became totally transparent, where, the corresponding energy is lower than the band gap energy of the thin films, in the range $200 - 1200\ nm$, which indicates that roughness is negligible, thus the surface is not scattered.

3.3.4 Morphological characterization

Fig. (3.12)(a_1) and Fig. (3.12)(a_2) show the SEM images of $ZnO^{(p)}_{(NW)}$ and $ZnO^{(g)}_{(NW)}$, respectively. Typical ZnO nanowires were obtained under both modes of elaboration with orientations not perfectly aligned. It is well known that when the nucleation stage is finished, the nanowires start to occupy the considered volume by the total electric charge. This growth in volume determines, subsequently, the length of the nanowires. After 15 min of electrodeposition, the nanowiress are found to have an average diameter of 245 nm and 185 nm, with an average length of about 350 nm and 225 nm, for $ZnO^{(p)}_{(NW)}$ and $ZnO^{(g)}_{(NW)}$, respectively. According to this result, it seems clear that the growth rate under potentiostatic mode is considerably faster. The nanowires in this study have been elaborated directly on FTO substrate without seed layer, which can introduce ameliorations. Wu and al.(2010) [139] reported that when seed layer is used, significant modifications take place; in which the density increases and the diameter reduces. In the other hand Fig. (3.12)(b_1) and Fig. (3.12)(b_2) show the SEM images of $ZnO^{(g)}_{(NS)}$ and $ZnO^{(p)}_{(NS)}$ respectively.

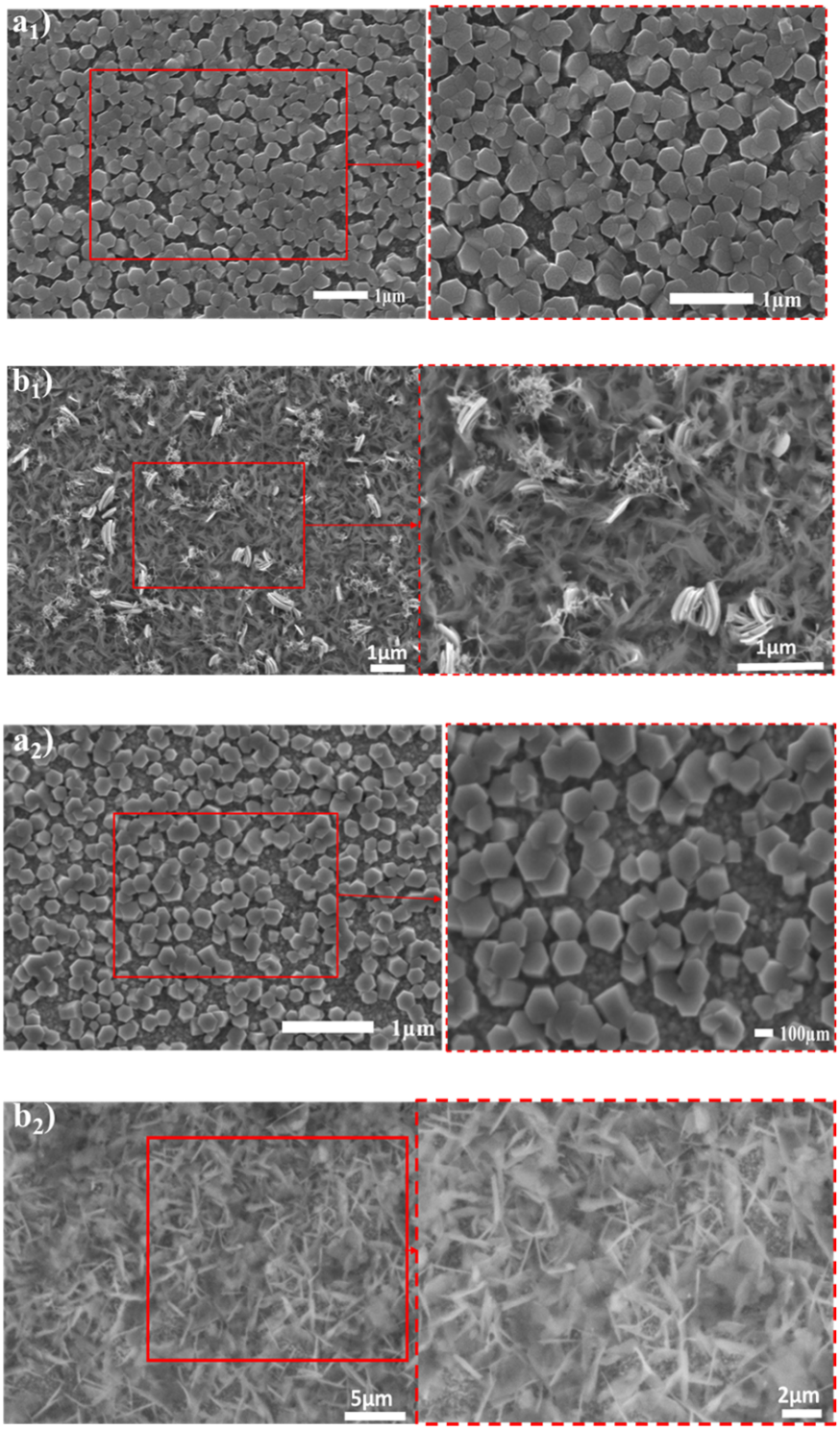

Figure 3.12: SEM images of ZnO nanostructures elaborated under potentiostatic, and galvanistatic modes for nanosheets and nanowires; a_1) $ZnO^{(p)}_{(NW)}$, a_2) $ZnO^{(g)}_{(NW)}$, b_1) $ZnO^{(g)}_{(NS)}$, b_2) $ZnO^{(p)}_{(NS)}$.

By focusing on the obtained results, it can be seen that the $ZnO^{(g)}_{(NS)}$ offred a distinctive performance that it candidates to be a seed layer for the elaborated nanowires. Finally, to better understand the mode effect into the efficiency of ZnO nanowires as well as the effect of the electrodeposition approach on the heterojunction performance, we propose to study the mode effect on the $p-Cu_2O/n-ZnO$ heterojunction for solar cell application. Where, $n-ZnO_{(NW)}\Big/ZnO^{(g)}_{(NS)}$ is the conduction layer.

3.4 Conclusion

In summary, ZnO nanosheets are very sensitive to the variation of the applied current density. However, a weak effect is observed comparing the elaboration approaches in the case of ZnO nanosheets, whereas, the $ZnO^{(g)}_{(NS)}$ are the preferred one in terms of ease. Evidently, the synthesized $ZnO^{(g)}_{(NS)}$, under $-2\ mA.cm^{-2}$, has the optimum features to be a seed layer for ZnO nanowires. On the other hand, for ZnO nanowires, when the mode is transformed from galvanostatic to potentiostatic, the diameter and the length of the nanowires have been extended. However, the crystallization ($f = 90\%$), optical transmittance, and electrochemical stability were ameliorated under the galvanostatic approach, as well as, the donor carrier density reached $5.36 \times 10^{20}\ cm^{-2}$ for $ZnO^{(g)}_{(NW)}$, which is the highest one. It is worth noting that the donor carrier density was significantly improved under galvanostatic mode regardless of the film morphology. So, it's a compromise to understand why we can not make a scientific decision about what is the best way to form nanowires without studying it in a clear application. Thus, the two films preceded by a seed layer will serve as a conductive layer in $p-Cu_2O\Big/n-ZnO_{(NW)}\Big/ZnO^{(g)}_{(NS)}$ junction for photovoltaic application.

Chapter 4

Electrochemical parameters effect on the Cu_2O nanostructures properties

4.1 Introduction

To date, there is consequently very little information regarding the influence of the current density on the structural and the morphological properties of deposits. In which, our work was reserved to the study of the current density effect on the cuprous oxide (Cu_2O) properties. Cu_2O semiconductor has been chosen, as it is nontoxic and low-cost[14, 15]. Recently, Cu_2O remains an interesting alternative to various metal oxide semiconductors thanks to the high theoretical efficiency of Cu_2O based solar cell. Thus, Cu_2O has been studied as a photocathode for the fractionation of water[68] and as absorber layer in heterojunctions for photovoltaic device[69, 70]. P-type Cu_2O gave correlated results for the majority of these applications[71]. thanks to its large range of conductivity (10^{-13} to $10^{-3}\Omega^{-1}cm^{-1}$) [16, 17] and the high absorption coefficient in the visible range[72–74] In this chapter, the current density effect on the structural, optical, and electrochemical properties is investigated. Notably, the direct effect of the applied current density on the structural properties was indicated previously by Paracchino for Cu_2O [140]. However, the constant current density of $-1mA.cm^{-2}$ was chosen by the

majority of papers, to grow the Cu_2O films under a Galvanostatic mode [116, 141–144], which can not be the optimum value for the different applications. Additionally, detailed information is attributed to the current effect on the electrochemical and physical properties through this chapter. To the best of our knowledge, the current density effect on the optical and the electrochemical features of Cu_2O films had never been reported. Furthermore, we illustrate the applied current density effect on the importance of the synthesized Cu_2O nanostructures for photoelectrochemical stability. In the second part of this chapter, the mode effect will take place in two different pH media. M.Abdelfatah et al.[143] reported a comparitive study between galvanostatic and potentiostatic effect on the Cu_2O nanostructurs, in order to investigate its influence to $p-Cu_2O/n-ZnO$ heterojunction efficiency. However, this single work was not enough for the scientific community to understand deeply which changes on the structural, optical and electrochemical properties could be introduced when the mode was changed. For that, the second part work will give many additional informations on approach effect into the elaborated Cu_2O thin films properties . While, the conductivity of Cu_2O also can be tuned by controlling the pH value of plating solutions during electrodeposition. It looks important, to express in the present study how much the film performance can be ameliorated when the pH value little bit varied.

4.2 Galvanostatic of Cu_2O nanostructures: Current density effect

In order to investigate the current density effect on the properties of Cu_2O nanostructures, Different current densities were applied, $-0.2, -0.3, -0.4$, and $-0.5 mA.cm^{-2}$ for $15 minutes$, in a bath containing a $0.05M$ copper sulfate ($CuSO_4$), $0.06M$ citric acid, and a $NaOH$ adjusting the pH at 12. When, the deposition temperature held constant at 70 °C.

4.2.1 Electrochemical analyses

4.2.1.1 Deposition mechanism of Cu_2O nanostructures

To investigate the applied current density effect on the Cu_2O nanostructures on a FTO substrate, different curent densities were applied at 70 °C. The electrodeposition mechanisme will take place as follows. Firstly, the development of OH^- resulting since the $NaOH$ was added to the solution to achieve pH of 12. Secondly the reduction of Cu^{+2} to Cu^+. The Cu_2O layers were formed by a multi-step process according to the following mechanism Eq. (4.1)-Eq. (4.3)

$$Cu^{+2} + e^- \rightarrow Cu^+ \tag{4.1}$$

$$NaOH \rightarrow Na^+ + \ OH^- \tag{4.2}$$

$$2Cu^+ + 2OH^- \underset{T=70\ ^\circ C}{\rightarrow} H_2O + Cu_2O \downarrow \tag{4.3}$$

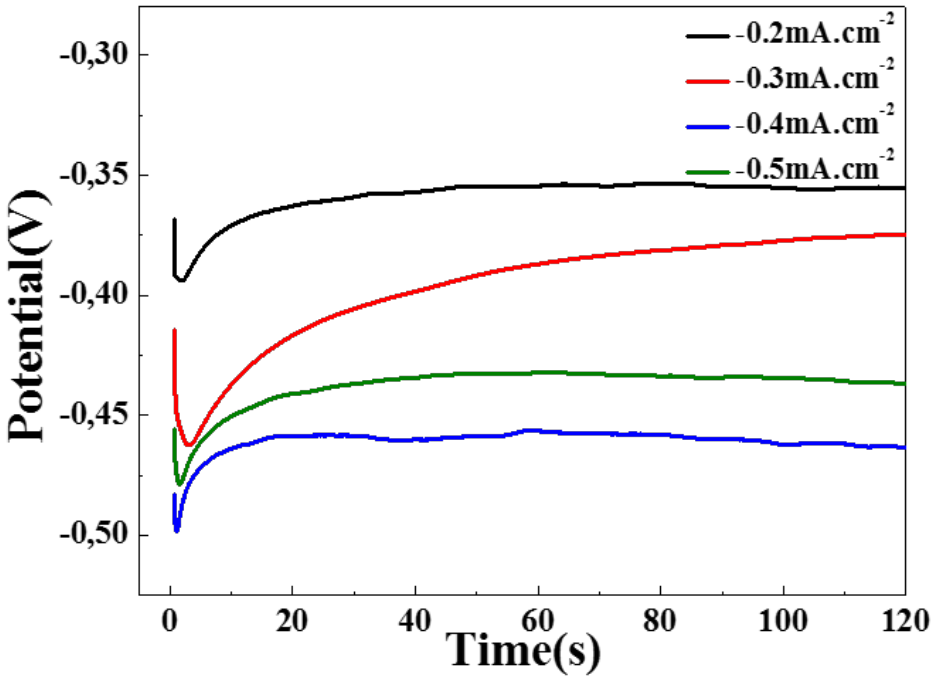

Figure 4.1: Chronopotentiograms obtained during deposition of Cu_2O thin films at different current densities: -0.2, -0.3, -0.4 and $-0.5 mA.cm^{-2}$ from an electrolyte containing $0.05M$ $CuSO_4$ and $0.06M$ citric acid, at 70°C during $15min$.

The potential transients for the deposited Cu_2O thin films at different applied current densities (-0.2, -0.3, -0.4 and $-0.5 mA.cm^{-2}$), as a function of time, are shown in

Fig. (4.1). As a general look, the chronopotentiograms are typical of a $3D$ electrocrystallization growth [127]. From the recorded graphs ($V = f(t)$), the potential attains, rapidly, a minimum value, which indicates the initial growth stages (nucleation). From Tab. (6.1), the coordinate of the nucleation step are $(2s; -0.39V)$, $(3s; -0.46V)$, $(0.96s; -0.49V)$, $(2s; -0.47V)$ corresponding to $-0.2, -0.3, -0.4$ and $-0.5mA.cm^{-2}$ respectively.

Table 4.1: Current density effect (-0.2, -0.3, -0.4 and $-0.5mA.cm^{-2}$) on the growth parameters of Cu_2O nanostructures.

Applied current density (mA)	**Nucleation stage**		**Average potential of growth stage (V)**
	Time (S)	**potential (V)**	
-0.2	2	-0.39	-0.35
-0.3	3	-0.46	-0.37
-0.4	0.96	-0.49	-0.46
-0.5	1.5	-0.47	-0.43

It is clear that the minimum value of this inverted peak becomes less negative decreasing the current density from -0.2 to $-0.4mA.cm^{-2}$. However, it re-increases for $-0.5mA.cm^{-2}$. It is well known that the plateau for the different graphs returns to the stabilization of the reaction following the constant growth of Cu_2O of very good quality. The Average potential of the growth stage in the steady state decreases towards more negative values from -0.35 to $-0.46V$ when the current density goes from -0.2 to $-0.4mA$. However, it increases to$-0.43V$ for $I = -0.5mA.cm^{-2}$ (see Tab. (6.1). Theoretically, the reaction rate and the applied current density are proportional and related by Faraday's low, given by:

$$G = \frac{MQ}{nAF\rho} \tag{4.4}$$

Where, M; is the molar mass, Q; is the total charge, F; is the Faraday constant, ρ; the bulk density of the deposit, and n; is the electron transfer per mol, A; is the working

electrode area. Therfore, Higher is the current density in absolute value, faster is the reaction, thicker is the film.

In order to research an optimum current density, all the different parameters must be taken into consideration. It is very important, in our study, to choose the current density which is able to develop the thicker film with a suitable performance.

4.2.1.2 Mott-scottky Measurements

Fig. (4.2) shows the Mott-Schottky plots of Cu_2O nanostructures obtained at different current densities ($-0.2, -0.3, -0.4$ and $-0.5 mA.cm^{-2}$), in $0.5 M Na_2SO_4$ solution and fixed frequency at $20 KHz$. Mott–Schottky (M–S) measurements are the best way to determine the conduction type, the flat band potential (E_{fb}), and the estimated major charge carrier densities of the Cu_2O semiconductor. The different curves of the capacitance as a function of the applied potential in the depletion zone show a negative slope for their linear parts. This confirms that the prepared samples for different current densities are $p-$type semiconductors, which is known from earlier for the developed Cu_2O in alkaline solution. Using Voltalab (potentiostat/galvanostat), the depletion layer capacitance $C^{-2} = f(E)$, at fixed frequency, was measured following the Eq. (2.2)[102]. The thickness of the space charge region (W) formed at the Cu_2O/electrolyte interface (depletion layer width) can be calculated as well from the equation Eq. (4.5)[145], which is directly related to the charge carrier density present in the semiconductor.

$$W = \sqrt{\frac{2\varepsilon\varepsilon_0 E_{bp}}{qN_A}} \tag{4.5}$$

From the slope of $M-S$ plots where the line interpolates until $C = 0$ gives the flat band potential (E_{fb}). Thanks to this slope, the acceptors concentration (N_A) of the different samples have been calculated (see Tab. (4.2)). It is clear that E_{fb} is anodic for different samples. When the applied cathodic current density decreases from $-0.3 mA$ to $-0.5 mA$, the acceptor density became three times higher; from 0.61×10^{19} to 1.84×10^{19} cm^{-3}.

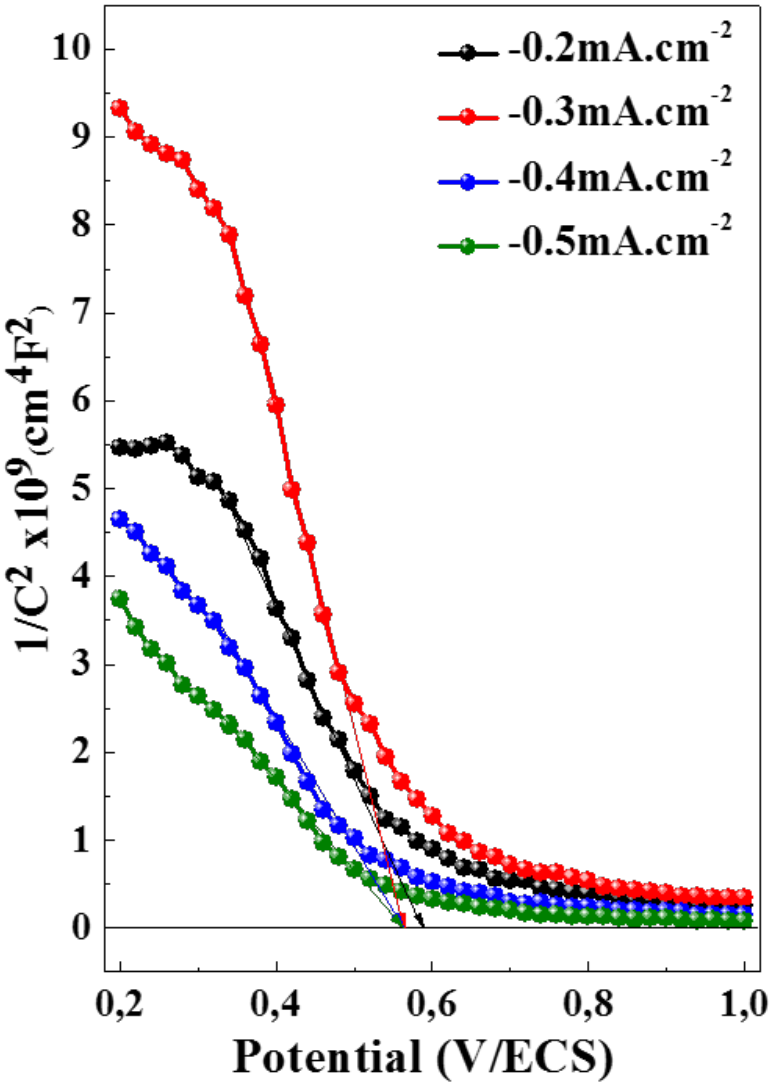

Figure 4.2: Mott–Schottky plots of Cu_2O thin films at different current densities: -0.2, -0.3, -0.4 and $-0.5 mA.cm^{-2}$. The corresponding flat band potential values are indicated for the different plots.

4.2.1.3 Photocurrent analysis

Fig. (4.3) shows the photocurrent measurements, as a function of time, of the synthesized Cu_2O nanostructures successfully elaborated under the different current densities $(-0.2, -0.3, -0.4, and -0.5 mA.cm^{-2})$. Photocurrent-Time measurements are performed to determine the conduction type and the photo-response of the Cu_2O. In order to evidence photo effects, the illumination was alternating light and dark using chopped mode

by step of $20sec$. The measurements have been taken in a $0.5MNa_2SO_4$ without bias potential. The photocurrent for the different samples remains constant and very close to $0.0mA$ in the dark. However, rectangular responses have been observed under illumination for all of the Cu_2O films. It seems clear, that the current density decreases suddenly since the sample is exposed to white light. Briefly, cathodic photocurrent was noted, to confirm the p-type semiconductor reached by Mott-Schottky analyses for the different samples regardless of the applied current density. The generated photocurrent was $-210, -160, -242$ and -606 $\mu A.cm^{-2}$, corresponding to $-0.2, -0,3, -0.4$ and 0.5 $mA.cm^{-2}$, respectively. It can be note that the photo response values are proportional to the estimate acceptor density.

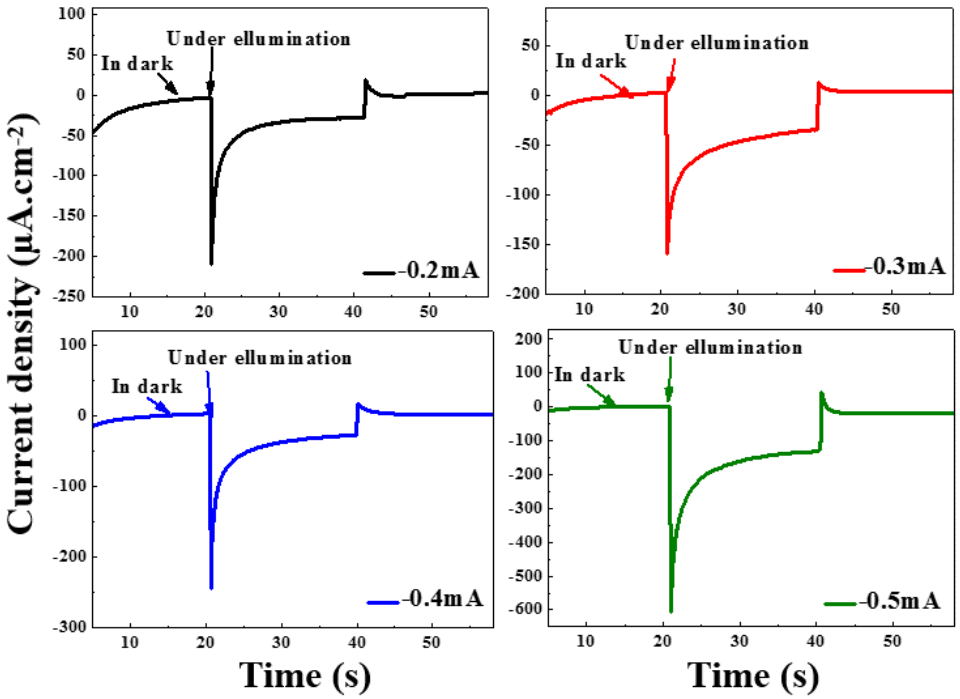

Figure 4.3: Photocurrent measured from of Cu_2O thin films at different current densities: $-0.2, -0.3, -0.4$ and $-0.5mA.cm^{-2}$.

4.2.1.4 Electrochemical impedance spectroscopy (EIS) analysis

Electrochemical impedance spectroscopy (EIS) for the Cu_2O nanostructures at different current densities: $-0.2, -0.3, -0.4$ and $-0.5mA.cm^{-2}$ was carried out in three electrode

cells in $0.5M$ of Na_2SO_4, at an open-circuit potential of $10mV vs SCE$, within the frequency range of 10^5 to $0.5 \times 10^{\check{}}1Hz$. Fig. (4.3) shows Nyquist diagrams (Z imaginary versus Z real) that analyze the charge transfer process in the interface electrolyte/electrode for the synthesized Cu_2O nanostructures.

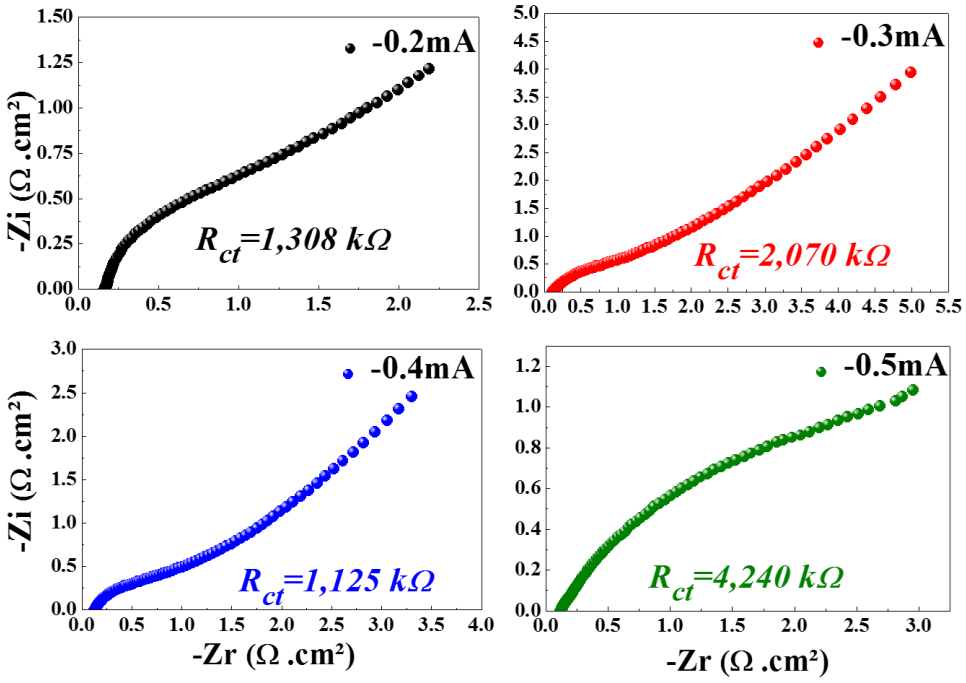

Figure 4.4: Nyquist plots (Z imaginary versus Z real) measured in $0.5M$ of Na_2SO_4 of Cu_2O thin films at different current densities: $-0.2, -0.3, -0.4$ and $-0.5\ mA.cm^{-2}$.

As a first look, the plots flow an identical shape, which is a large semi-circle, in a high frequency region accompanied by a straight line with approximately 45° in the low-frequency region. The semi-circle diameter in the high frequencies indicates the charge transfer resistance (R_{ct}), which can be obtained by fitting the Nyquist plots. The corresponding values are mentioned in the diagrams. It seems clear that the lowest charge transfer resistance (R_{ct}) is 1.125 KΩ for the elaborated Cu_2O under $-0.4mA.cm^{-2}$ correspond to the shortest semicircle diameter, which means that the Cu_2O in this condition possesses the highest charge transfer mobility [146, 147]. It is worth noting that the charge transfer efficiency is proportional to the photoresponse and the acceptor charge density for the grew Cu_2O films from -0.2 to $-0.4mA.cm^{-2}$. However, a high charge transfer

resistance (R_{ct}) is observed under $-0.5mA.cm^{-2}$ that may be due to the instability of the sample. Furthermore, the linear part of the different diagrams indicates a mass transfer limited process in the low-frequency region[148].

Table 4.2: Current density effect ($-0.2, -0.3, -0.4$ and $-0.5\ mA.cm^{-2}$) on the electrical properties of Cu_2O nanostructures.

Sample	$\mathbf{E_{fb}}$**(mV/ECS)**	$\mathbf{N_A}(cm^{-2})$	**W(nm)**	**Max photoresponse** (μ**A.cm**$^{-2}$)	$R_{ct}(K\Omega)$
-0.2mA	586	1.12×10^{19}	6.663	-210	1.305
-0.3mA	-563	0.61×10^{19}	3.994	-160	2.070
-0.4mA	-563	1.34×10^{19}	2.974	-242	1.125
-0.5mA	-563	1.84×10^{19}	3.224	-606	4.240

4.2.2 Structural characterization

Fig. (4.5)(a) shows XRD patterns that investigate the structural properties of the obtained Cu_2O films on FTO substrates. The different Cu_2O nanostructures were electrodeposited over a current density range from -0.2 to $-0.5mA.cm^{-2}$. Fortunately, no additional peaks or impurities were seen, only corresponding peaks to the Cu_2O were observed, according to (JCPDS no. 00-005-0667). It seems clear that the applied current density has a strong effect on the crystallographic orientation. This is in agreement with the other works [130, 140], which mentioned that the texturation is closely related to the current density. For $I = -0.2mA$, (200) was observed as preferential orientation. However, it transforms to (111) when the current density a little bit decreases. Theoretically, in the growth principle, the fastest kinetics is responsible for growing grains parallel to the surface, whereas the slow kinetics is responsible for the growth of the exposed faces [149]. Therefore, the relative growth rate determines the final shape of the crystal and controls

its structural properties. The crystallographic orientation is important for the transport and mobility of the charge carrier density. On the other hand, the photocatalytic activity is determined by the exposed film facets [140], As well it is responsible for controlling the final morphology. According to Fig. (4.5)(a), the (200) peak is proportional to the estimated acceptor density. The texture factor of the films was calculated through the following equation [138], summarized in Tab. (4.3).

$$f = \frac{\frac{I^{(111)}}{I^{(200)}} - \frac{I_0^{(111)}}{I_0^{(200)}}}{\frac{I^{(111)}}{I^{(200)}} + \frac{I_0^{(111)}}{I_0^{(200)}}} \tag{4.6}$$

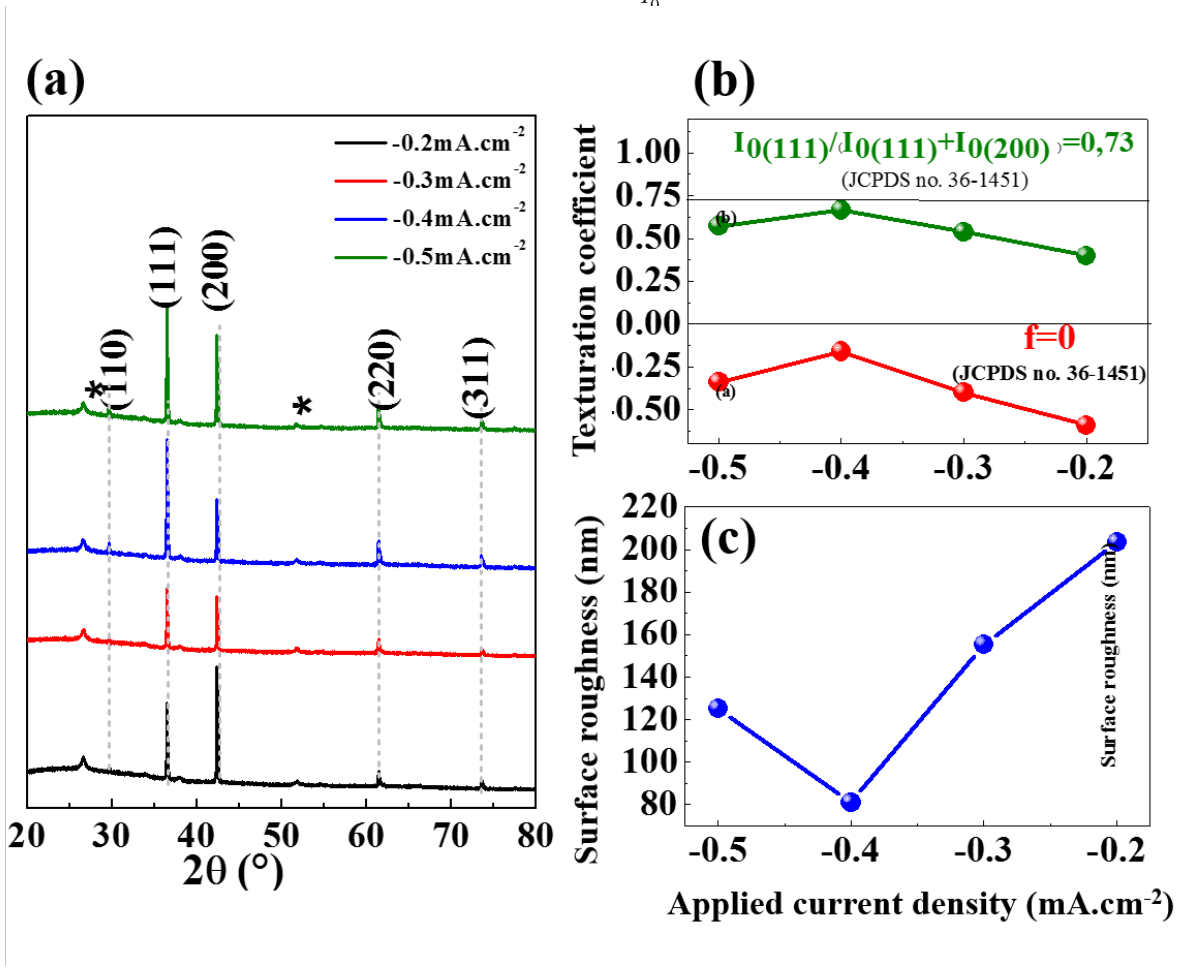

Figure 4.5: a) XRD patterns of Cu_2O thin films at different current densities: -0.2, -0.3, -0.4 and $-0.5 mA.cm^{-2}$ on FTO. b) Texture coefficients ($I_{(111)}/I_{(200)}$) and $I_{(111)}/(I_{(111)} + I_{(200)})$) as a function of the applied current density. (111) and (200) are the main diffraction peaks from the deposited Cu_2O nanostructures. c) The roughness as function on the applied current density.

Fig. (4.5)(b) shows the f factor values and the ratio between the (111) intensity and the sum of the (111) and (200) intensities, as a function of the applied current density. The black lines show the corresponding factors obtained from (JCPDS no. 00-005-0667) for a polycrystalline Cu_2O. So, the goal is to find preferential orientation along the 111

Table 4.3: Current density effect ($-0.2, -0.3, -0.4$ and $-0.5 mA.cm^{-2}$) on the structural properties of Cu_2O nanostructures.

Sample	**Surface roughness(nm)**	**Texturation coefficient**		
		f [(111)/(200)]	$\frac{\mathbf{I_{(111)}}}{\mathbf{I_{(111)}+I_{(200)}}}$	$\frac{\mathbf{I_{(111)}}}{\mathbf{I_{(200)}}}$
-0.2mA	203.485	-0.59	0.40	0.6811
-0.3mA	155.22	-0.4	0.5381	1.1652
-0.4mA	81.067	-0.16	0.6667	2.0005
-0.5mA	125.10	-0.34	0.5728	1.3410

is the highest possible when the grains are cubes with {100} exposed faces. (111) was the preferential found orientation for all the deposited Cu_2O films under current density from $-0.3\ mA.cm^{-2}$ to $-0.5\ mA.cm^{-2}$. It can be seen that, under $-0.4 mA.cm^{-2}$, the film gives the desired crystallographic orientation. However, it does not exceed the black line. This texturation variation is attributed to the competition between (200) and (111) orientations during the deposition reaction of Cu_2O, as a function of the applied current density. This result could explain the variation in the carrier charge density analyzed by the Mott-Schottcky measurements, and the photoresponse obtained by the photocurrent measurements. Besides, the films roughness has been measured and presented in Fig. (4.5)(c). It can be seen that it is inversely proportional to the texturation factors in Fig. (4.5)(b). The higher is the (111) orientation, the lower is the film roughness. As long as, the structural properties control the final morphology, it can control also the film surface roughness.

4.2.3 Optical characterization

Using a UV-visible spectrophotometer, the optical measurements of the elaborated Cu_2O films under different current densities were carried out at ambient temperature. The spectral of which extends over is from 200 to 1100 nm. Fig. (4.6)(a) shows the different spectra of the optical transmittance of the samples. As a general look, whatever the applied current density, the different samples follow an identical shape.

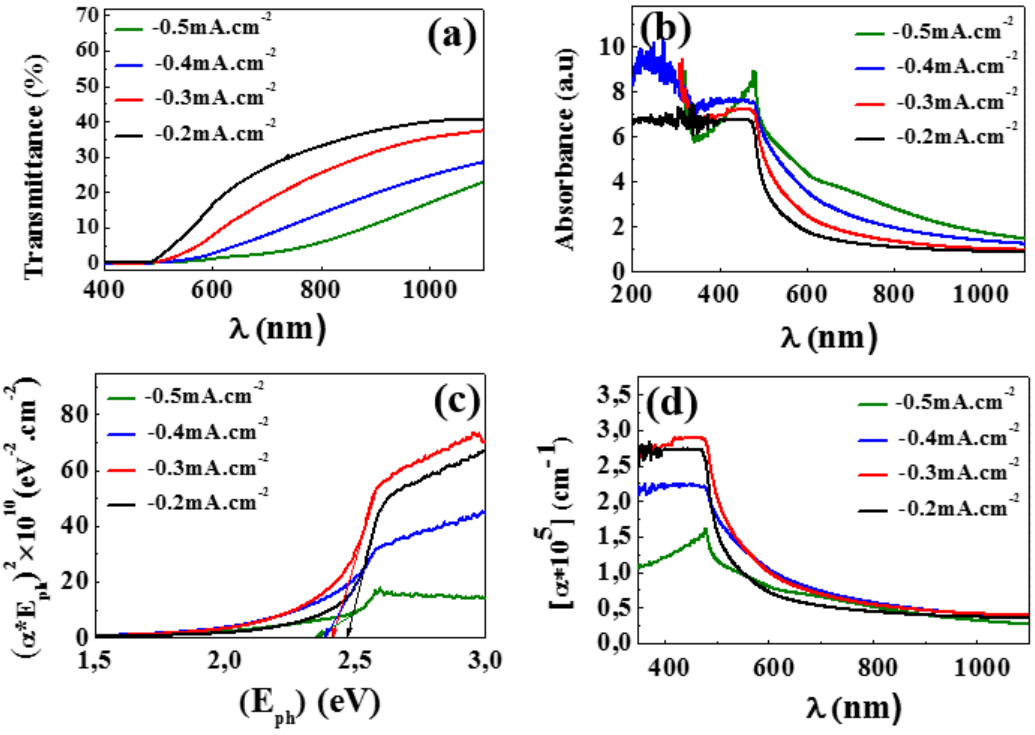

Figure 4.6: a) Transmittance spectra of Cu_2O nanostructures at different current densities: $-0.2, -0.3, -0.4$ and $-0.5 mA.cm^{-2}$. b) Absorbance spectra of the different Cu_2O nanostructures. c) Dependence of $(\alpha h\nu)^2$ versus photon energy (E_{ph}) (eV) for Cu_2O thin films. d) The corresponding absorption coefficient.

It can be seen that the light is totally absorbed (0% transmittance) in the UV range likewise in the left side of the visible spectrum, as a function of the wavelength, regardless of the applied current density. It seems clear that the transmittance begins to increase softly, from the cyan-green range due to the direct and narrow band-gap of Cu_2O films[150]. It is worthnoting that the light starts to be transmitted when its energy is less

or equal to the band gap energy (by increasing the wavelength). On the other hand, when the incident energy becomes less than the band gap energy of Cu_2O semi-conductors, the absorbance becomes weak, driving to an increasing transmittance proportional to the wavelength (see Fig. (4.6)(b)). From Fig. (4.6)(a), the transmittance still increasing over the visible range and continues steady with a weak increase until the near infrared towards a maximum percentage; $40.5, 37.67, 28.38$ and 23.2% respectively for $-0.2, -0.3, -0.4$ and $0.5\ mA.cm^{-2}$. It can be seen that the current density has a big effect on the optical parameters of the film. In addition, when the current varies from -0.2 to $-0.5 mA.cm^{-2}$ the film thickness increases according to Tab. (4.4), which is in agreement with Eq. (4.4). However, the transmittance decreases while the current density decreases to more negative values regardless of the incident photon energy. From Fig. (4.6)(b), the absorbance achieves its maximal value when the photon energy is higher than the gap energy ($\lambda < \lambda_g$). At $\lambda = \lambda_g$ the absorbance achieves its limited value after a plateau, and it is preparing to decrease. Finally, when photon energy becomes less than the gap energy ($\lambda > \lambda_g$), sudden decay is observed stilling decreases until the Infrared spectrum, where the curves for the different samples become closer. It is worthnoting that the absorbance increases when the current density increases (in absolute value) over the entire measuring range. The absorption coefficient was calculated from Beer-Lambert's low (Eq. (2.4)). During the measurement, the incident field was perpendicular to the film surface means the reflectance was null. The absorption coefficient is shown in Fig. (4.6)(d). It's evident that the transmittance of the different Cu_2O films does not exceed 40%, for the most transparent sample elaborated under $-0.2 mA.cm^{-2}$, which is back to the best absorbance of the samples confirmed by the high absorption coefficient. Tab. (4.4) summarize all the obtained optical parameters, through UV.Vis spectrophotometery measurements, investigating the effect of the current density on the optical band gap energy. The $(\alpha h\nu)^2$ versus the photon energy $(h\nu)$ were plotted for the different current densities in Fig. (4.4)(c) using Tauc relation Eq. (2.5) [110], determining the optical band gap for the deposits. From Tab. (4.4), the band gap energies are: $2.46, 2.4, 2.38$ and 2.34 for $-0.2, -0.3, -0.4$ and$-0.5 mA.cm^{-2}$, respectively. It can be seen that the band gap energy decreases when the applied current density decreases to more negative values. This result notes that the band gap energy

can be narrowed by increasing the rate of growth. The light penetration depth, which is defined by the inverse absorption coefficient, is calculated for $\lambda = \lambda_g$. It can be seen that the values are proportional to the photoresponse, which explains the variation in the photocurrent measurements as a function of the applied current density. The higher is the light penetration, the better is the excitation, more effective is the interaction with light.

Table 4.4: Current density effect ($-0.2, -0.3, -0.4$ and $-0.5 mA.cm^{-2}$) on the optical properties of of Cu_2O nanostructures.

Sample	**Band gap Energy(eV)**	**Band gap Wavelength λ_g(nm)**	**Transmittance at λ_g**	**Film thickness d(nm)**	**Absorption parameters at λ_g**		
					$\alpha \times 10^5$ (cm^{-1})	**Absorbance**	**light penetration depth (nm)**
-0.2mA	2.46	504.06	2.33%	247.65	1.52	3.75	65.7
-0.3mA	2.40	516.66	1.19%	249.69	1.77	4.43	56.4
-0.4mA	2.38	521	0.46%	342.24	1.56	5.37	66.1
-0.5mA	2.34	529.91	0.33%	549.48	1.03	5.7	97

4.2.4 Photoelectrochemical (PEC) stability of Cu_2O nanostuctures for water splitting

The photoelectrochemical (PEC) stability of the Cu_2O thin films at different current densities; -0.2, -0.3, -0.4 and $-0.5 mA.cm^{-2}$, were evaluated for 20 minute in a distilled water at a constant potential of a $-0.5V$ under a chopped light for 20 *sec* on and 20 *sec* off. The PEC performance curves are shown in Fig. (4.7). It can be seen that the cathodic photocurrent is constant as time increases for the elaborated samples under -0.2

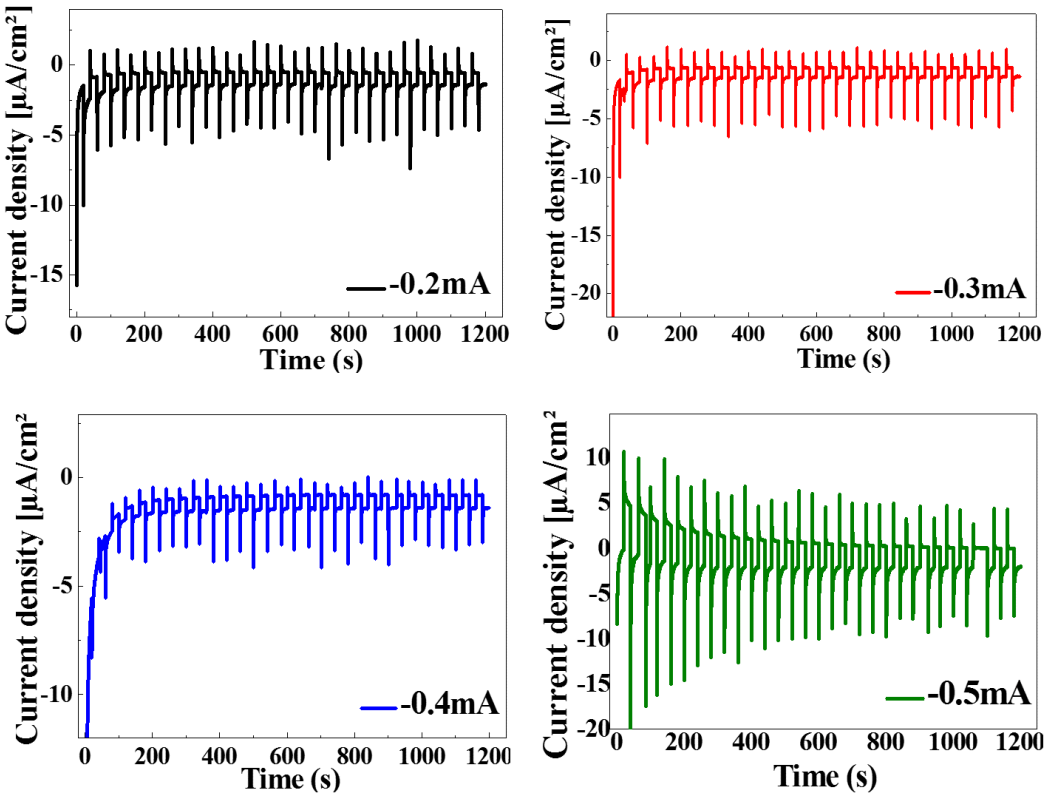

Figure 4.7: Photoelectrochemical (PEC) water splitting measurements of Cu_2O nanostructures at different current densities (-0.2, -0.3, -0.4 and -0.5 $mA.cm^{-2}$), in distilled water, applied potential is $-0,5$ V/SCE for 20 minutes.

to $-0.4mA.cm^{-2}$. This indicates that the Cu_2O nanostructures are stable. However, for $-0.5mA.cm^{-2}$, the generated photocurrent decreases as a function of time. As well as, the PEC stability of the Cu_2O nanostructures can be evaluated quantitatively using the following relation[151]:

$$R_{ph} = J_{ph}^{final} \Big/ J_{ph}^{initial} \tag{4.7}$$

Where $J_{ph}^{initial}$ and J_{ph}^{final} are the average photocurrent at the initial stage (100 sec) of the illumination and the average photocurrent densities at the final stage (100 sec) of the illumination, respectively, where the results were collected in Tab. (4.5). It seems clear that the stability of the samples is in good agreement with the electrochemical impedance spectroscopy. The higher is the charge transfer mobility, the higher is the photoelectrochemical stability. It is worth noting that a high PEC performance is achieved, for

Table 4.5: Current density effect ($-0.2, -0.3, -0.4$ and $-0.5 mA.cm^{-2}$) on the Photoelectrochemical (PEC) stability of Cu_2O nanostructures for water splitting application.

Sample	-0.2mA	-0.3mA	-0.4mA	-0.5mA
$J_{ph}^{initial}$	-5.75	-7.13	-3.47	-17.46
J_{ph}^{final}	-4.53	-4.85	-3.11	-9.67
R_{ph}	78.78%	68.02%	89.62%	55.38%

the different samples, and it does not drop below 55.38% in the worst conditions (at $-0.5 mA.cm^{-2}$). On the other hand, it exceed 89.62% at $-0.4 mA.cm^{-2}$. These results are very significant either for photocatalytic or photovoltaic applications.

4.3 Galvanostatic, and potentiostatic electrodeposition of Cu_2O nanostructures: comparative study in two different pH

In order to investigate the mode effect, in different pH media, on the properties of Cu_2O nanostructures, two baths containing a $0.05M$ copper sulfate ($CuSO_4$), $0.06M$ citric acid, and a $NaOH$ adjusting the pH at11 and 12. When, the deposition temperature held constant at 70 °C for $15 minute$. Under potentiostatic mode, constant potential of $-0.6V/ESC$ will be applied, and constant current density of $-0.4 mA.cm^{-2}$ will be applied through galvanostatic mode

4.3.1 Electrochemical study

4.3.1.1 Cyclic voltammetry

Fig. (4.8) shows cyclic voltammetry recorded in two different pH, 11 and 12. The voltamograms show the same appearance.

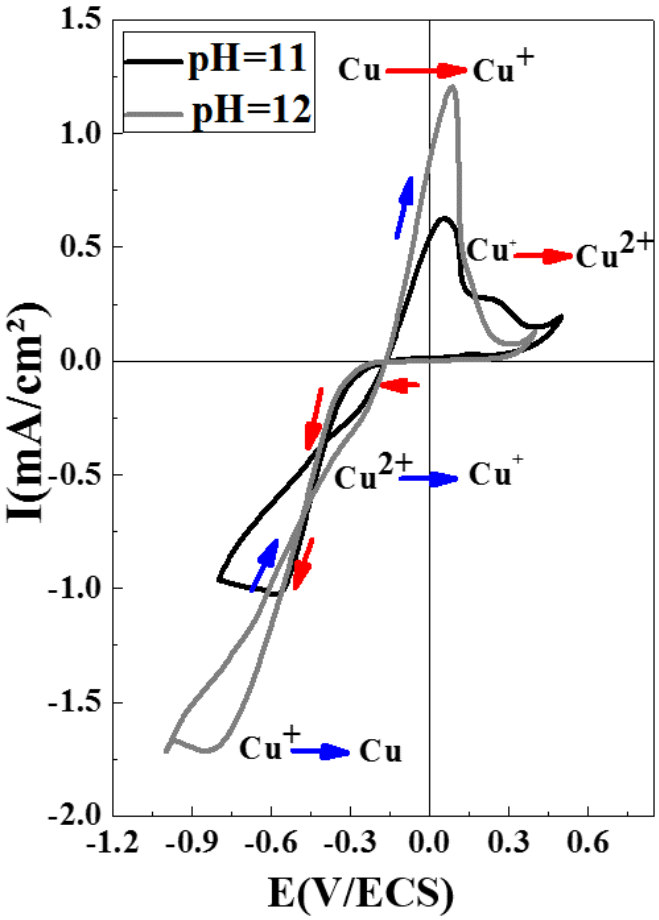

Figure 4.8: Cyclic voltammograms recorded in 0.05M of $CuSO_4$ at 70 °C, in pH of 11 and 12.

In the cathodic sweep from 0.5 V to -1.0 V, two reduction peas have been observed. The first peak observed at -0.25 V for both curves. Which is correspond to the reduction of Cu^{2+} ions present in the solution to Cu^{+} ionsCu^{+2} to Cu^{+}[149] , followed by possibility of formation of Cu_2O[152] between -0.18 V and -0.57 V in pH of 11. However, the peak is larger for pH=12 followed by the formation of Cu_2O between $-0.18V$ and -0.7 V. The second peak, at 0.6 V in pH 11 and $0.8V$ in pH 12, is associated with the reduction of Cu^{+} ions to metallic copper (Cu). Evenly, two peaks were noted in the anodic sweep, the first one indicate the oxidation of copper previously formed to Cu^{+} ions at 0.5 V and 0.82 V for pH of 11 and 12 respectively. the second indicate Cu^{+} to Cu^{2+} oxidation at 0.25 V corresponding to pH 11 and at 0.18 V in pH 12. Comparing the two voltamograms, it can

be seen that when the electrolyte became more basic, this can induce significant shift in the peaks position and diameter. Furthermore, the current density recorded on the FTO surface shows decrease in more basic electrolyte (pH=12). To better understand, when $-0.4V$ was applied the current density decreases from $-0.35\ mA.cm^{-2}$ to $-0.5\ mA.cm^{-2}$. Which can be explain by the easier and faster formation of Cu_2O in pH 12. Besides, faster is the formation, thicker is the film, better is optical absorption of Cu_2O. However, electrochemical, structural, optical and morphological study is necessary to evaluate the pH effect in Cu_2O features.

In each electrolyte two samples were developed successively, in galavanostatic mode and potentiostatic mode. They will be spelled out in the rest of the thesis: $Cu_2O^{(11)}_{(p)}$, $Cu_2O^{(11)}_{(g)}$, $Cu_2O^{(12)}_{(p)}$, and $Cu_2O^{(12)}_{(g)}$, respectively for Cu_2O nanostructures elaborated; in pH=11 under potentiostatic mode, in pH=11 under galvanostatic mode, in pH=12 under potentiostatic mode, and film formed in pH=12 under galvanostatic mode.

4.3.1.2 Mott-Schottky measurements

Fig. (4.9) shows Mott-Schottky plots of different Cu_2O films, in order to have an idea about the mode effect and the pH value on the electrical properties. It seems clear that the slope of the linear part of the capacitance curves is negative for the different samples confirming the p-type semiconductors known from earlier for Cu_2O. From the slope of the line, the accepter carrier density N_A can be estimate thanks to Eq. (2.2)[102]. See Tab (4.5), for $Cu_2O^{(11)}_{(p)}$ the carrier density is $4.32 \times 10^{16} cm^{-3}$, which decreases to $0.89 \times 10^{16} cm^{-3}$ since the mode transformed to galvanostatic ($Cu_2O^{(11)}_{(g)}$). In addition, it decreases to $1.62 \times 10^{16} cm^{-3}$ when the pH increases saving the same mode. Furthermore, the calculated carrier density, for the Cu_2O nanostructures, are about $10^{16} cm^{-3}$, which are in agreement with the values for electrodeposited Cu_2O films ($10^{14} - 10^{18}\ cm^{-3}$) [153–156]. However, in $Cu_2O^{(12)}_{(g)}$ case, the estimated acceptor density is very high compared to other results, but it is in good accord with values published by Nakaoka [157]. Theoretically, the carrier density is proportional to the number of defects in the crystal grating of the oxide, such as copper vacancies (Cu_V) and/ or interstitial oxygen (O_i) [158, 159]. It seems

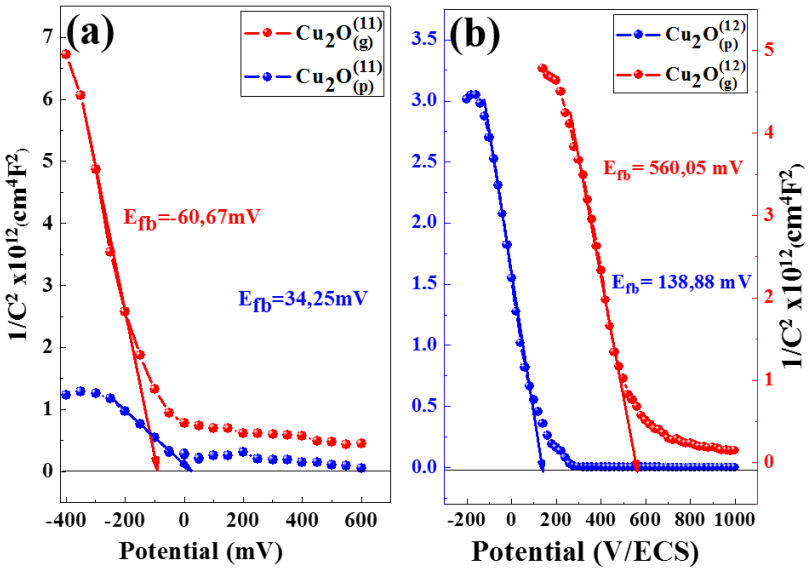

Sample	N_A (cm^{-3})
$Cu_2O^{(11)}_{(p)}$	4.32×10^{16}
$Cu_2O^{(11)}_{(g)}$	0.89×10^{16}
$Cu_2O^{(12)}_{(p)}$	1.62×10^{16}
$Cu_2O^{(12)}_{(g)}$	1.34×10^{19}

Figure 4.9: Mott–Schottky plots for Cu_2O thin films elaborated under potentiostatic, and gavanistatic modes a) bath pH=11, b) bath pH=12. The corresponding flat band potential values are indicated for the different samples.

clear that, all samples elaborated under constant current density in the previous study of this work in electrodeposition bath pH of 12 had higher donor concentration. This could be due to the faster deposition rate of Cu_2O or it can be due to the orientation of cristals, because the number of acceptors is estimated just in the depletion zone and not in all the crystallographic network of the semiconductor.

4.3.1.3 Photocurrent analysis

Photocurrent-Time measurements were measured for different conditions in order to determine the photoresponse, and to confirm Mott-shottcky analyses. Fig. (4.10) shows Photoresponse=f(t) for Cu_2O films recorded under chopped light in $0.5M$ Na_2SO_4 and $0Vvs.SCE$ as an applied potential.

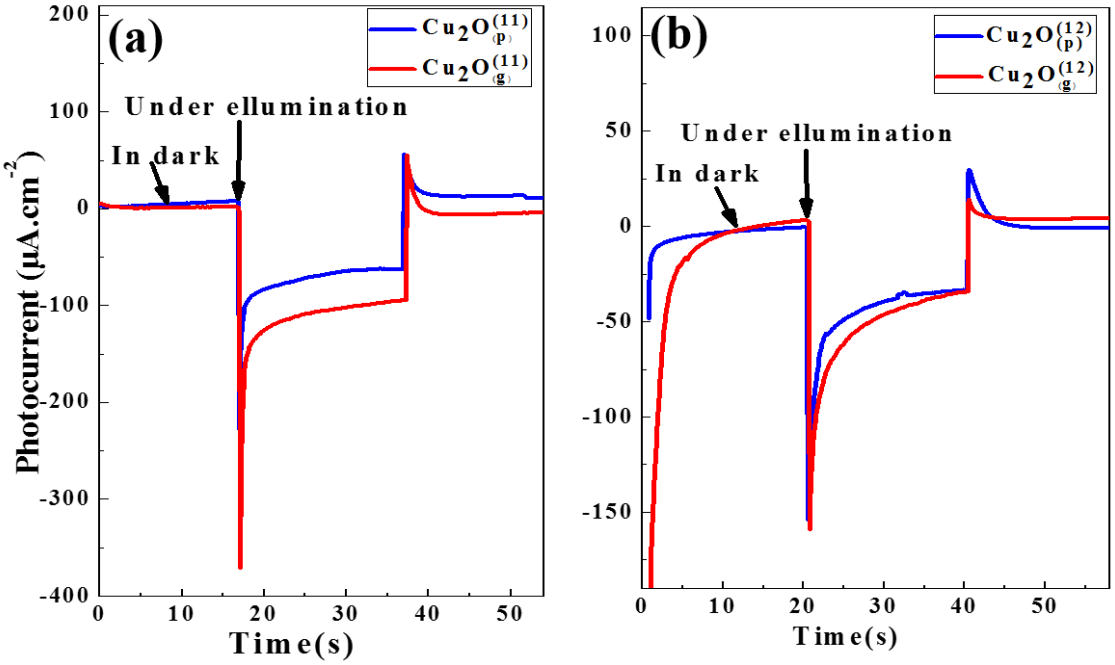

Figure 4.10: Photocurrent measurements of Cu_2O thin films grow under potentiostatic, and gavanistatic modes. a) bath pH=11, b) bath pH=12.

It seems clear, for both medium regardless is the mode of elaboration, constant current very close to $0A$ was observed in dark. However, cathodic photocurrent have been noted under white light as rectangular responses for all samples. As Known, the cathodic photorespense determine the p-type behavior semiconductors. That confirms Mott-Schottky results. When the pH medium is about 11 (see Fig. (4.10)(a)), the maximal photocurrent generated since the film received light was $-215\ \mu A.cm^{-2}$ and $-371.2\ \mu A.cm^{-2}$ for $Cu_2O^{(11)}_{(p)}$, and $Cu_2O^{(11)}_{(g)}$ respectively. Through Mott-schottky measurement, the estimated acceptor density was higher using potentiostatic mode, that is note in accord with the photoresponse. Which, maybe due to more roughness at the potentiostatic film surface caused scattering phenomena affected the photons-electron interaction. In the other hand, in more basic electrolyte (Fig. (4.10)(a)), both curves are relatively superposed. Under illumination, the maximal photocurrent generated was $-153.3\mu A.cm^{-2}$ and $-159.11\ \mu A.cm^{-2}$ corresponding to $Cu_2O^{(12)}_{(p)}$, and $Cu_2O^{(12)}_{(g)}$ respectively. Practically, no mode effect is observed in this case. A. Paracchino et al.[140] reported that the crystallographic orientation is relevant to influence the transport of currier density and the photon-material

interaction. Direct relation is between the exposed facets and the photo-catalytic activity of the films. To better understand, structural study is necessary.

4.3.2 Structural characterization

The crystallographic orientation is the mean important feature to control the film morphology and optical properties. Film performance is determined by the films exposed facets[140]. XRD pattern are shown in Fig. (4.11)(a) for Cu_2O films developed under galvonostatic approach and potontiostatic approach in pH path of 11and 12. Back to (JCPDS no. 00-005-0667), only peaks corresponding to Cu_2O were observed for different conditions. Fortunately, (111) orientation when the oriented grains are cubes with the 100 faces is preferential one for all of samples. However, effect on the crystallographic orientation is remarkable, which is controlled by the relative growth rate. Further, it is important for the transport and mobility and the final performance of film. Fig. (4.11)(b) shows the ratio between (111) and (200) intensities, and Fig. (4.11)(c) shows the ratio between (111) intensity and the sum of (111) and (200) intensities. The horizontal bleu lines show the theoretical values obtained from (JCPDS no. 00-005-0667) for a polycrystalline Cu_2O. It seems clear, that the film orientation on (111) is better using potentiostatic mode, i.e; from Tab (4.6) $\frac{I_{(111)}}{I_{(111)}+I_{(200)}}$ is: 0.8291 and 0.7869 for $Cu_2O^{(11)}_{(p)}$, and $Cu_2O^{(11)}_{(g)}$. And it is 0.8086 and 0.6667 for $Cu_2O^{(12)}_{(p)}$, and $Cu_2O^{(12)}_{(g)}$ respectively. For both texturation factors (see Fig. (4.11)(b) and Fig. (4.11)(c)), all values are above the theoretical bar except for $Cu_2O^{(12)}_{(g)}$, which show the enhancement of the crystallographic grating of Cu_2O films. It is important as well to noted that the texturation coefficient following (111) orientation is higher from samples elaborate in less basic electrolyte under the same mode; $\frac{I_{(111)}}{I_{(200)}}$ is: 4.8521 and 4.2259 for $Cu_2O^{(11)}_{(p)}$, and $Cu_2O^{(12)}_{(p)}$, and it is 3.6943 and 2.0005 for $Cu_2O^{(11)}_{(g)}$) , and $Cu_2O^{(12)}_{(g)}$ respectively, According to Tab. (4.6).

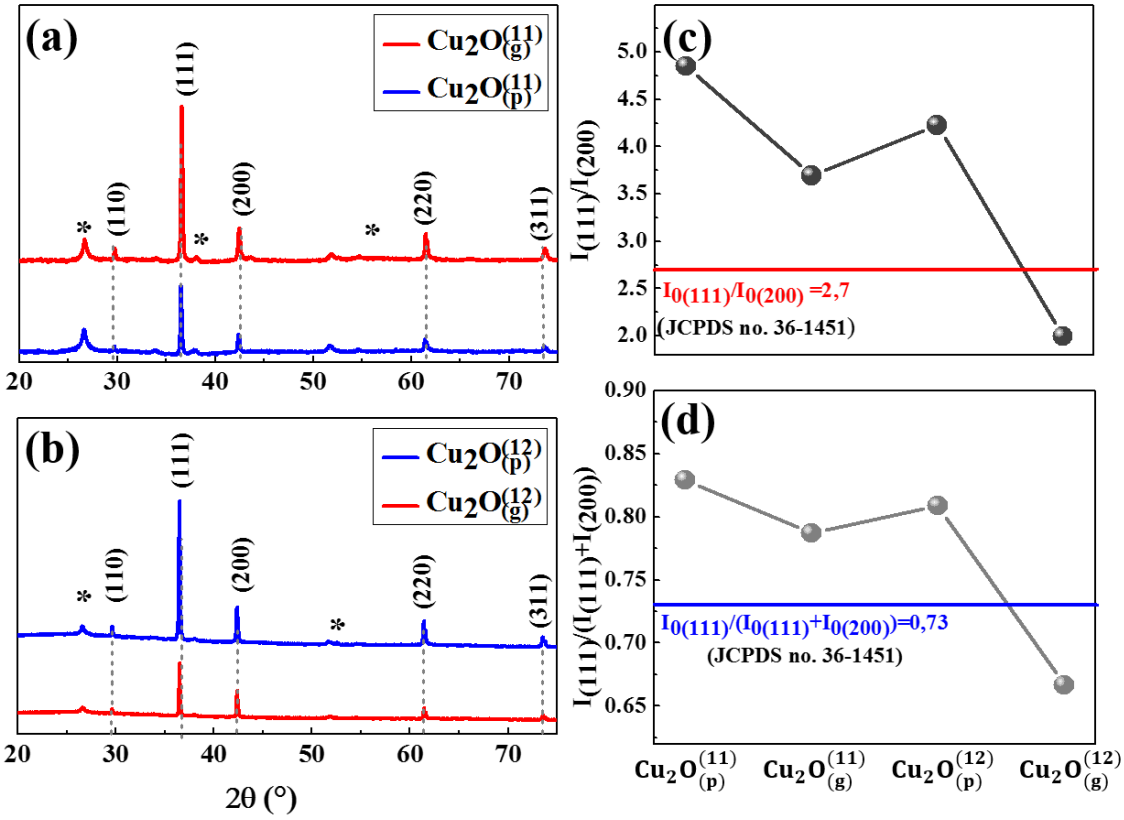

Figure 4.11: *XRD* patterns of Cu_2O thin films elaborate under potentiostatic, and gavanistatic modes (a pH 11, b) pH 12. (*) Indicate diffraction peaks corresponding to the *FTO* substrates. The corresponding texture coefficients: c) $(I_{(111)}/I_{(200)})$. d) $I_{(111)}/(I_{(111)} + I_{(200)})$. (111) and (200) are the main diffraction peaks from the Cu_2O films. The line in the graph shows the intensities ratio according to the (JCPDS no. 00-005-0667).

Table 4.6: Mode effect on the structural properties of Cu_2O nonostructures.

Sample	$Cu_2O^{(11)}_{(p)}$	$Cu_2O^{(12)}_{(g)}$	$Cu_2O^{(11)}_{(p)}$	$Cu_2O^{(12)}_{(g)}$
$\frac{I_{(111)}}{I_{(111)}+I_{(200)}}$	0.8291	0.7869	0.8086	0.6667
$\frac{I_{(111)}}{I_{(200)}}$	4.8521	3.6943	4.2259	2.0005

It seems clear that, the crystallographic orientation is followed the 100 plan for different

samples, but, for $Cu_2O^{(12)}_{(p)}$ the ratio is below the JCPDS value. This may explains the deviated value of the acceptor density, which is directly related to the orientation of the crystals that makes up the semiconductor network.

4.3.3 Optical characterization

Absorption coefficients for different conditions were shown in Fig. (4.12), which extends over is from 200 to 1100nm spectral.

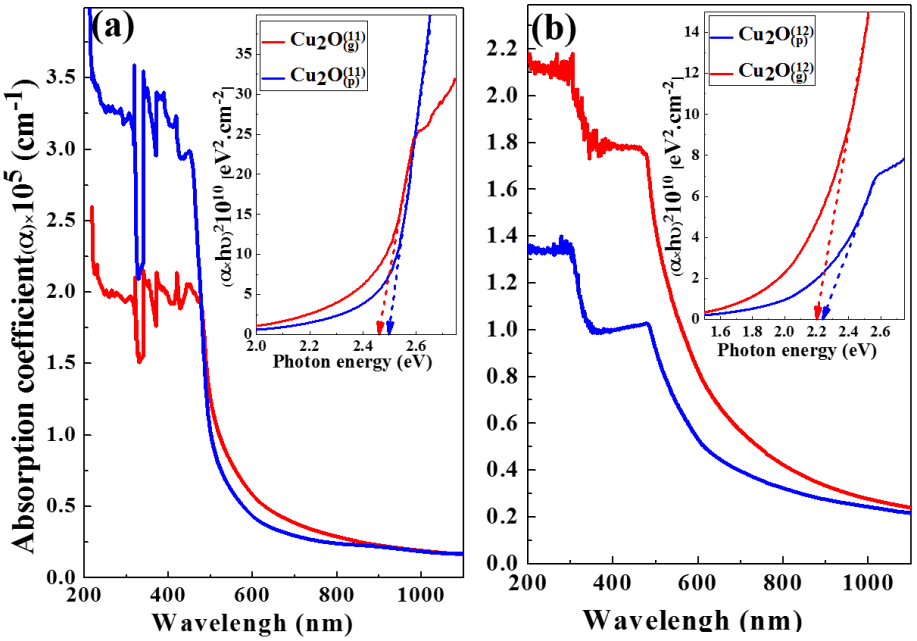

Figure 4.12: Absorption coefficient spectra of Cu_2O thin films elaborate under potentiostatic, and gavanistatic modes. a) bath pH=11. Inset. The corresponding dependence of $(\alpha h\nu)^2$ versus photon energy (eV). b) bath $pH = 12$. Inset. The corresponding dependence of $(\alpha h\nu)^2$ versus photon energy (eV).

It seems clear that in both baths, absorption coefficients for films elaborated under constant applied potential ($Cu_2O^{(11)}_{(p)}$, and $Cu_2O^{(12)}_{(p)}$) is lower compared to the galvanostatic one ($Cu_2O^{(11)}_{(g)}$, and $Cu_2O^{(12)}_{(g)}$) in the visible and near IR. It is important to note that the absorption coefficient started to decrease softly when the energy of the incident photo became lower than the band gap energy (with wavelength increasing). Briefly, in

Table 4.7: Mode effect on the optical properties of Cu_2O nonostructures

Sample	**Band gap Energy(eV)**	**Band gap Wavelength $\lambda_g(nm)$**	**Film thickness d(nm)**	**Absorption parameters at λ_g**		
				$\alpha \times 10^5$ (cm^{-1})	**Absorbance**	**light penetration depth (nm)**
$\mathbf{Cu_2O^{(11)}_{(p)}}$	2.49	498	348.8	0.59	2.06	169.49
$\mathbf{Cu_2O^{(11)}_{(g)}}$	2.45	506.12	583.9	0.77	4.6	129.87
$\mathbf{Cu_2O^{(12)}_{(p)}}$	2.23	556.05	551.10	0.68	3.72	147.05
$\mathbf{Cu_2O^{(12)}_{(g)}}$	2.19	566.21	354.42	1.05	3.72	95.29

Tab. (4.7) the absorbance and the light penetration depth were calculated through Beer-Lambert low Eq. (2.4) for 550nm as the medal of the Cu_2O optical band gap which is as well the medal of the visible range. It can be seen, that the light penetration depth decreases from 169.49 to 129.87nm for $Cu_2O^{(11)}_{(p)}$, and $Cu_2O^{(11)}_{(g)}$ and from 147.05 to 95.29nm for $Cu_2O^{(12)}_{(p)}$, and $Cu_2O^{(12)}_{(g)}$. Which can be back to the texturation ratio between (111) and (200) orientations, which can be introduce scattering phenomenon at the surface.
Insert Fig. (4.12) shows the $(\alpha h\nu)^2$versus the photon energy ($h\nu$) were plots for the different samples, using Tauc relation Eq. (2.5) [110], determining the optical band gap for the deposits. The band gap energy and the corresponding band gap wavelengths are summarized in Tab. (4.7) as well. The band gap energy decreases when the mode transformed from potentio to glavano. The band gap energy decreases with the bath pH increases regardless is the mode used during the Cu_2O film formation.

4.3.4 Morphological characterization

Fig. (4.13) shows the topography from the 2D AFM images insert roughness values. It can be seen that the film surface looks homogeneous with relatively small size for films

elaborate in path pH of 11. However, the grains became bigger in pH=12. Further, it can be noted that films have grown under potentiostatic mode; $Cu_2O^{(11)}_{(p)}$, and $Cu_2O^{(12)}_{(p)}$ are more uniform. The surface roughness decreases from 30.85 to 24.40nm, however, it increases twice from 45.48 to 81.06nm when the elaboration mode transform from potentiostatic mode to glvanostatic mode in pH 11 and 12 respectively.

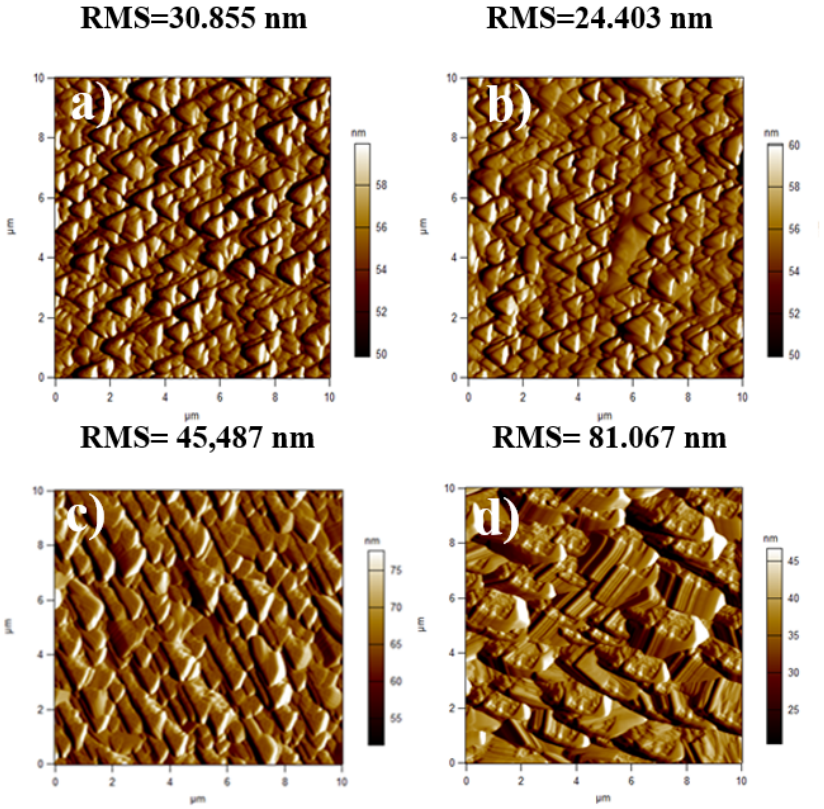

Figure 4.13: Tapping mode 2D AFM images ($10 \times 10 \mu m^2$) of Cu_2O thin films. a) $Cu_2O^{(11)}_{(p)}$ b) $Cu_2O^{(11)}_{(g)}$ c) $Cu_2O^{(12)}_{(p)}$ d)$Cu_2O^{(12)}_{(g)}$.

In the other hand, look at Tab. (4.7), in pH 11 $Cu_2O^{(11)}_{(g)}$ is thicker than $Cu_2O^{(11)}_{(p)}$, and $Cu_2O^{(12)}_{(p)}$, is thicker than $Cu_2O^{(12)}_{(g)}$, in pH 12. It can be seen that the thickness is invers proportional to the surface roughness. When, the thickness increases, it gives the holes a chance to fill up, which is in accord with another study [114], where the roughness increases when the diameter of the Cu_2O nanocube decreases. However, this hypothesis can be valid only to Cu_2O, because, for rGO the roughness increases with thickness increasing [63]. Fig. (4.14) shows the SEM images of $Cu_2O^{(11)}_{(p)}$, $Cu_2O^{(11)}_{(g)}$, $Cu_2O^{(12)}_{(p)}$, and

$Cu_2O^{(12)}_{(g)}$.

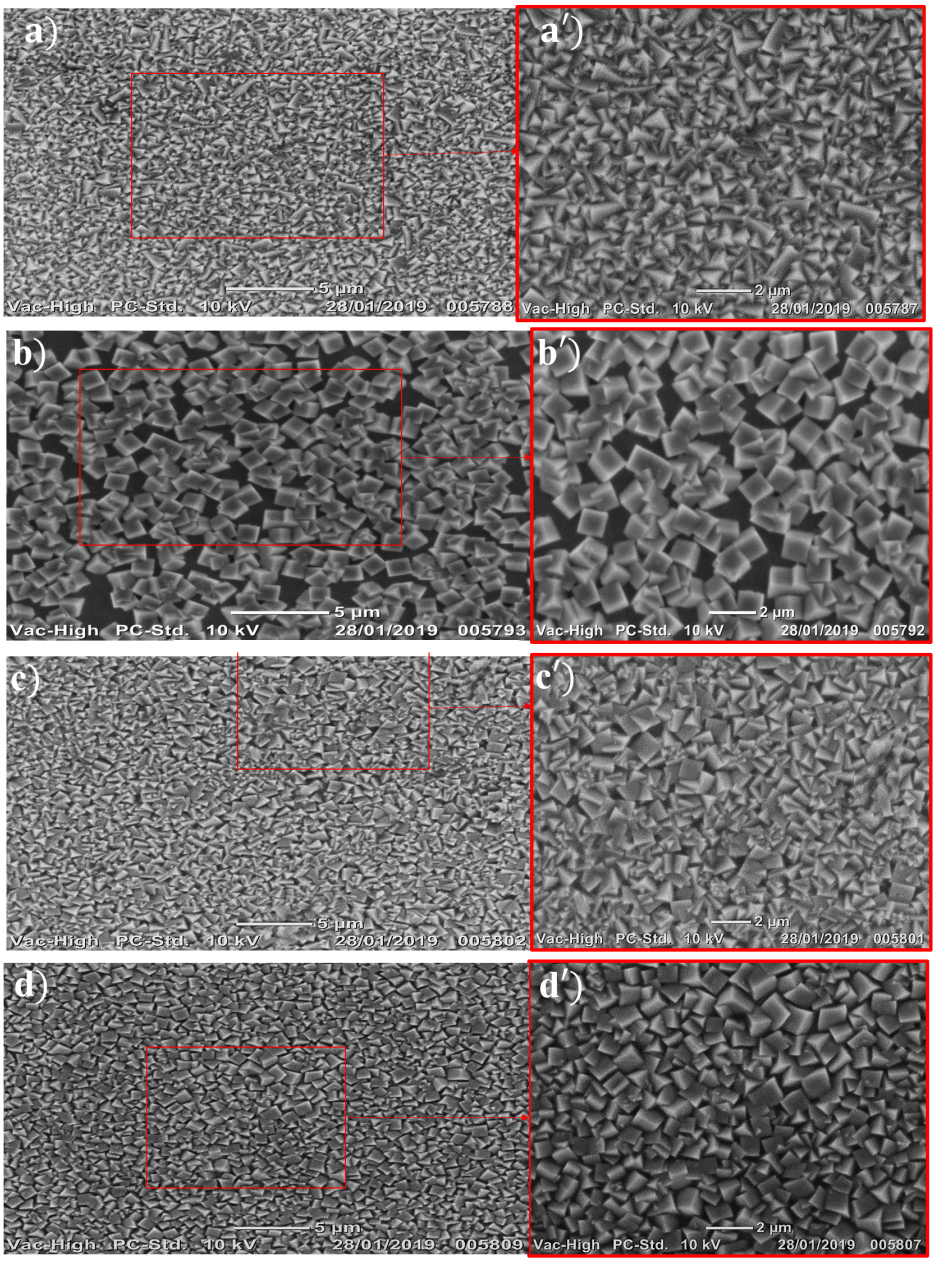

Figure 4.14: SEM images of of Cu_2O thin films. a) $Cu_2O^{(11)}_{(p)}$ b) $Cu_2O^{(11)}_{(g)}$ c) $Cu_2O^{(12)}_{(p)}$ d)$Cu_2O^{(12)}_{(g)}$

As a general look, typical cubic Cu_2O is obtained under the different conditions of elaboration. However, they are not oriented in the same way. In pH bath of 11, homogeneous pyramidal morphology is observed using potentiostatic approach, means cubs were

growing following the {100} plan, which confirms the high crystallographic orientation following (111). Saving the mode of elaboration in more alkaline solution, practically same cub orientation was obtained. In both baths, under galvanostatic approach the grains quantity is lower, which is can be explain by the lower rate of growth compared to the potentiostatic one. Besides, the cubs are exposed into {100}, and {111} plans, which can be explain by the competition in reaction between the (111) and (200) crystallographic orientation. In the other hand, homogeneous grain in size are achieved under galvanostatic mode compered to whose obtained using the potentiostatic one. Furthermore, increasing the bath pH from 11 to 12 the grain size increased, when constant potential, and constant current density where applied respectively.

4.4 Conclusion

In summary, in the previous chapter, we have shown that the performance of Cu_2O nanostructures can be optimized by controlling the electrodeposition parameters. The applied current density can control directly the structural orientation, which influence the film morphology and the charge carrier mobility. In our conditions, $-0.4\mu A.cm^{-2}$ was the optimal current density. In the other hand, the mode of elaboration can introduce a remarkable effect on the film features. Crystallographic orientation is better using the potenstiostatic mode. However, the absorption coefficient is higher under galvanostatic mode. With increasing bath pH, the roughness, and the absorption coefficient increase. Despite the band gap energy and the orientation perpendicular to {100} decrease. It is very important to note, there is a compromise when you study, the electrodeposition parameter effect on final film features. Because, it is related to the application. e.i when the Cu_2O film is prepared for photovoltaic application, the orientation fllowing (111) is important and the optical properties (high absorption coefficient) are important as well. However, when the film is oriented to phocatalytic, the structural properties have not significant influence as long as the optical performance are very high.

Chapter 5

Additives effect on the Cu_2O nanostructures properties

5.1 Introduction

TAILORING the interfacial arrangement of atoms plays an important role in enhancing the desired reactivity or stability of a material [160]. For which, morphological control of crystals became an opportunity for scientists these days. It is well known that the performances of Cu_2O semiconductor nanostructures depend on a set of parameters such as the composition, crystallization, size, and morphology [161–163]. In particular, the surface morphology determines the physical, structural, and chemical properties of nanoparticles[164] and the performance of Cu_2O nanostructures as well[140]. Thus, a great number of efforts was focusing on synthesis shape-controlled Cu_2O nanocrystals such as nano-cubes [165], hollow spheres [166], nanocage , nanoframes [167], and polyhedrals[168]. Up to date, the cause of the Cu_2O conduction type is not completely clear and still the subject of intense debate. Theoretical calculation predicting the presence of anti-site defects of Cu and O at well-defined pH. Where, under strong acidic solutions the Cu atom substitutes an O atom, causing$n-$type Cu_2O semiconductor[169]. W. Wang et al (2010)[158] demonstrated experimentally that $n-$type Cu_2O can be intrinsically deposited (without doping) in acidic solution. Which is in agreement with the theoretical results. On the other hand, ab–initio calculations suggest that the presence of copper vacancies introduces an acceptor level at $0.3eV$ above valence band (Ev) which causes the formation of $p-$type Cu_2O [159]. Experimentally, $p-$type conduction was ob-

tained at alkaline solutions; from cupric sulfate solution at $pH7-12$ [156, 170]. Besides the pH adjustment, Cu_2O conductivity type can be tuned by adding chlorine ions in the electrodeposition bath. Thus, enormous work has studied the chlorine effect on the conduction type[171, 172]. At acidic pH values, the Cl^- ions present in the electrolyte occupy an O atom position to introduce a donor level acting as an n-type dopant to Cu_2O film[173]. However, the presence of Cl^- ions has no effect on the Cu_2O carrier density at high pH values. This view is supported by Lincot et al (2012) who reported that regardless of the Cl^- ions concentration in the solution, the conduction type of Cu_2O remains $p-$type, as long as the pH is in its highest values [171]. Therefore, the effect of $Cl-$ ions on Cu_2O structural, morphological, optical, and electrical properties requires a series of investigations. On the other hand, changing the direction and growth rate of the crystals lead to different final morphologies[174], which can be obtained by synthesizing Cu_2O in a growth medium containing additives that have the power to adsorb preferentially on specific crystallographic planes[175, 176]. M.J. Siegfried and K.S.Choi[177] were used many additives to control the stability and the morphology of Cu_2O nanocrystals such as NH_4NO_3 , or $(NH_4)_2SO_4$. In this work, two additives have been chosen to controlCu_2O properties, and to study their effect on the morphological, structural, and electrochemical properties ofCu_2O nanostructure. Ammonium chloride (NH_4Cl) will be used as additive to control Cu_2O nanoparticles. Besides, potassium chloride (KCl) will be used to control Cu_2O nanostructures. For both studies, galvanostatic electrochemical deposition had been chosen to elaborate a nanostructured Cu_2O, as the rate of the deposition can be precisely controlled using this method[23]. To our knowledge, the effect of NH_4Cl on the structure and shape of Cu_2O nanoparticles had never been reported. As well as, we investigate the effect of chlorine on structural, morphological, and optical properties of Cu_2O nanostructures, using different concentrations of KCl under galvanostatic approach. Furthermore, we will illustrate the importance of synthesized Cu_2O nanoparticles for photoelectrochemical applications.

5.2 Ammonium chloride effect on Cu_2O nanoparticles properties, galvanostaticlly electrodeposited

The Cu_2O nanoparticles were prepared from a $0.003M$ of copper nitrate ($Cu(NO_3)2$) with a $0.1M$ of potassium chloride (KCl). To study the additive effect on the features of the Cu_2O nanoparticles, a $0.0015M$ of ammonium chloride (NH_4Cl) was added to the electrolyte. After a current effect study, the current density was kept at $-0.3mA.cm^{-2}$ as an optimum value for 2 hours.

5.2.1 Cyclic voltammetry

In this study, the Cu_2O nanoparticles were electrodeposited in a chlorine medium. We investigate the effect of the additive (NH_4Cl) on the electrochemical process of the Cu_2O formation using a Cyclic Voltammetry. Fig. (5.1) shows a voltammogram FTO substrate immersed in a Cu_2O deposition bath without the additive and in the presence of the NH_4Cl. The two voltammograms show the same appearance; In the cathodic sweep from $1.0V$ to $-1.0V$, the reduction peak observed at $\breve{}0.05V$ corresponds to the reduction of the Cu^{2+} ions present in the solution to Cu^{+} ions, followed by the formation of Cu_2O between $-0.03V$ and $-0.23V$. The second peak at $-0.42V$ is associated with the reduction of the Cu^{+} ions to metallic copper (Cu). In the anodic sweep, two peaks were noted, the first indicates the oxidation of the copper that previously formed to the Cu^{+} ions at $0.055V$ while the second indicates Cu^{+} to Cu^{2+} oxidation at $0.3V$. Comparing the two curves, it can be seen that the presence of the NH_4Cl induces a significant shift in the peaks position. The reduction of Cu^{2+} to Cu^{+} shifted from $\breve{}0.03V$ in the absence of the NH_4Cl to $-0.14V$ in the presence of the NH_4Cl. Furthermore, the current density on the FTO surface show decrease in the presence of the NH_4Cl. For example at an applied potential of $-0.18V$ the current density on the voltammogram slightly decreases from $0.152mA.cm^{-2}$ (which corresponds to the absence of the NH_4Cl) to $0.775mA.cm^{-2}$ in the presence of NH_4Cl, which mean that the formation of the Cu_2O is easier and faster in the absence of the additive. This was confirmed from SEM images where the Cu_2O nanoparticles were covering FTO surface in the absence of the additive Fig. (5.2)-(a) and

poorly formed in the presence of the NH_4Cl Fig. (5.2)-(e).

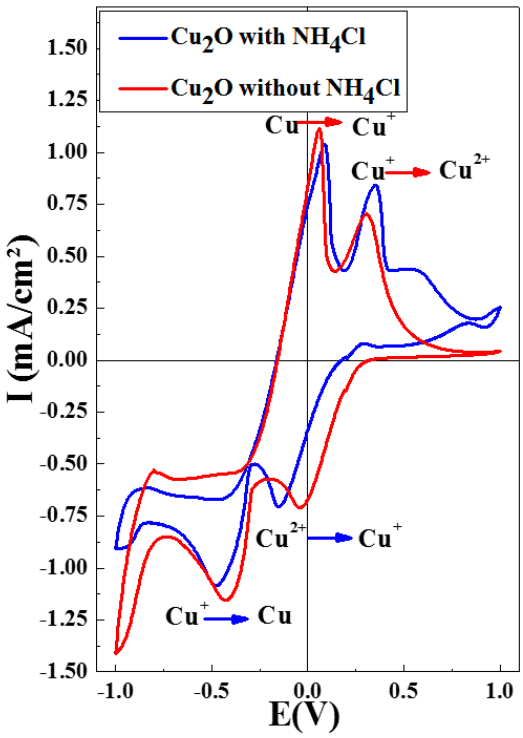

Figure 5.1: Cyclic voltammogram recorded in $0.003M$ of $Cu(NO_3)_2$ and $0.1M$ of KCl at 70 °C, and in the same conditions with addition of $0.0015M$ Of NH_4Cl. Potential scan rate is $100mV/s$.

5.2.2 Morphological characterization

Detailed analysis for the Cu_2O nanoparticles morphology was performed by the field emission scanning electron microscopy (SEM). Fig. (5.2) shows SEM images of Cu_2O deposited in the presence and in the absence of the ammonium chloride.

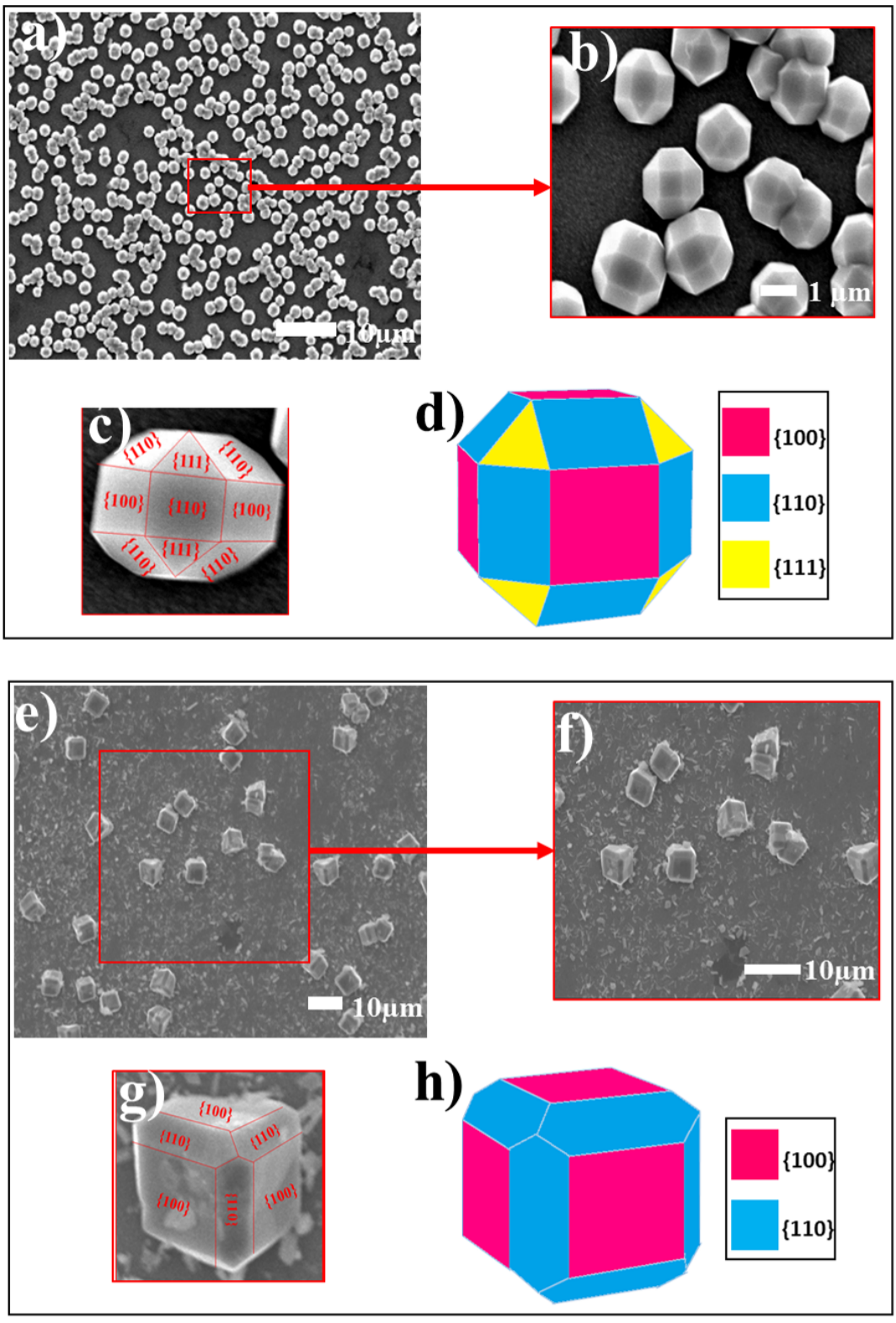

Figure 5.2: SEM images of the Cu_2O particles. a, b, c, d) without NH_4Cl. e, f, g, h) with $0.0015M$ NH_4Cl.

It is clear that the amount and the morphology of Cu_2O were greatly affected by the presence of the NH_4Cl. Small particles of Cu_2O were deposited all over the FTO surface in the absence of the additive Fig. (5.2)-(a,b), whereas in the presence of the NH_4Cl, few particles of Cu_2O were scattered over the surface of FTO Fig. (5.2)-(e,f). It can be seen from SEM images of Cu_2O individual grain Fig. (5.2)-(c,g) that the Cu_2O nanoparticles have uniform morphology with two different types of polyhedral. 26-facet polyhedral, with a particle size of $1.73m$, was observed in the absence of the NH_4Cl Fig. (5.2)-(c). While, 18-facet polyhedral, with three times larger particle size ($4.85m$), was formed in the presence of the additive Fig. (5.2)-(g). For a clear illustration of crystallographic plans, simulated 3D structures of Cu_2O crystals are shown in Fig. (5.2)-(d,h). The 26-facet polyhedral formed in the absence of the additive has, 12 rectangular faces, 8 triangular faces, and 6 square faces, correspond on {110}, {111} and {100} crystallographic plans respectively. On the other hand, 18-polyhedral formed in the presence of the NH_4Cl, 12 hexagular {100} faces, and 6 square {110} faces.

5.2.3 Structural characterization

The XRD analyses of the Cu_2O nanoparticles are shown in Fig. (5.3)(a). The deposited Cu_2O in the absence of the NH_4Cl is orientated following (200), (220) and (111) of polycrystalline cubic phase were indexed (JCPDS no. 00-005-0667). It's worthnoting that the peaks at 43.31° and the one at 50.53° were indexed to metallic copper (111) orientation (JCPDS card, No°. $85-1326$). This is in agreement with the SEM images, the Cu_2O particles grew in polyhedral shape with different facets corresponding to {110}, {100} and {111} crystallographic plans on which are perpendicular on the XRD (220), (111) and (200) orientations, respectively. On the other hand, the presence of the NH_4Cl, in the Cu_2O deposition bath, changes totally the composition and the orientation of the Cu_2O nanoparticles. It shows a single peak indexed as (110) orientation (monocrystal) following the cubic phase of cuprous oxide (JCPDS no. 00-005-0667). No other peaks of impurities, like cupric oxide (CuO) or metallic copper (Cu), are detected, which indicates the high purity of these particles.

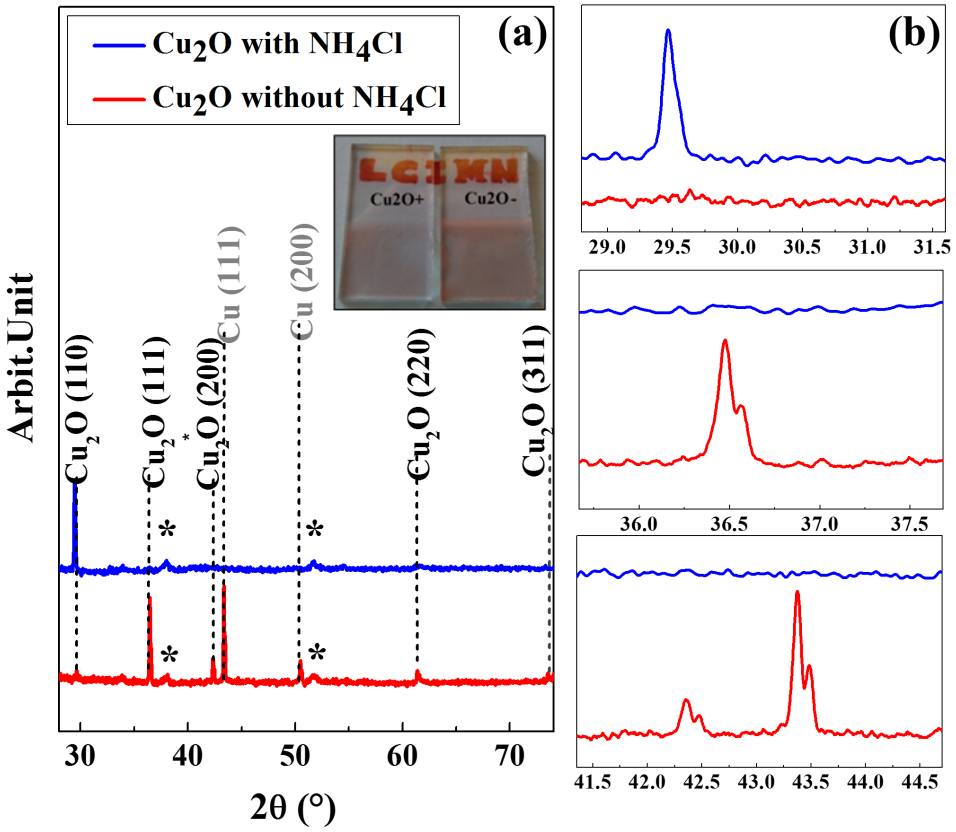

Figure 5.3: a) XRD pattern of Cu_2O nanoparticles electrodeposited on FTO substrate with and without NH_4Cl. (*) Indicate diffraction peaks corresponding to the FTO substrate.b) Zoom of XRD spectra of obtained films at different diffraction peak regions

Inset Fig. (5.3)(a) shows the real samples, it seems clear that the film formed in a bath free of NH_4Cl is darker, which is in agreement with SEM images. That shows that the crystals are more compact.Fig. (5.3)(b) presents a zoom of XRD spectra at different diffraction peak regions, that confirm the radical change of the structural orientation by adding a small amount of NH_4Cl.

5.2.4 Photocurrent analysis

Photoelectrochemical characterization allowed us to have information about the Cu_2O nanoparticles conduction type and evaluate the electrochemical behavior of the Cu_2O in the dark and its photo-activity under the illumination. Fig. (5.4) shows the photo-response

curves of the Cu_2O particles recorded in a 0.5 M of Na_2SO_4 solution under a chopped illumination for 20sec on and 20sec off. As can be seen, under the irradiation, the two samples Fig. (5.4)(a,b) present an abrupt decrease in the current density. This cathodic current (current negative relative to the dark current) confirms a p-type conductivity to Cu_2O. The Cu_2O particles formed in the absence of the additive reveal higher photocurrent response (16.25 $\mu A.cm^{-2}$) than the Cu_2O particles deposited in the presence of the NH_4Cl (3.2 $\mu A.cm^{-2}$). This can be explained by the presence of the metallic copper in the formed Cu_2O in the absence of the additive[151]. As the $p-$type Cu_2O under the illumination generate electrons as a minor carrier, the photogenerated electrons move to the $Cu_2O/$ electrolyte interface to reduce H^+ ions present in the solution. The presence of the metallic copper atoms facilitated the transport of the photogenerated electrons to the interface, which improves the photoresponse.

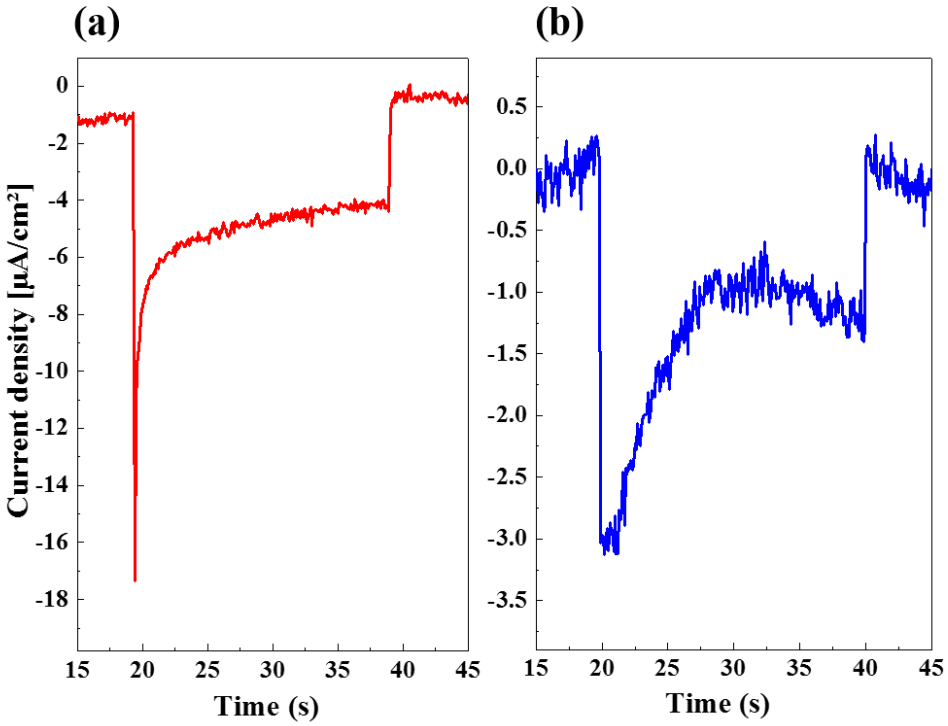

Figure 5.4: a) Photocurrent measured from Cu_2O nanoparticules. For the measurement, the applied potential is $0V/SCE$. The solution contains 0.5 M Na_2SO_4. The sample was illuminated with a 500 W white-light source. b) with $0.0015MNH_4Cl$.

5.2.5 The photoelectrochemical (PEC) stability of Cu_2O 26−facet polyhedral particles

The photoelectrochemical (PEC) stability of Cu_2O 26−facet polyhedral particles, formed in the absence of the additive, was evaluated for 20 minute at a constant potential of $-0.5V$ under chopped light with 20 *sec* on and 20 *sec* off. The PEC performance curve is presented in Fig. (5.5).

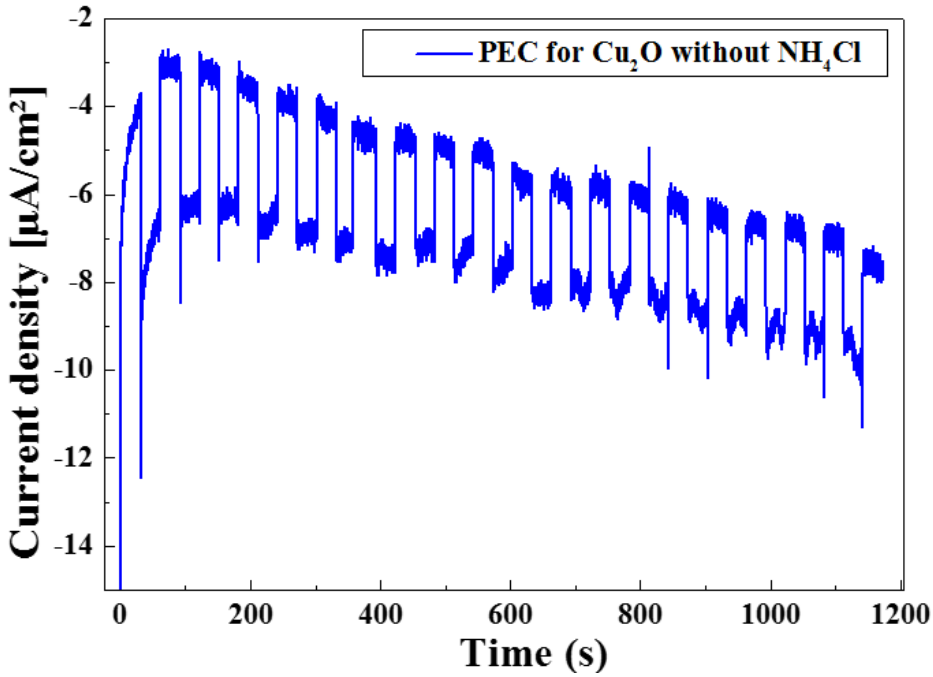

Figure 5.5: Photoelectrochemical (PEC) water splitting measurements, applied potential is $-0,5V/SCE$ in distillate water.

The cathodic photocurrent didn't change as the time was increased. This indicates that the Cu_2O particles are stable. The PEC stability of Cu_2O particles can be evaluated by Eq. (5.1) relation[151]:

$$R_{ph} = J_{ph}^{final} \Big/ J_{ph}^{initial} \tag{5.1}$$

Where $J_{ph}^{initial}$ is the average photocurrent at the initial stage (100 *sec*) of illumination and J_{ph}^{final} is the average photocurrent densities at the final stage (100 *sec*) of illumination. As the photocurrent densities at the end of the PEC measurements (−3.00) slightly smaller than the initial photocurrent densities (−4.08), high PEC performance of 73.5%

was achieved. These results were very significant for photovoltaic and photocatalytic applications.

5.3 Potassium chloride effect on Cu_2O nanoparticles properties, galvanostaticlly electrodeposited

The Cu_2O nanostructures were grown in a deposition bath contains a $0.05M$ of copper sulfate ($CuSO_4$), a $0.05M$ of citric acid, and a $NaOH$ to adjust the pH at 11. In order to investigate the chloride effect on the structural, morphological, and optical properties of the Cu_2O nanostructures, two concentrations of potassium chloride KCl ($0.001M$ and $0.1M$) were added, where one of them was 100 times concentrated. The elaboration was for 30 minutes.

5.3.1 Morphological characterization

The SEM images of the deposited Cu_2O films in the absence and the presence of different concentrations of Cl^- ions are shown in Fig. (5.6). It seems clear that the morphology of the Cu_2O nanostructures is strongly dependent on the presence of the Cl^- ions. The surface of the deposited Cu_2O sample in a bath free of chloride ions Fig. (5.6)(a) is entirely covered by very compact grains of cubic shapes, where the average grain size was around $700nm$. Small flakes of $20nm$ were evenly distributed over the surface Cu_2O cube faces. EDX analysis (not shown) confirms the purity of the Cu_2O. Fig. (5.6)(b) shows the surface of the deposited Cu_2O film in the presence of a $0.001M$ of chlorine ions. It is clear that the substrate surface was partially covered by smaller Cu_2O cubic grain ($550nm$) of sharper edges, and cubic Cu_2O faces free of flakes. However, by increasing the chloride concentration to $0.1M$ Fig. (5.6)(c), the morphology is completely changed. The substrate surface was entirely covered by an inhomogeneous film of Cu_2O. Along the deposit, crystals of polyhedral shape and relatively small size were growing. Around each group of crystals (contained two or three crystals) leaves are formed, where it is clear that from one part of an already existing group another one was developed.

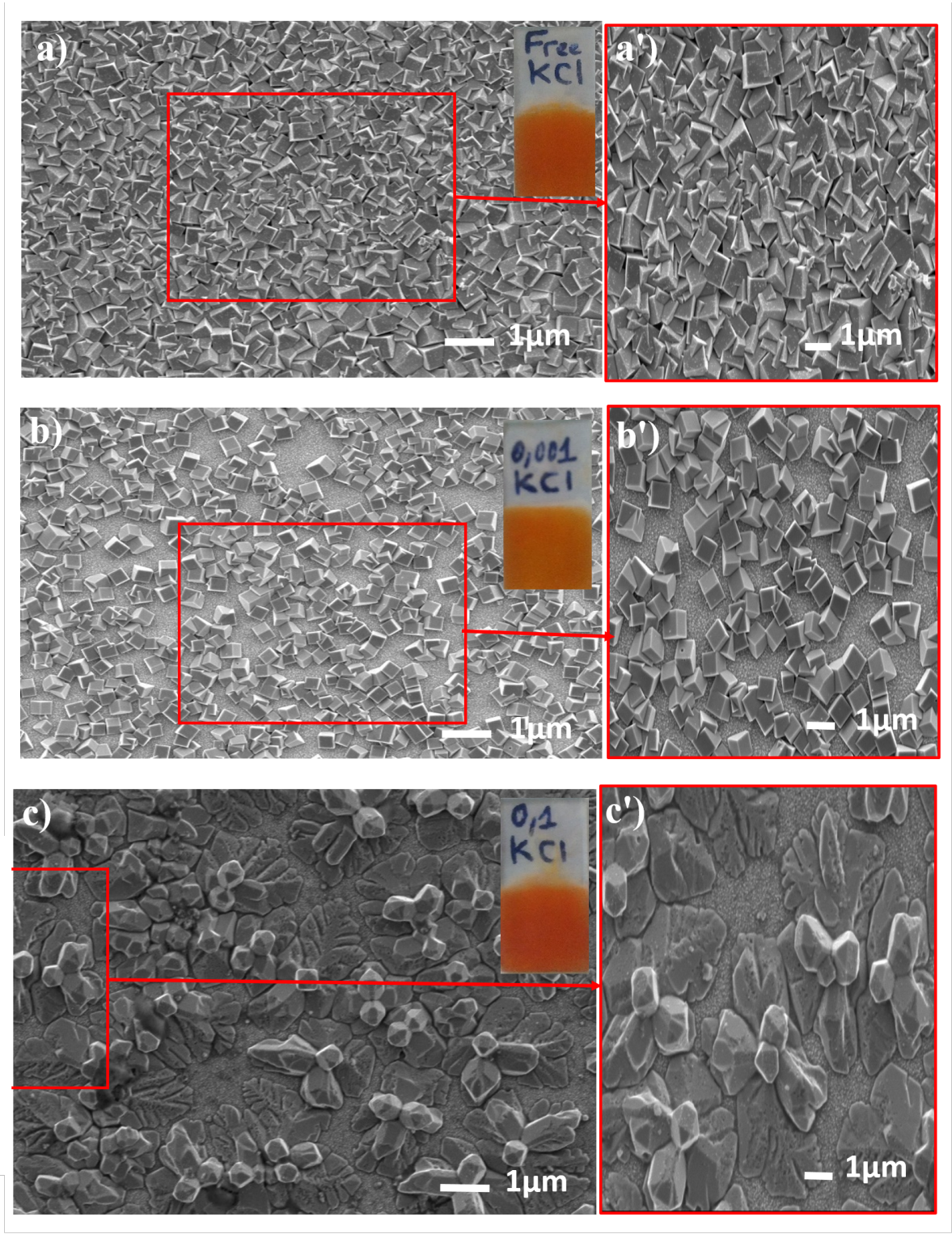

Figure 5.6: SEM images of the Cu_2O nanostructures (a) without KCl (b) 0.001M KCl (c) 0.1M KCl. In the corner of each image, a higher magnification of the respective nanostructures is shown.

Also, steams are formed in the region that divides two groups, this is exactly what we call "dendritic branching growth". Whereby, the branches on the substrate grow faster than those emerging from the substrate due to the fact that the FTO substrate is much more conductive than the Cu_2O crystals. From these observations; we can say that the chlorine ions follow an additive behavior in controlling Cu_2O morphology. They have made Cu_2O grows as dendrites, where the lateral growth is much faster than the vertical growth. K.Choi[178] has identified that the growth along the (100) direction can be hindered in the presence of the chlorine ions. Dendritic branching growth can achieve high surface areas with excellent charge transport properties due to good electrical continuity. To better understand these properties, a structural analysis and photocurrent measurements are necessary.

5.3.2 Structural characterization

To identify the structural properties of the Cu_2O nanostructures deposited in different chloride concentrations, the X-ray diffraction (XRD) were carried out as shown in Fig. (5.7) (a). The identification of the XRD spectra peaks confirms the formation of the polycrystalline Cu_2O nanostructures, crystallized following the cubic phase according to (JCPDS no. 00-005-0667) with (111) orientation as the most intense peak. The noted peaks at 29.46°, 42.27°, 61.33°, and 73.59° were indexed to (110), (200), (220) and (311), respectively. No additional peak, corresponding to any impurities such as Cu, $Cu(OH)_2$ or CuO, has been observed. Comparing the XRD spectra, all the samples show a (111) preferential orientation. An increase in the (111) orientation intensity with increasing Cl^- concentration was also observed, which may be due to the increase of the deposited Cu_2O amount. It is important to note that the peaks position shift to higher values with increasing Cl^- concentration from $0.001M$ to $0.1M$ indicating the incorporation of the Cl^- ions in the Cu_2O lattice. The texturation factor of films was calculated through the following equation Eq. (5.2) [138], and summarized in Tab. (5.1).

$$f = \frac{\left(I^{(111)}/I^{(200)}\right) - \left(I_0^{(111)}/I_0^{(200)}\right)}{\left(I^{(111)}/I^{(200)}\right) + \left(I_0^{(111)}/I_0^{(200)}\right)} \tag{5.2}$$

Fig. (5.7)(b) shows the f factor values and the ratio between (111) and (200) intensities, as a function of the chloride concentrations.

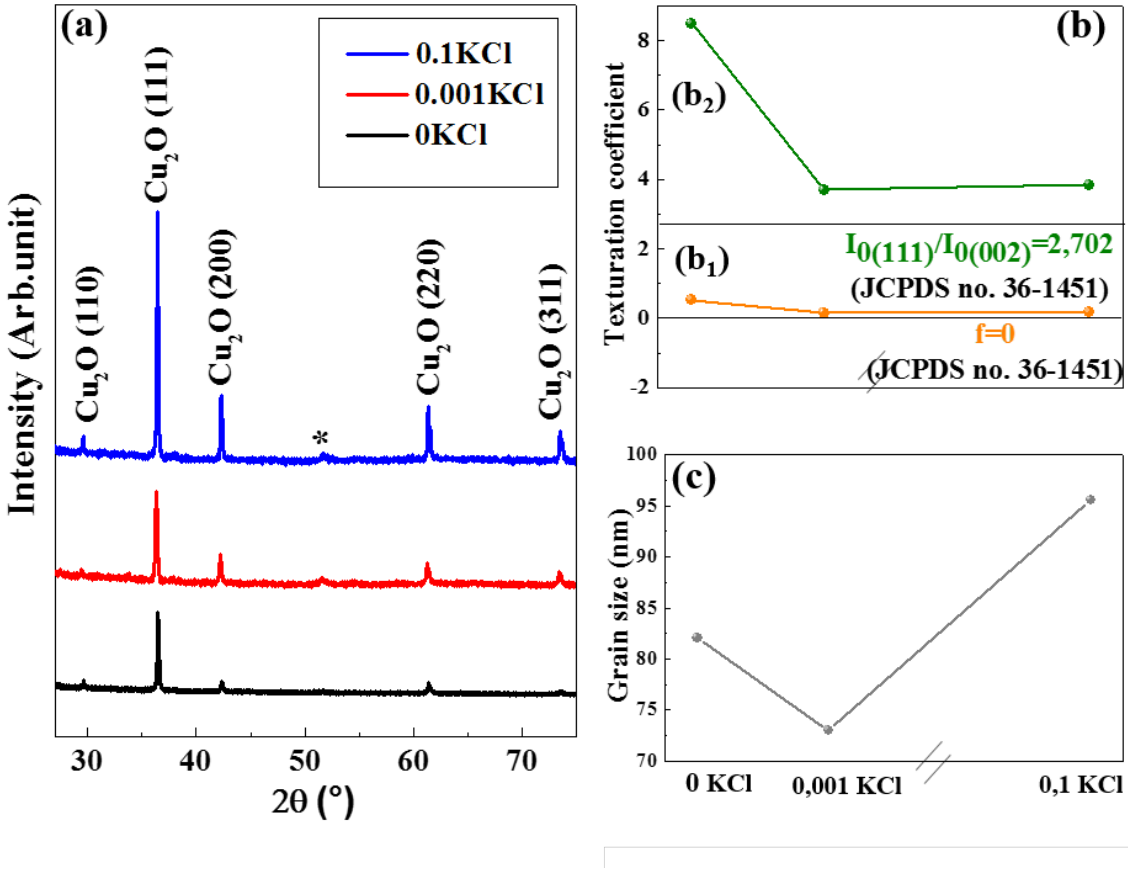

Figure 5.7: a) XRD patterns of Cu_2O nanostructures electrodeposited on FTO without and with different concentrations of KCl. b) Texture coefficients: b_1) f parameter of X-ray diffraction peaks as a function of the concentrations of KCl. $b2$) $I_{(111)}/I_{(200)}$) as a function of the concentrations of KCl. (111) and (200) are the main diffraction peaks from the Cu_2O films.

The black lines show the corresponding factors obtained from (JCPDS card, No°. $05-0667$) for the polycrystalline Cu_2O. It seems clear that the texturation factors is situated above the reference line for all the deposited Cu_2O films, regardless is the chloride concentration in the electrolyte, which confirms that the films are of best quality. The highest factor value is corresponding to Cu_2O free of Cl^-. The grain size is shown in Fig. (5.7)(c), where it seems clear that is proportional to the texturation following (111), which is confirmed by the SEM images. where The crystals in the dendritic branching

growth have the biggest size. Tab. (5.1) summarizes the effect of the concentration of the Cl^- ions on the crystallographic parameters

Table 5.1: KCl's concentration effect on the structural properties of Cu_2O nanostructures.

Sample	β **(nm)**	**D (nm)**	$I_{(111)}/I_{(200)}$	**f**
Free of Cl^-	0.20381	82.051	8.4795	0.516
0.001 Cl^-	0.22897	73.002	3.6888	0.1545
0.1 Cl^-	0.175	95.545	3.8404	0.1740

5.3.3 Electrochemical measurements

5.3.3.1 Photocurrent analysis

Fig. (5.8) presents the photocurrent of the Cu_2O samples recorded under a chopped light in a $0.5M$ Na_2SO_4 and an applied potential of $0V/SCE$. All the samples show reproducible photocurrent with time. Under the illumination, a decrease in the current was noted (cathodic photocurrent) indicating that the deposited Cu_2O films behave as a p-type semiconductor in the absence or the presence of the Cl^- ions, which confirms the $M-S$ results. The photocurrent generated was $28.0\mu A$ for the Cu_2O film free of Cl^-. The Cu_2O film deposited in the presence of the Cl^- $(0.001M)$ shows a lower photocurrent of $11.0\mu A$. This decrease may be due to the small quantity of the deposited Cu_2O in this concentration compared to that deposited in the absence of the Cl^- confirmed in the SEM images. However, the deposited Cu_2O film in a higher Cl^- concentration $(0.1M)$ reveals the highest response of $36.4\mu A$. This improvement can be explained by the surface continuity in the dendritic branching morphology compared to the cubic morphology [178], which facilitates the carrier transport in the Cu_2O electrolyte interface.

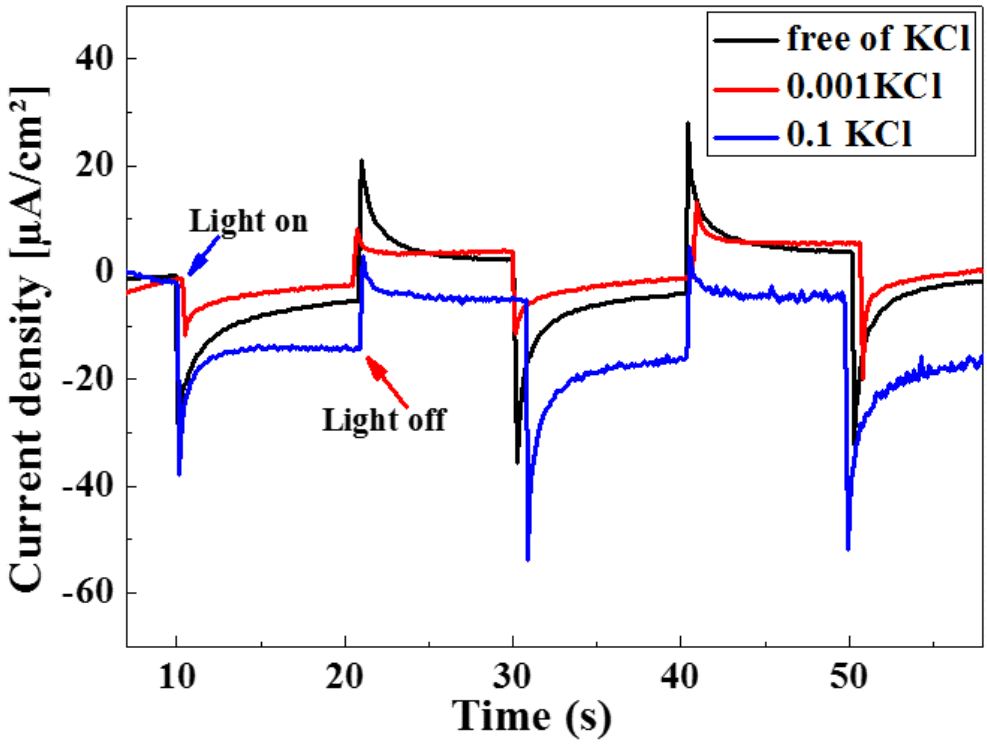

Figure 5.8: Photocurrent measured from Cu_2O nanostructures deposited , without KCl, with $0.001MKCl$ and $0.1MKCl$.

5.3.3.2 Mott–Schottky (M–S) measurements

The conduction type, the flat band (E_{fb}), and the acceptor densities of the deposited Cu_2O nanostructures were determined by studying the semiconductor electrolyte interface using the Mott–Schottky (M-S) measurements. In which, the depletion layer capacitance $C^{-2}vs.E$, at a fixed frequency, was measured and presented as an $M-S$ plot following the equation Eq. (2.2) [103]: Fig. (5.9) shows the Mott-Schottky plots of the Cu_2O nanostructures, obtained at different Cl^- concentrations, in a $0.5M$ Na_2SO_4 and a fixed frequency of $20KHz$. It is clear that the slope of the linear part of the capacitance curves, as a function of the applied potential in the depletion zone, is negative, which indicates that all the samples are p-type semiconductors. The use of Cl^- as a doping agent (Fig. (5.9)(b) and Fig. (5.9)(c)) makes it possible to improve the electrical properties of the Cu_2O, it increases the concentration of the charge carriers of this oxide by the occupation of the Cu/O substitutional sites. Indeed, the determination of the flat band potential E_{fb}

is done by extrapolating the linear part of the Schottky curves. From the slope of the line, we can estimate the density of the donor carriers N_A. The values of E_{fb} and N_A that calculated without and with different concentrations of Cl^- ions are summarized in the Tab. (5.2). The values of the obtained N_A are $1.29 \times 10^{17} cm^{-3}$, $2.89 \times 10^{17} cm^{-3}$, and $3.31 \times 10^{18} cm^{-3}$, respectively, for Cu_2O thin films free of Cl^-, with $0.001M$ Cl^- and $0.1MCl^-$. We observed that the concentration of the charge carriers increases from $1.29 \times 10^{17} cm^{-3}$ to $3.31 \times 10^{18} cm^{-3}$ (30 times largest) with increasing the concentration of Cl to $0.1M$. It is very important to note that these values of N_A are proportional to the KCl concentration. The Mott-Schottky measurements confirmed that the KCl in our study behave as a doping agent without any effect on the conduction type besides its additive behavior observed by the SEM.

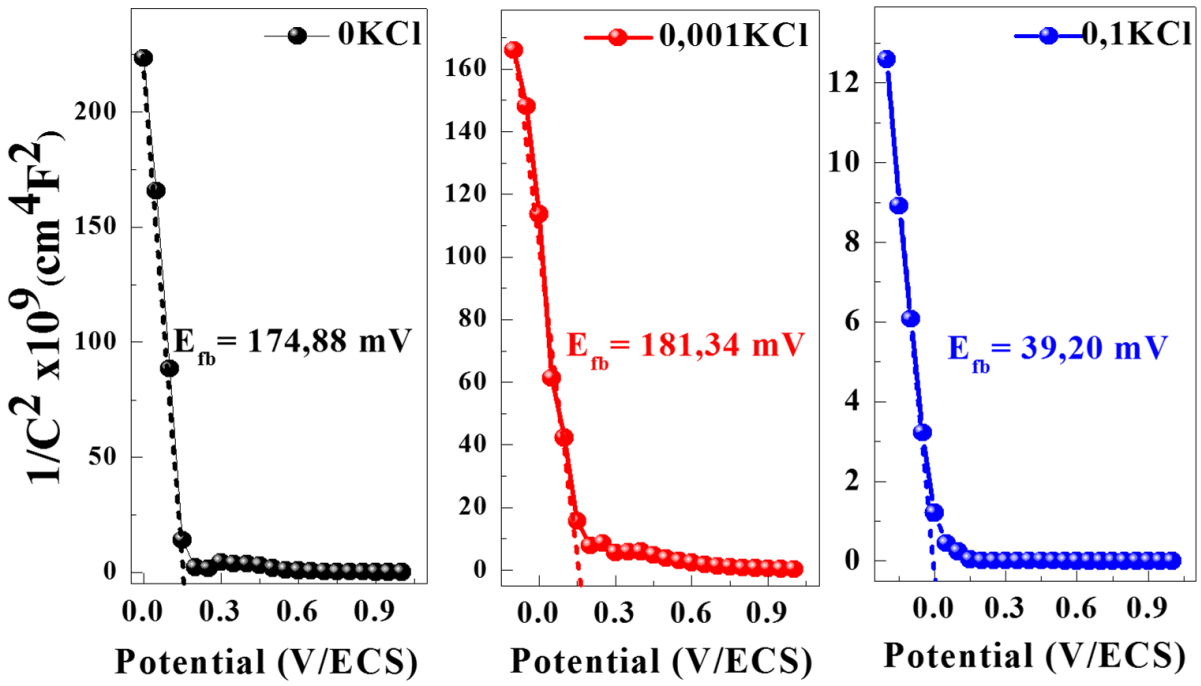

Figure 5.9: Mott–Schottky plots for Cu_2O nanostructures deposited (a) without KCl, (b) with $0.001MKCl$, (c) with $0.1MKCl$. The corresponding flat band potential values are indicated for the different plots.

Table 5.2: KCl concentration effect on the charge density of Cu_2O nanostructures.

Sample	E_{fb} **(mV/ECS)**	N_A (cm^{-3})
Free of Cl^-	174,88	1.29×10^{17}
0.001 Cl^-	181,34	2.89×10^{17}
0.1 Cl^-	39,20	3.31×10^{18}

5.3.4 Optical characterization

Optical measurements of the Cu_2O films without and with different concentrations of Cl^- ions were carried out at an ambient temperature using a UV-visible spectrophotometer. The spectral of which extends over is from 200 to $1100nm$. The different spectra of the optical response of samples with varying concentrations of Cl^- are shown in Fig. (5.10)(a). The shape of the set of transmission spectra fig9.a is identical whatever the concentration of $Cl-$ used. It seems clear that the samples have a low transmission $< 40\%$ in visible spectrum $(400nm - 800nm)$ and $< 60\%$ in near infra-red $(800nm - 1100)$ depending on the concentration of chloride. Practically, the light is totally absorbed in the range $< 500nm$ for the different spectra. The comparison of the optical absorption curves of the first sample without chloride (reference surface) with the two others shows clearly that the absorption decrease for$0.001M$ KCl, while it increase for $0.1M$ of KCl in the visible range. This result confirms that the chloride induces a modification of the structure and the surface of the Cu_2O deposits, which are presented by SEM and XRD. The decrease of absorption is due to the surface parctically covered by very clean grains of cubic shapes compared to the reference surface, which is totally covered confirmed SEM images. However, the decrease of transmission when the film grows in chlorine medium $(0.1MKCl)$, is due to the high surface area entirely covered by the dendritic branching growth. Fig. (5.10)(b) shows the $(\alpha h\nu)^2$ versus the photon energy $(h\nu)$ to determinate the optical band gap for the different Cu_2O films. The Tauc relation is used, given by Eq. (2.5) [110]. the optical band gap can be acheived by extrapolating downwards to the photon energy axis for the corresponding straight lines [110]. From the inset of Fig. (5.10)(b), we

can see the variation of the band gap energy, for the different KCl concentrations. It is worth-noting that the Cl^- ions have direct effect on the Eg, that is increases from 2.43 to 2.49 in film elaborated with low Cl^- concentration. However, it decreases to 2.13 in the chloride medium.

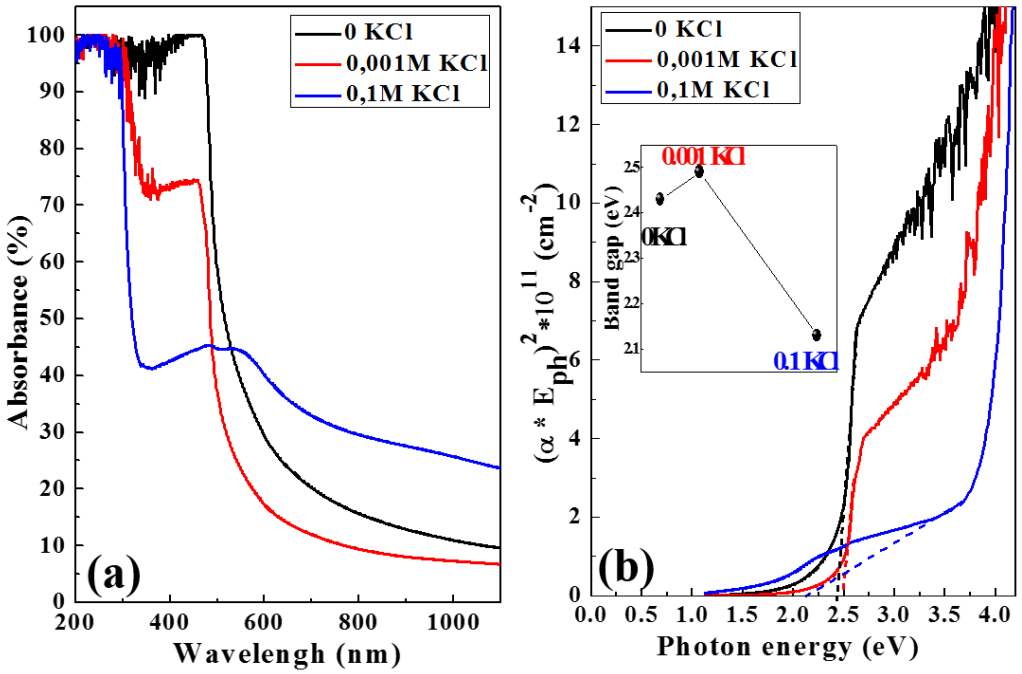

Figure 5.10: a) Absorbance spectra of the electrodeposited Cu_2O nanostructures without and with different concentrations of KCl. b) The Tauc plots as function of the the KCl concentration.

5.4 Conclusion

In summary, two different types of Cu_2O polyhedrons microcrystals have been successfully prepared and evaluated for photoelectrochemical (PEC) stability. On the other hand, different morphologies of Cu_2O nanostructures have been prepared and characterized. We have demonstrated experimentally that the Ammonium Chloride (NH_4Cl) and the potassium Chloride (KCl) have a big effects on the structure, the composition, the size, and especially on the morphology of both Cu_2O microcrystals and nanostructures. Cu_2O 26-facet polyhedral microcrystals can be changed to 18-polyhedral Cu_2O microcrystals

in the presence of NH_4Cl. In addition to the total change of structure orientation and chemical composition, the presence of KCl with the high concentration change totally the morphology from cubic nanostructures to dendrites of polyhedral shape and ameliorate the absorbance, due to high surface area. Through photocurrent measurement, we have confirmed good stability for the Cu_2O nanostructures prepared in chlorine medium and desirable electrical proprieties for charge transport by Mott-Schottky measurement. While it ameliorated the surface of nanocubes in low concentration. High photoelectrochemical (PEC) stability of 73.5% was achieved from Cu_2O 26-facet polyhedral. This result gives an opportunity for future utilization of Cu_2O polyhedral in a large range of applications such as photovoltaic, water splitting, and photochemical decomposition of pollutants. Taken together, this study may provide a new and facile way to control the morphology of other semiconductor materials using this additive. We also confirmed that the presence of KCl in the solution could not change the conduction type of Cu_2O regardless of its concentration in the solution.

Chapter 6

Potentiostatic and galvanostatic electrodeposition of $p - Cu_2O/n - ZnO_{(NW)}/ZnO^{(g)}_{(NS)}$ heterojunction

6.1 Introduction

METAL oxide semiconductors are promising alternatives for large-scale applications due to their abundance in nature, non-toxicity, and low-cost[179, 180]. The theoretical power conversion efficiency limit of a Cu_2O-based solar cell is approaching the 18–20%[20] according to Shockley-Queisser (SQ) limit. ZnO thin film is an alternative window material for Cu_2O based optoelectronic applications owing to its stable structure and high optical transmittance in the visible region. Optimum crystallinity and optical properties of ZnO thin films and good band alignment with the Cu_2O layer are two important steps for an efficient heterojunction. On the other hand, natural vacancy and interstitial defects in the ZnO crystal play a crucial role in the electronic properties of the structure; reveal additional energy levels within the band gap, and change the junction efficiency [181, 182]. In order to reduce these defects, various studies were carried out to improve the crystallinity[183, 184]. Furthermore, many strategies have been proposed by studying the effect of electrochemical parameters on the $p - Cu_2O/n - ZnO$ efficiency. In this chapter, we propose different architectures in order to study the mode effect on

the final performance of $p-Cu_2O/n-ZnO_{(NW)}/ZnO^{(g)}_{(NS)}$ heterostructure. The different samples in the present work were prepaped following Fig. (6.1) steps

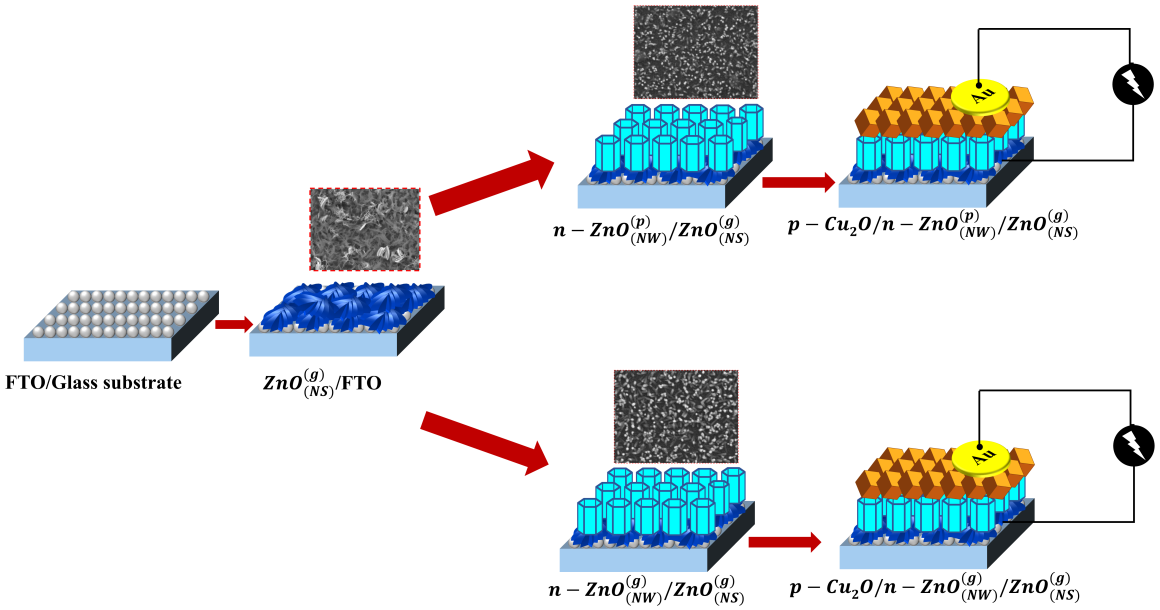

Figure 6.1: Processing steps for the fabrication of $p-Cu_2O\Big/n-ZnO^{(p)}_{(NW)}\Big/ZnO^{(g)}_{(NS)}$ and $p-Cu_2O\Big/n-ZnO^{(g)}_{(NW)}\Big/ZnO^{(g)}_{(NS)}$ heterojunctions for solar cell application.

Table 6.1: Different designs of the elaborated heterojunctions based on ZnO and Cu_2O nanostructures.

	Heterojunctions based on $ZnO^{(NW)}_{(p)}$				Heterojunctions based on $ZnO^{(NW)}_{(g)}$
Junction	**Joc1**	**Joc2**	**Joc3**	**Joc4**	**Joc5**
Seed layer	$ZnO^{(NS)}_{(g)}$	$ZnO^{(NS)}_{(g)}$	$ZnO^{(NS)}_{(g)}$	$ZnO^{(NS)}_{(g)}$	$ZnO^{(NS)}_{(g)}$
Conductive layer	$ZnO^{(NW)}_{(p)}$	$ZnO^{(NW)}_{(p)}$	$ZnO^{(NW)}_{(p)}$	$ZnO^{(NW)}_{(p)}$	$ZnO^{(NW)}_{(g)}$
Absorber layer	$Cu_20^{(11)}_{(p)}$	$Cu_20^{(11)}_{(g)}$	$Cu_20^{(12)}_{(p)}$	$Cu_20^{(12)}_{(g)}$	$Cu_20^{(11)}_{(p)}$

6.2 pH effect as function of the elaboration mode on $p-Cu_2O/n-ZnO^{(p)}_{(NW)}/ZnO^{(g)}_{(NS)}$ heterojunction

In this part, the Cu_2O, as absorber layer, will be elaborated in different pH media and elaboration approaches in order to investigate their effect on $p-Cu_2O/n-ZnO_{(NW)}/ZnO^{(g)}_{(NS)}$ performance. Where $n-ZnO_{(NW)}/ZnO^{(g)}_{(NS)}$ is the conductive layer.

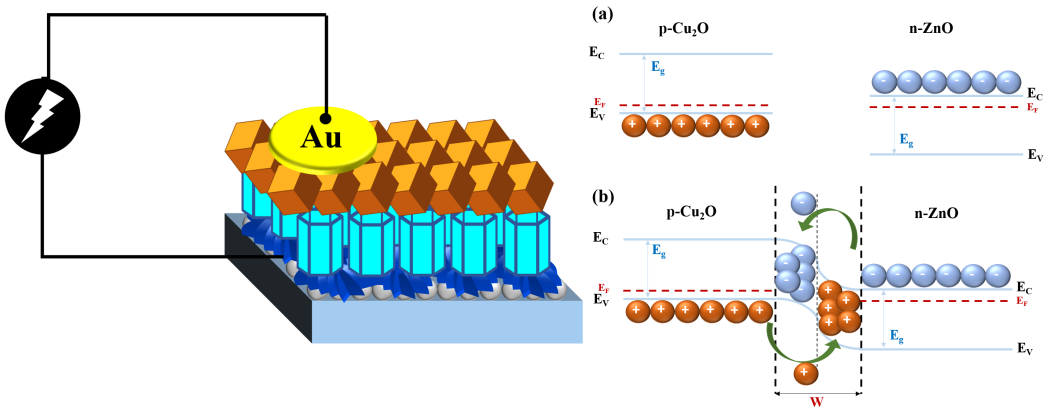

Figure 6.2: a) Schematic design of the sythesized $p-Cu_2O/n-ZnO_{(NW)}/ZnO^{(g)}_{(NS)}$ heterojunction. b) Energitic diagram before and after contact

6.2.1 Deposition mechanism of Cu_2O nanostructures on $n-ZnO^{(p)}_{(NW)}/\ ZnO^{(g)}_{(NS)}$ films

Fig. (6.3)(a) shows the current density-time curves (potentiostatic mode) during the electrodeposition of the Cu_2O nanostructures on the $n-ZnO^{(p)}_{(NW)}/ZnO^{(g)}_{(NS)}/FTO$ substrate in different pH media. It can be seen that the nucleation and growth steps are more observable in pH 12 ($joc3$). Which reached the plateau region after $450sec$. However, in pH 11($joc1$), only the diffusion step is observed. Which may be due to the resistivity of substrate.

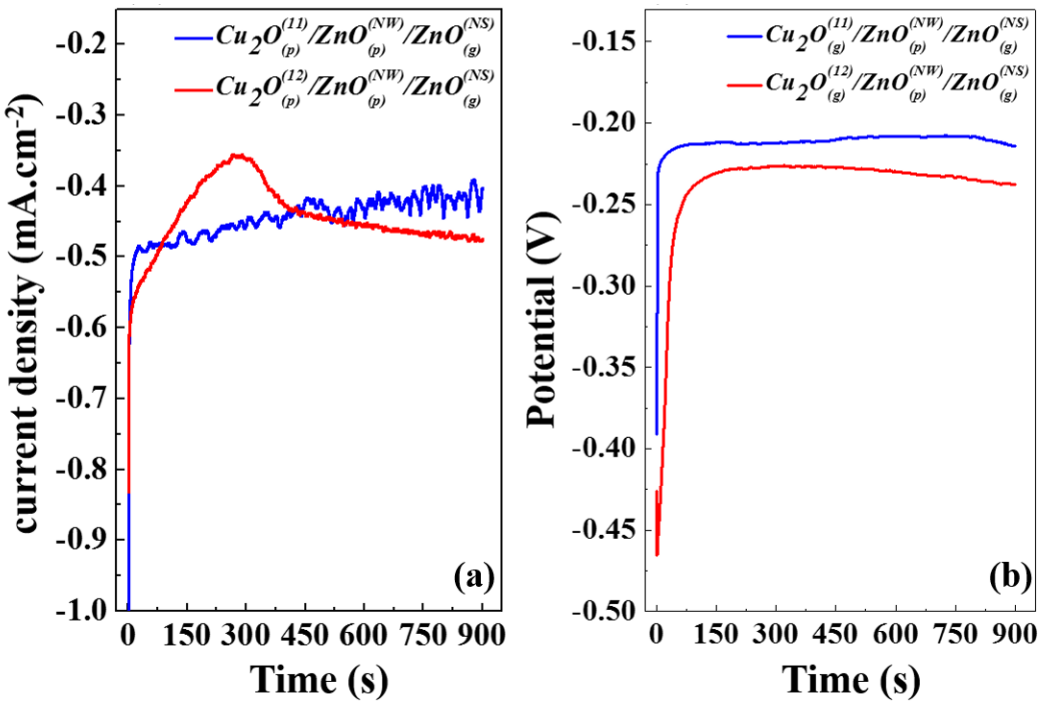

Figure 6.3: a) Chronoamperograms obtained during deposition of Cu_2O thin films on $n-ZnO^{(p)}_{(NW)}/ZnO^{(g)}_{(NS)}$ at 70 °C and different pH media during $15min$, from an electrolyte containing $0.05M$ $CuSO_4$, $0.06M$ citric acid,and $NaOH$ to adjust the pH b) The correponding Chronopotentiograms in identical conditions.

Fig. (6.3)(b) shows the potential-time curves (galvanostatic mode) during the electrodeposition of the Cu_2O nanostructures on the $n-ZnO^{(p)}_{(NW)}/ZnO^{(g)}_{(NS)}/FTO$ substrate in different pH media. It can be seen that the plateau (diffusion stage) is reached at $-0.25V$ in pH 12 ($joc4$). However, in pH 11 ($joc2$), it has been observed at $-0.22V$. Which confirms that the the growth of Cu_2O nanostructures on the $n-ZnO^{(p)}_{(NW)}/ZnO^{(g)}_{(NS)}/FTO$ substrate, is faster by increasing the pH of the electrolyte.

6.2.2 Structural characterization

Fig. (6.4)(a) shows the XRD patterns of $ZnO^{(p)}_{(NW)}$ with prefertial orientation along (002), corresponding to the c-axis, is the most intense peak, which could cover the rest. Which favors the transverse growth of nanostructure perpendicular to the substrate surface (1D ZnO nanostrures).

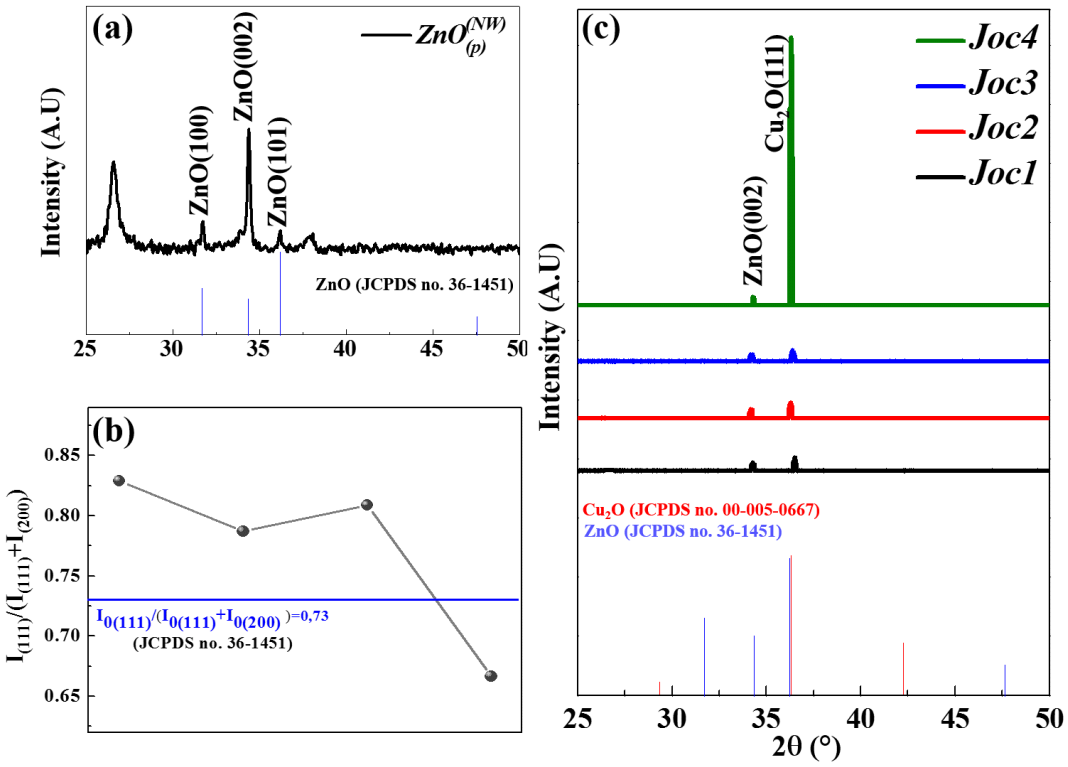

Figure 6.4: a) XRD pattern of ZnO nanowires electrodeposited potentiostatically. b) XRD pattern of the obtained $p-Cu_2O/n-ZnO^{(p)}_{(NW)}/ZnO^{(g)}_{(NS)}$ heterojunctions

Fig. (6.4)(b) shows the texture coefficient of the absorber substrates ($Cu_2O^{(11)}_{(p)}$, $Cu_2O^{(11)}_{(g)}$, $Cu_2O^{(12)}_{(p)}$, and $Cu_2O^{(12)}_{(g)}$). X-ray diffraction has been performed on the different heterojunctions ($Joc1$, $Joc2$, $Joc3$, and $Joc4$), where the XRD patterns are shown in Fig. (6.4)(c). No additional peaks or impurities were seen, only corresponding peaks to the Cu_2O and ZnO were observed, according to (JCPDS no. 00-005-0667) and (JCPDS no. 36-1451) respectively. show clearly polycrystalline materials. Moreover, only one peak corresponds to (111) orientation plane for Cu_2O, accompanied by the presence of (002) of ZnO. High crystallization is observed in the different hetejunctions.

6.2.3 Optical characterization

The optical absorbance spectrum of Cu_2O are shown in Fig. (6.5)(a), the absorption edge is observed at $500nm$. Which has been impouved and shifted to $500nm$ for all

the $p-Cu_2O/n-ZnO^{(p)}_{(NW)}/ZnO^{(g)}_{(NS)}$ films. The band gap energies were calculated in Chapter 4 for $Cu_2O^{(11)}_{(p)}$, $Cu_2O^{(11)}_{(g)}$, $Cu_2O^{(12)}_{(p)}$, and $Cu_2O^{(12)}_{(g)}$). Where, all the values are summerized in Tab. (4.7)

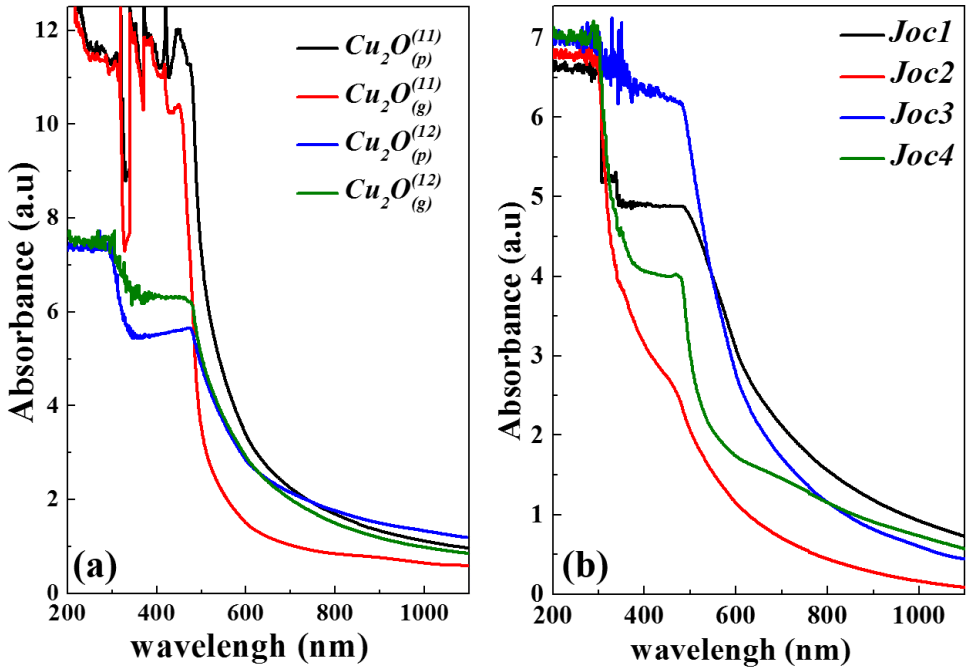

Figure 6.5: a) Absorbance spectra of the electrodeposited Cu_2O nanostructures within different pH media and under different deposition approches. b) Absorbance spectra of the corresponding $p-Cu_2O/n-ZnO^{(p)}_{(NW)}/ZnO^{(g)}_{(NS)}$ heterojunctions .

6.2.4 Morphological characterization

Fig. (6.6) shows the SEM images of $Joc1, Joc2, Joc3$, and $Joc4$. In general look, typical cubic Cu_2O, as a superficial layer, were observed for the different junctions. However, they are not oriented in the same way which in agreement with the corresponding Cu_2O layers Fig. (4.14). Homogeneous pyramidal morphology is shown using potentiostatic approach, means cubs were growing following the {100} plan, which confirms the high crystallographic orientation following (111) regardless of the pH. However, the cubs are exposed into {100}, and {111} plans, which can be explain by the competition in reaction between the (111) and (200) crystallographic orientation, which has been confirmed Chapter 4 in

order to stuy the mode effect. Under galvanostatic approach the grains quantity is lower, which can be explained by the lower rate of growth, compared to the potentiostatic one.

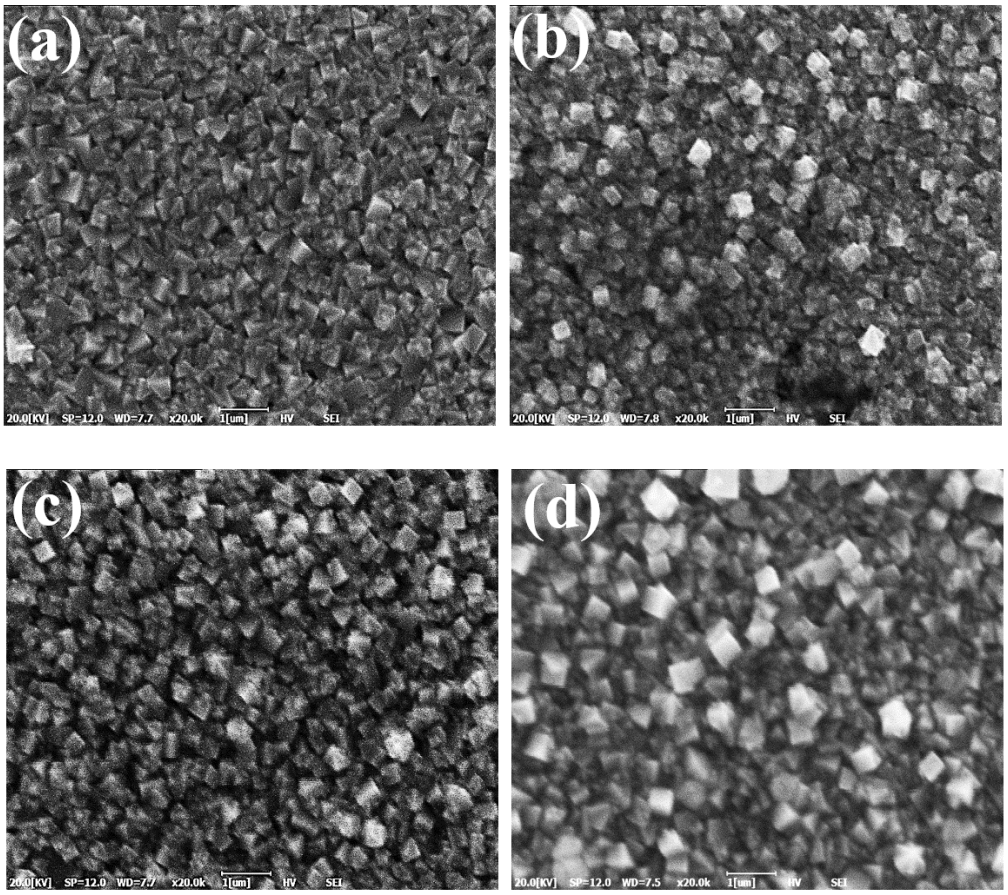

Figure 6.6: SEM images of a)Joc1, b)Joc2, c)Joc3, and d) Joc4.

6.2.5 I-V characterization

The electrical characteristic of the electrodeposited $p-Cu_2O/n-ZnO^{(p)}_{(NW)}/ZnO^{(g)}_{(NS)}$ heterojunction devices was investigated under dark conditions through the current vs voltage (I-V) electrical characterization. Fig. (6.7) illustrated typical I-V characteristics recorded for $Au/p{-}Cu_2O/n{-}ZnO^{(p)}_{(NW)}/ZnO^{(g)}_{(NS)}/FTO$ heterojunction devices in different elaboration conditions.

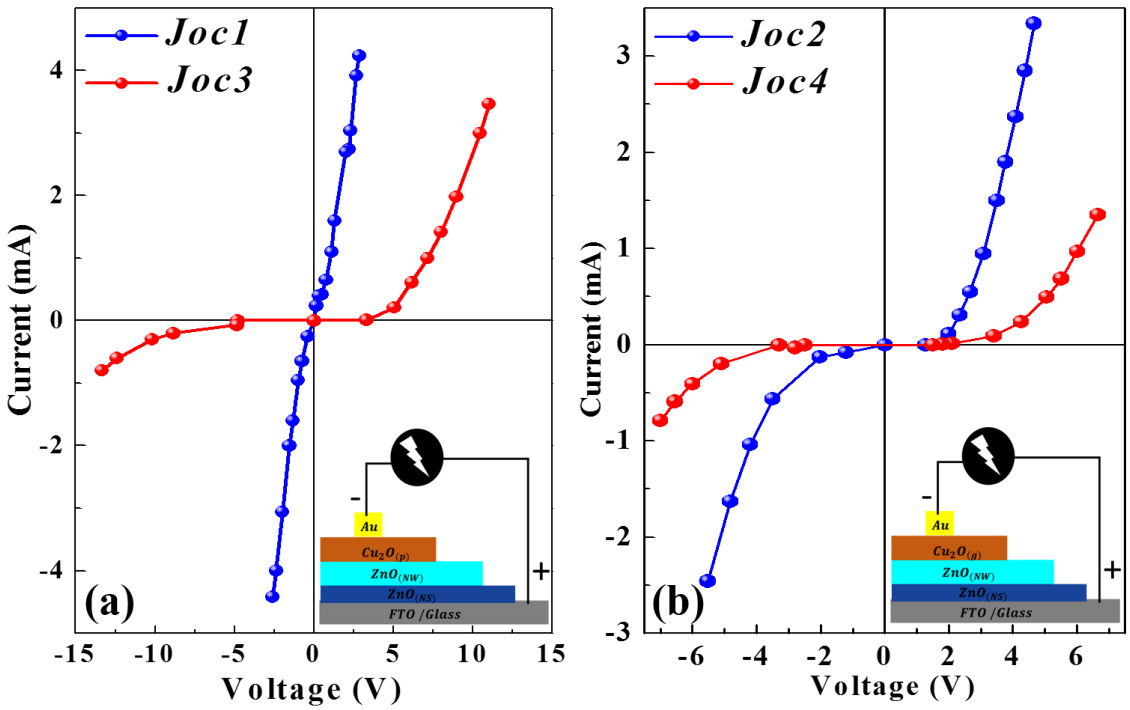

Figure 6.7: Current density–voltage characteristics of $p-Cu_2O/n-ZnO^{(p)}_{(NW)}/ZnO^{(g)}_{(NS)}$ heterojunctions in the dark. Inset of the figure illustrates the corresponding heterojunction design.

The obtained results revealed the successful formation of $p-n$ junctions at the interface between the $ZnO^{(p)}_{(NW)}$ and Cu_2O. It is worth noting that the I-V characteristic curves of Cu_2O/FTO show Ohmic behavior over the entire voltage region ranging from -1 to $+1V$. As a comparison of the two I-V curves corresponding to $Joc1$ and $Joc3$ (Fig. (6.7)(a)) reveals that $p-Cu_2O/n-ZnO^{(p)}_{(NW)}/ZnO^{(g)}_{(NS)}$ based on $Cu_2O^{(12)}_{(p)}$ $(Joc3)$ shows better performance, which presents significant rectification behavior. On the other hand, under galvanostatic mode (Fig. (6.7)(b)) $p-Cu_2O/n-ZnO^{(p)}_{(NW)}/ZnO^{(g)}_{(NS)}$ based on $Cu_2O^{(12)}_{(g)}$ $(Joc4)$ shows better performance. As a result, we can say that the performance of the $p-Cu_2O/n-ZnO^{(p)}_{(NW)}/ZnO^{(g)}_{(NS)}$ can be improved by increasing the pH of the electrolyte during the growth of Cu_2O absorber layer. It has been achieved from Chapter 4 that the pH increasing reduce the band gap, maybe this is the reason which affects the the alignment of the energy bands in $p-Cu_2O/n-ZnO^{(p)}_{(NW)}/ZnO^{(g)}_{(NS)}$ heterojunction.

6.3 Elaboration mode effect on $p-Cu_2O/n-ZnO^{(g)}_{(NW)}/ZnO^{(g)}_{(NS)}$ heterojunction

6.3.1 Structural characterization

Fig. (6.8)(a) shows the XRD patterns of $ZnO^{(g)}_{(NW)}$ with prefertial orientation along (002), corresponding to the c-axis.

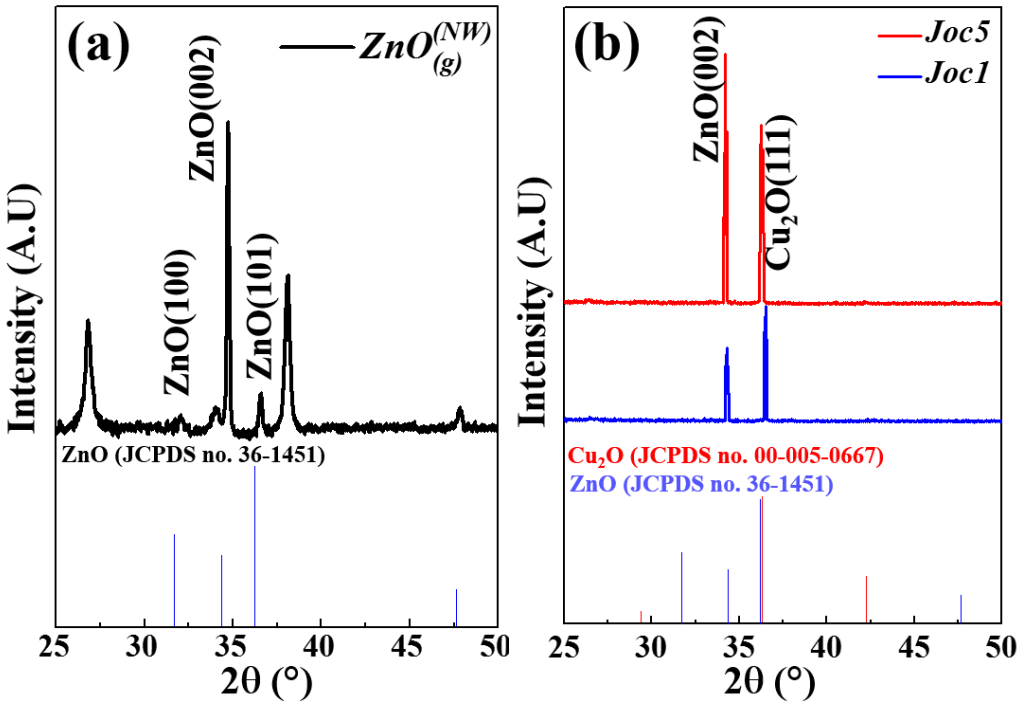

Figure 6.8: a) XRD pattern of ZnO nanowires electrodeposited galvanostatically. b) XRD pattern of the obtained $p-Cu_2O/n-ZnO^{(g)}_{(NW)}/ZnO^{(g)}_{(NS)}$ heterojunctions

Fig. (6.8)(b) shows the XRD patterns for $joc1$ and $joc5$. No additional peaks or impurities were seen, only corresponding peaks to the Cu_2O and ZnO were observed, according to (JCPDS no. 00-005-0667) and (JCPDS no. 36-1451) respectively. show clearly polycrystalline materials. Moreover, only one peak corresponds to (111) orientation plane for Cu_2O, accompanied by the presence of (002) of ZnO. It can be seen that texturization changed when the ratio between peaks inverted by changed the elaboration mode of $ZnO^{(g)}_{(NW)}$ (condctive layer).

6.3.2 I-V characterization

Fig. (6.9) illustrated typical I-V characteristics recorded for $Au/p-Cu_2O/n-ZnO^{(p)}_{(NW)}/ZnO^{(g)}_{(NS)}/FTO$ heterojunction devices in as function of the elaboration mode on the $ZnO_{(NW)}$.

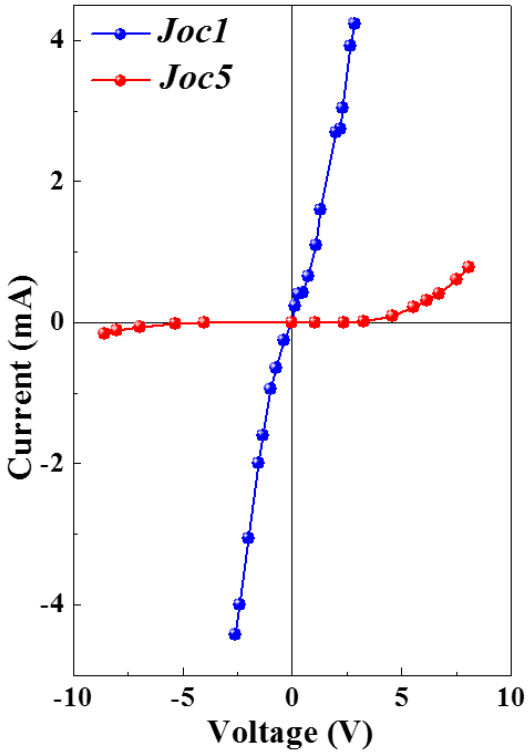

Figure 6.9: Current density–voltage characteristics of $p-Cu_2O/n-ZnO^{(g)}_{(NW)}/ZnO^{(g)}_{(NS)}$ heterojunctions in the dark.

The obtained results revealed the successful formation of $p-n$ junctions at the interface between the $ZnO_{(NW)}$ and $Cu_2O_{(p)}$. As a qualitative comparison of the two I-V curves of $Joc1$ and $Joc5$. $Joc5$ shows better performance, which presents significant rectification behavior.

6.4 Conclusion

In the previous chapter, $p-Cu_2O/n-ZnO_{(NW)}/ZnO^{(g)}_{(NS)}$ heterojunctions were successfully realized using simple method of elaboration. By increasing the pH a little bit the performance of the heterojunction significantly improved. As well as when the elaboration mode of the conductive layer transforms from potentiostatic to galvanostatic the rectification behavior significantly enhanced.

Conclusions

In summery, ZnO and Cu_2O nanostructures were successfully elaborated using electrodeposition way. The work presented, throughout this thesis, is dedicated to study the electrochemical deposition key parameters (applied current density, mode of elaboration, pH of medium, additives) on the electrochemical, optical, structural, and morphological properties of metal oxides (ZnO and Cu_2O) grown using electrodeposition method. So, the manuscript is composed of; an introduction, six chapters, and a conclusion.

Chapter 1 illustrates basics on semiconductors, $p-n$junctions, metal oxides used, and background on thin films for photovoltaic application

Chapter 2 shows the experimental setup, elaboration conditions including the solution preparation details and the characterization techniques.

In Chapter 3, significant effects on the electrochemical, structural, optical, and topographical proprieties had been exhibited on ZnO nanostructures through this chapter, when the current density was varied. In this chapter, it has been demonstrated experimentally that, ZnO nanosheets are very sensitive to the variation of the applied current density, where the crystallization, the optical transmittance, and the electrochemical performance were strongly influenced. However, a weak effect is observed comparing the elaboration approaches in the case of ZnO nanosheets, whereas, the $ZnO^{(g)}_{(NS)}$ are the preferred one in terms of ease. Evidently, the synthesized $ZnO^{(g)}_{(NS)}$, by applying $-2mA.cm^{-2}$, achieves the optimum features to be a seed layer for ZnO nanowires. On the other hand, for ZnO nanowires, when the mode is transformed from galvano to potentio, the diameter and the length of the nanowires have been extended. However, the crystallization, opti-

cal transmittance, and electrochemical stability were ameliorated under the galvanostatic approach. It is worth noting that the donor carrier density was significantly improved under galvanostatic mode regardless of the film morphology. Each mode has its strengths for a specific application. So, it's a compromise to understand why we can not make a scientific decision about what is the best way to form nanowires without studying it in a clear application.

In Chapter 4, we have shown that the performance of Cu_2O nanostructures can be optimized by controlling the key parameters. Cu_2O nanostructures are very sensitive to the variation of the applied current density to control directly the structural orientation, which influence the film morphology and the charge carrier mobility. In our conditions, $-0.4\mu A.cm^{-2}$ was the optimal current density. In the other hand, the mode of elaboration can introduce a remarkable effect on the film properties. Using the potenstiostatic mode, the crystallization is significantly improved. However, the absorption coefficient can be improved under galvanostatic mode. By increasing bath pH, the roughness and the absorption coefficient increase. It is very important to note, there is a compromise when you study, the electrodeposition parameter effect on final film features. Because, it is related to the application.

In Chapter 5, Cu_2O polyhedrons with two different shapes were successfully elaborated by galvanostatic electrochemical depositiond in selected growth mediums. Cu_2O show highly symmetric 26-facet polyhedral microcrystals with well-defined {100}, {110}, {111} crystallographic faces. In the presence of additive (NH_4Cl), Cu_2O show 18-polyhedral with well-developed {100} and {110} faces. The two morphologies revealed $p-$type semiconducting behavior. The effect of potassium chloride (KCl) on Cu_2O nanostructures electrodeposited were also studied in this chapter, in order to investigate itseffect on their structure, morphology, conduction type, and their optical properties. Cu_2O 26-facet polyhedral show a high photoelectrochemical (PEC) stability of 73.5%. Which is of great importance for future water splitting application. The conduction type of Cu_2O nanostructures does not change regardless, the concentration of KCl in the electrolyte, and that chlorine ions can ameliorate the density of the donor carriers (30 times largest) and the morphologie can be totally changed when the concentration of Cl^- ions attends $0.1M$ from nanocubes

to dendrites of polyhedral shape. In Chapter 6, $p-Cu_2O/n-ZnO_{(NW)}/ZnO^{(g)}_{(NS)}$ heterojunctions were successfully realized using the optimum conditions achieved from Chapter 3 and Chapter 4. The performance of the heterojunction significantly improved, by increasing the pH a little bit. As well as when the elaboration mode of the conductive layer transforms from potentiostatic to galvanostatic.

Future work

In the previous thesis the mean electrodepostion parameters well succceffuly studied for both ZnO and Cu_2O nanostructures with different morphologies. As present work, we propose to study the thickness effect, of the cunductive layer and the absorber layer, on $p-Cu_2O/n-ZnO_{(NW)}/ZnO^{(g)}_{(NS)}$ performance. As well, we propose to play on the absorber layer by adding Cu_2O nanoparticles ($Cu_2O_{(NP)}$) or Cu_2O dendrites of polyhedral ($Cu_2O_{(DP)}$) as a superficial film to be in the direct contact with light.

Bibliography

[1] Michelle L Bell, Devra L Davis, and Tony Fletcher. A retrospective assessment of mortality from the London smog episode of 1952: the role of influenza and pollution. *Environmental health perspectives*, 112(1):6–8, 2004.

[2] Kirk R Smith, Nigel Bruce, Kalpana Balakrishnan, Heather Adair-Rohani, John Balmes, Zoë Chafe, Mukesh Dherani, H Dean Hosgood, Sumi Mehta, Daniel Pope, et al. Millions dead: how do we know and what does it mean? Methods used in the comparative risk assessment of household air pollution. *Annual review of public health*, 35:185–206, 2014.

[3] Colleen M McShane and Kyoung-Shin Choi. Photocurrent enhancement of n-type Cu_2O electrodes achieved by controlling dendritic branching growth. *Journal of the American Chemical Society*, 131(7):2561–2569, 2009.

[4] Goutam Kumar Dalapati, Himani Sharma, Asim Guchhait, Nilanjan Chakrabarty, Priyanka Bamola, Qian Liu, Gopalan Saianand, Ambati Mounika Sai Krishna, Sabyasachi Mukhopadhyay, Avishek Dey, et al. Tin oxide for optoelectronic, photovoltaic and energy storage devices: a review. *Journal of Materials Chemistry A*, pages Early–Access, 2021.

[5] Thanh Tai Nguyen, Malkeshkumar Patel, Jin-Won Kim, Woochan Lee, and Joondong Kim. Functional TiO_2 interlayer for all-transparent metal-oxide photovoltaics. *Journal of Alloys and Compounds*, 816:152602, 2020.

[6] Jin-Heng Li, Bo-Xiao Tang, Li-Ming Tao, Ye-Xiang Xie, Yun Liang, and Man-Bo Zhang. Reusable copper-catalyzed cross-coupling reactions of aryl halides with organotins in inexpensive ionic liquids. *The Journal of organic chemistry*, 71(19): 7488–7490, 2006.

[7] Mehrez E El-Naggar, Kamel Shoueir, et al. Recent advances in polymer/metal/metal oxide hybrid nanostructures for catalytic applications: a review. *Journal of Environmental Chemical Engineering*, 8(5):104175, 2020.

[8] Petra E de Jongh, Daniel Vanmaekelbergh, and John J Kelly. Cu_2O: a catalyst for the photochemical decomposition of water? *Chemical Communications*, (12): 1069–1070, 1999.

[9] Shaodong Sun. Recent advances in hybrid Cu_2O-based heterogeneous nanostructures. *Nanoscale*, 7(25):10850–10882, 2015.

[10] A Chen, S Haddad, YC Wu, TN Fang, S Kaza, and Z Lan. Erasing characteristics of Cu_2O metal-insulator-metal resistive switching memory. *Applied Physics Letters*, 92(1):013503, 2008.

[11] Shaodong Sun, Xiaoping Song, Dongchu Deng, Xiaozhe Zhang, and Zhimao Yang. Nanotwins in polycrystalline Cu_7S_4 cages: highly active architectures for enhancing photocatalytic activities. *Catalysis Science & Technology*, 2(7):1309–1314, 2012.

[12] Gopalu Karunakaran, Govindhan Maduraiveeran, Evgeny Kolesnikov, Suresh Kannan Balasingam, Denis Kuznetsov, and Manab Kundu. Hollow-structured $Cu0.4Zn0.6Fe_2O_4$ as a novel negative electrode material for high-performance lithium-ion batteries. *Journal of Alloys and Compounds*, 865:158769, 2021.

[13] Masanobu Izaki and Takashi Omi. Transparent zinc oxide films prepared by electrochemical reaction. *Applied Physics Letters*, 68(17):2439–2440, 1996.

[14] G Riveros, A Garmendia, D Ramirez, M Tejos, P Grez, H Gomez, and EA Dalchiele. Study of the electrodeposition of Cu_2O thin films from DMSO solution. *Journal of the Electrochemical Society*, 160(1):D28, 2012.

[15] Xiaoyun Fan, Ning Hua, Jian Xu, Zhen Wang, Hanzhong Jia, and Chuanyi Wang. Controllable synthesis of two different morphologies of Cu_2O particles with the assistance of carbon dots. *RSC Advances*, 4(32):16524–16527, 2014.

[16] M Tapiero, JP Zielinger, and C Noguet. Electrical conductivity and thermal activation energies in Cu_2O single crystals. *Physica status solidi (a)*, 12(2):517–520, 1972.

[17] M Tapiero, JP Zielinger, and C Noguet. Photomemory effect in Cu_2O single crystals. Phenomenology and interpretation. *physica status solidi (a)*, 33(1):155–166, 1976.

[18] Ying Yang, Juan Han, Xiaohui Ning, Wei Cao, Wei Xu, and Liejin Guo. Controllable morphology and conductivity of electrodeposited Cu_2O thin film: effect of surfactants. *ACS applied materials & interfaces*, 6(24):22534–22543, 2014.

[19] PE De Jongh, D Vanmaekelbergh, and JJ Kelly. Cu_2O: electrodeposition and characterization. *Chemistry of materials*, 11(12):3512–3517, 1999.

[20] William Shockley and Hans J Queisser. Detailed balance limit of efficiency of p-n junction solar cells. *Journal of applied physics*, 32(3):510–519, 1961.

[21] Seung Ki Baek, Ki Ryong Lee, and Hyung Koun Cho. Oxide pn heterojunction of Cu_2O/ZnO nanowires and their photovoltaic performance. *Journal of Nanomaterials*, 2013, 2013.

[22] Biswajit Ghosh, Rajarshi Roy, Sumit Chowdhury, Pushan Banerjee, and Subrata Das. Synthesis of SnS thin films via galvanostatic electrodeposition and fabrication of CdS/SnS heterostructure for photovoltaic applications. *applied surface science*, 256(13):4328–4333, 2010.

[23] Gabriel Oltean, Leif Nyholm, and Kristina Edström. Galvanostatic electrodeposition of aluminium nano-rods for Li-ion three-dimensional micro-battery current collectors. *Electrochimica Acta*, 56(9):3203–3208, 2011.

[24] Raul Salazar, Claude Lévy-Clément, and Valentina Ivanova. Galvanostatic deposition of ZnO thin films. *Electrochimica acta*, 78:547–556, 2012.

[25] Ali Eftekhari and Foroogh Molaei. Carbon nanotube-assisted electrodeposition. Part I: battery performance of manganese oxide films electrodeposited at low current densities. *Journal of Power Sources*, 274:1306–1314, 2015.

[26] Ken Matsuoka, Mitsuaki Okuhata, Naoki Hatsuta, and Masayuki Takashiri. Effect of composition on the properties of bismuth telluride thin films produced by galvanostatic electrodeposition. *Transactions of the Materials Research Society of Japan*, 40(4):383–387, 2015.

[27] Milica M Petrović, Ian J Slipper, Milan D Antonijević, Goran S Nikolić, Jelena Z Mitrović, Danijela V Bojić, and Aleksandar Lj Bojić. Characterization of a Bi_2O_3 coat based anode prepared by galvanostatic electrodeposition and its use for the electrochemical degradation of Reactive Orange 4. *Journal of the Taiwan Institute of Chemical Engineers*, 50:282–287, 2015.

[28] Gomaa AM Ali, Mashitah M Yusoff, Yun Hau Ng, Hong Ngee Lim, and Kwok Feng Chong. Potentiostatic and galvanostatic electrodeposition of manganese oxide for supercapacitor application: A comparison study. *Current Applied Physics*, 15(10): 1143–1147, 2015.

[29] Rachmat Adhi Wibowo, Raad Hamid, Thomas Maier, and Theodoros Dimopoulos. Galvanostatically-electrodeposited Cu–Zn–Sn multilayers as precursors for crystallising kesterite Cu_2ZnSnS_4 thin films. *Thin Solid Films*, 582:239–244, 2015.

[30] O Razmjoo, ME Bahrololoom, and P Najafisayar. The effect of current density on the composition, structure, morphology and optical properties of galvanostatically electrodeposited nanostructured cadmium telluride films. *Ceramics International*, 43(1):121–127, 2017.

[31] Ben G Streetman, Sanjay Banerjee, et al. *Solid state electronic devices*, volume 10. Pearson/Prentice Hall Upper Saddle River, 2006.

[32] Greg Sun. Intersubband approach to silicon based lasers—circumventing the indirect bandgap limitation. *Advances in Optics and Photonics*, 3(1):53–87, 2011.

[33] Pallab Bhattacharya. *Semiconductor optoelectronic devices*. Prentice-Hall, Inc., 1997.

[34] SR Elliott. The Physics and Chemistry of Solids, 2000. *ISBN-13*, pages 978–0.

[35] SJ Pearton, DP Norton, K Ip, YW Heo, and T Steiner. RETRACTED: Recent progress in processing and properties of ZnO, 2005.

[36] David Berney Needleman. *Optical design guidelines for spectral splitting photovoltaic systems: A sensitivity analysis approach*. PhD thesis, Massachusetts Institute of Technology, 2014.

[37] KL Chopra PD Paulson V Dutta. Thin-film solar cells: an overview. *Prog. Photovoltaics Res. Appl*, 12(23):69–92, 2004.

[38] Kasturi Lal Chopra and Suhit Ranjan Das. Why thin film solar cells? In *Thin film solar cells*, pages 1–18. Springer, 1983.

[39] Martin A Grenn. Solar Cell Operating Principles Technology And System Application" prenticell Hall. *Inc Evylewood Cliffs N, J*, 1982.

[40] Antonio Luque and Steven Hegedus. *Handbook of photovoltaic science and engineering*. John Wiley & Sons, 2011.

[41] Andres Cuevas, Ronald A Sinton, Neil E Midkiff, and Richard M Swanson. 26-percent efficient point-junction concentrator solar cells with a front metal grid. *IEEE electron device letters*, 11(1):6–8, 1990.

[42] Chetan Singh Solanki. *Solar photovoltaics: fundamentals, technologies and applications*. Phi learning pvt. Ltd., 2015.

[43] Giovanni Altamura. *Development of CZTSSe thin films based solar cells*. PhD thesis, Université Joseph-Fourier-Grenoble I, 2014.

[44] DA Cusano. CdTe solar cells and photovoltaic heterojunctions in II–VI compounds. *Solid-State Electronics*, 6(3):217–232, 1963.

[45] EI Adirovich, Yu M Yuabov, and GR Yagudaev. Photoelectric effects in film diodes with CdS-CdTe heterojunctions. *Sov Phys Semiconductors*, 3(1):61–64, 1969.

[46] Sigurd Wagner, JL Shay, P Migliorato, and HM Kasper. $CuInSe_2$/CdS heterojunction photovoltaic detectors. *Applied Physics Letters*, 25(8):434–435, 1974.

[47] LL Kazmerski, FR White, and GK Morgan. Thin-film $CuInSe_2$/CdS heterojunction solar cells. *Applied Physics Letters*, 29(4):268–270, 1976.

[48] Makoto Konagai, Mitsunori Sugimoto, and Kiyoshi Takahashi. High efficiency GaAs thin film solar cells by peeled film technology. *Journal of crystal growth*, 45:277–280, 1978.

[49] Teodor K Todorov, Jiang Tang, Santanu Bag, Oki Gunawan, Tayfun Gokmen, Yu Zhu, and David B Mitzi. Beyond 11% efficiency: characteristics of state-of-the-art Cu2ZnSn (S, Se) 4 solar cells. *Advanced Energy Materials*, 3(1):34–38, 2013.

[50] Wei Wang, Mark T Winkler, Oki Gunawan, Tayfun Gokmen, Teodor K Todorov, Yu Zhu, and David B Mitzi. Device characteristics of CZTSSe thin-film solar cells with 12.6% efficiency. *Advanced energy materials*, 4(7):1301465, 2014.

[51] Min-Teng Chen, Ming-Pei Lu, Yi-Jen Wu, Jinhui Song, Chung-Yang Lee, Ming-Yen Lu, Yu-Cheng Chang, Li-Jen Chou, Zhong Lin Wang, and Lih-Juann Chen. Near UV LEDs made with in situ doped pn homojunction ZnO nanowire arrays. *Nano letters*, 10(11):4387–4393, 2010.

[52] KL Chopra and PD Paulson. V. Dutta, V.,"Thin-Film Solar Cells: An Overview". *Prog. Photovolt: Res. Appl*, 12(2-3):69–92, 2004.

[53] Martin A Green. Solar cells: operating principles, technology, and system applications. *Englewood Cliffs*, 1982.

[54] PP Horley, L Licea Jiménez, SA Pérez García, J Álvarez Quintana, Yu V Vorobiev, R Ramírez Bon, VP Makhniy, and J González Hernández. Thin Film Solar Cells: Modeling, Obtaining and Applications. *Application of Solar Energy*, 2013.

[55] C Klingshirn. *ZnO*: From basics towards applications. *physica status solidi (b)*, 244 (9):3027–3073, 2007.

[56] Gaurav Malik, Satyendra Mourya, Jyoti Jaiswal, and Ramesh Chandra. Effect of annealing parameters on optoelectronic properties of highly ordered ZnO thin films. *Materials Science in Semiconductor Processing*, 100:200–213, 2019.

[57] Arijit Sarkar, Ajit K Katiyar, Amal K Das, and Samit K Ray. Si membrane–ZnO heterojunction-based broad band visible light emitting diode for flexible optoelectronic devices. *Flexible and Printed Electronics*, 3(2):025004, 2018.

[58] Kanghua Li, Rokas Kondrotas, Chao Chen, Shuaicheng Lu, Xixing Wen, Dengbing Li, Jiajun Luo, Yang Zhao, and Jiang Tang. Improved efficiency by insertion of Zn1- xMgxO through sol-gel method in ZnO/Sb_2Se_3 solar cell. *Solar Energy*, 167: 10–17, 2018.

[59] Subbian Karuppuchamy, K Nonomura, T Yoshida, T Sugiura, and H Minoura. Cathodic electrodeposition of oxide semiconductor thin films and their application to dye-sensitized solar cells. *Solid State Ionics*, 151(1-4):19–27, 2002.

[60] Faiz Rahman. Zinc oxide light-emitting diodes: a review. *Optical Engineering*, 58 (1):010901, 2019.

[61] Goki Eda, Giovanni Fanchini, and Manish Chhowalla. Large-area ultrathin films of reduced graphene oxide as a transparent and flexible electronic material. *Nature nanotechnology*, 3(5):270–274, 2008.

[62] Xuan Wang, Linjie Zhi, and Klaus Müllen. Transparent, conductive graphene electrodes for dye-sensitized solar cells. *Nano letters*, 8(1):323–327, 2008.

[63] Zongyou Yin, Shixin Wu, Xiaozhu Zhou, Xiao Huang, Qichun Zhang, Freddy Boey, and Hua Zhang. Electrochemical deposition of *ZnO* nanorods on transparent reduced graphene oxide electrodes for hybrid solar cells. *small*, 6(2):307–312, 2010.

[64] Won Il Park, Chul-Ho Lee, Jung Min Lee, Nam-Jung Kim, and Gyu-Chul Yi. Inorganic nanostructures grown on graphene layers. *Nanoscale*, 3(9):3522–3533, 2011.

[65] Sophie Peulon and Daniel Lincot. Cathodic electrodeposition from aqueous solution of dense or open-structured zinc oxide films. *Advanced Materials*, 8(2):166–170, 1996.

[66] Ümit Özgür, Ya I Alivov, Chunli Liu, A Teke, MAn Reshchikov, S Doğan, VCSJ Avrutin, S-J Cho, and H Morkoç. A comprehensive review of ZnO materials and devices. *Journal of applied physics*, 98(4):11, 2005.

[67] Romain Magnan. *Oxyde transparent conducteur de ZnO: V à partir d'une cible de nanoparticules: de l'ablation par laser pulsé à un procédé de décharge à barrière diélectrique double fréquence à pression atmosphérique*. PhD thesis, Université de Perpignan; Institut national de la recherche scientifique ..., 2020.

[68] Adriana Paracchino, Vincent Laporte, Kevin Sivula, Michael Grätzel, and Elijah Thimsen. Highly active oxide photocathode for photoelectrochemical water reduction. *Nature materials*, 10(6):456–461, 2011.

[69] Lok-kun Tsui and Giovanni Zangari. Modification of TiO_2 nanotubes by Cu_2O for photoelectrochemical, photocatalytic, and photovoltaic devices. *Electrochimica Acta*, 128:341–348, 2014.

[70] Y Nishi, T Miyata, J Nomoto, and T Minami. High-efficiency Cu_2O-based heterojunction solar cells fabricated on thermally oxidized copper sheets. In *2011 37th IEEE Photovoltaic Specialists Conference*, pages 000266–000270. IEEE, 2011.

[71] David O Scanlon, Benjamin J Morgan, Graeme W Watson, and Aron Walsh. Acceptor levels in p-type Cu_2O: rationalizing theory and experiment. *Physical Review Letters*, 103(9):096405, 2009.

[72] K Akimoto, S Ishizuka, M Yanagita, Y Nawa, Goutam K Paul, and T Sakurai. Thin film deposition of Cu_2O and application for solar cells. *Solar energy*, 80(6):715–722, 2006.

[73] Alberto Mittiga, Enrico Salza, Francesca Sarto, Mario Tucci, and Rajaraman Vasanthi. Heterojunction solar cell with 2% efficiency based on a Cu_2O substrate. *Applied physics letters*, 88(16):163502, 2006.

[74] LC Olsen, FW Addis, and W Miller. Experimental and theoretical studies of Cu_2O solar cells. *Solar cells*, 7(3):247–279, 1982.

[75] Y Abdu and AO Musa. Copper (I) oxide (Cu_2) based solar cells-a review. *Bayero Journal of Pure and Applied Sciences*, 2(2):8–12, 2009.

[76] AE Rakhshani. Preparation, characteristics and photovoltaic properties of cuprous oxide—a review. *Solid-State Electronics*, 29(1):7–17, 1986.

[77] GK Paul, Y Nawa, H Sato, T Sakurai, and K Akimoto. Defects in Cu_2O studied by deep level transient spectroscopy. *Applied physics letters*, 88(14):141901, 2006.

[78] Chengxiang Xiang, Gregory M Kimball, Ronald L Grimm, Bruce S Brunschwig, Harry A Atwater, and Nathan S Lewis. 820 mV open-circuit voltages from Cu_2O/CH_3CN junctions. *Energy & Environmental Science*, 4(4):1311–1318, 2011.

[79] AS Povarennykh. A short history of mineralogy and the classification of minerals. In *Crystal Chemical Classification of Minerals*, pages 3–26. Springer, 1972.

[80] Benjamin D Yuhas and Peidong Yang. Nanowire-based all-oxide solar cells. *Journal of the American Chemical Society*, 131(10):3756–3761, 2009.

[81] J Katayama, K Ito, M Matsuoka, and J Tamaki. Performance of Cu_2O /ZnO solar cell prepared by two-step electrodeposition. *Journal of Applied Electrochemistry*, 34 (7):687–692, 2004.

[82] SS Jeong, A Mittiga, E Salza, A Masci, and S Passerini. Electrodeposited ZnO/Cu_2O heterojunction solar cells. *Electrochimica Acta*, 53(5):2226–2231, 2008.

[83] T Yoshida, D Komatsu, N Shimokawa, and H Minoura. Mechanism of cathodic electrodeposition of zinc oxide thin films from aqueous zinc nitrate baths. *Thin solid films*, 451:166–169, 2004.

[84] CR Gorla, NW Emanetoglu, S Liang, WE Mayo, Y Lu, M Wraback, and H Shen. Structural, optical, and surface acoustic wave properties of epitaxial ZnO films grown on (0112) sapphire by metalorganic chemical vapor deposition. *Journal of Applied Physics*, 85(5):2595–2602, 1999.

[85] MK Puchert, PY Timbrell, and RN Lamb. Postdeposition annealing of radio frequency magnetron sputtered *ZnO* films. *Journal of Vacuum Science & Technology A: Vacuum, Surfaces, and Films*, 14(4):2220–2230, 1996.

[86] S Eisermann, A Kronenberger, M Dietrich, S Petznick, A Laufer, A Polity, and BK Meyer. Hydrogen and nitrogen incorporation in ZnO thin films grown by radio-frequency (RF) sputtering. *Thin Solid Films*, 518(4):1099–1102, 2009.

[87] Chung-Wei Kung, Hsin-Wei Chen, Chia-Yu Lin, Yi-Hsuan Lai, R Vittal, and Kuo-Chuan Ho. Electrochemical synthesis of a double-layer film of *ZnO* nanosheets/-nanoparticles and its application for dye-sensitized solar cells. *Progress in Photovoltaics: Research and applications*, 22(4):440–451, 2014.

[88] Thierry Pauporté, Oleg Lupan, Vasile Postica, Mathias Hoppe, Lee Chow, and Rainer Adelung. Al-Doped ZnO nanowires by electrochemical deposition for selective V_{OC} nanosensor and nanophotodetector. *physica status solidi (a)*, 215(16): 1700824, 2018.

[89] Tsukasa Yoshida, Jingbo Zhang, Daisuke Komatsu, Seiichi Sawatani, Hideki Minoura, Thierry Pauporté, Daniel Lincot, Torsten Oekermann, Derck Schlettwein, Hirokazu Tada, et al. Electrodeposition of inorganic/organic hybrid thin films. *Advanced Functional Materials*, 19(1):17–43, 2009.

[90] L Mentar, O Baka, MR Khelladi, A Azizi, S Velumani, G Schmerber, and A Dinia. Effect of nitrate concentration on the electrochemical growth and properties of *ZnO* nanostructures. *Journal of Materials Science: Materials in Electronics*, 26(2):1217–1224, 2015.

[91] Gerald Ensang Timuda and Keiko Waki. Controlling ZnO Nanosheet Morphology By Galvanostatic Electrodeposition. In *ECS Meeting Abstracts*, number 42, page 2122. IOP Publishing, 2016.

[92] Gerald Ensang Timuda and Keiko Waki. Galvanostatic electrodeposition of ZnO nanosheet: effect of different applied current densities and deposition times on the

nanosheet morphology. *Advances in Natural Sciences: Nanoscience and Nanotechnology*, 11(2):025005, 2020.

[93] M Stumpp, THQ Nguyen, C Lupo, and D Schlettwein. Interplay of Different Reaction Pathways in the Pulsed Galvanostatic Deposition of Zinc Oxide. *Electrochimica Acta*, 169:367–375, 2015.

[94] Yuchun Zhai, Huiqing Fan, Qiang Li, and Wei Yan. Morphology evolutions and optical properties of Cu_2O films by an electrochemical deposition on flexible substrate. *Applied surface science*, 258(7):3232–3236, 2012.

[95] Mazhar Ali Abbasi, Yaqoob Khan, Sajjad Hussain, Omer Nur, and Magnus Willander. Anions effect on the low temperature growth of ZnO nanostructures. *Vacuum*, 86(12):1998–2001, 2012.

[96] Gastón P Barreto, Graciela Morales, and Ma Luisa López Quintanilla. Microwave assisted synthesis of ZnO nanoparticles: effect of precursor reagents, temperature, irradiation time, and additives on nano-ZnO morphology development. *Journal of Materials*, 2013:1–11, 2013.

[97] Debabrata Pradhan and Kam Tong Leung. Controlled growth of two-dimensional and one-dimensional ZnO nanostructures on indium tin oxide coated glass by direct electrodeposition. *Langmuir*, 24(17):9707–9716, 2008.

[98] Ramon Tena-Zaera, Jamil Elias, Gillaume Wang, and Claude Levy-Clement. Role of chloride ions on electrochemical deposition of ZnO nanowire arrays from O_2 reduction. *The Journal of Physical Chemistry C*, 111(45):16706–16711, 2007.

[99] J Elias, R Tena-Zaera, and C Lévy-Clément. Electrochemical deposition of ZnO nanowire arrays with tailored dimensions. *Journal of Electroanalytical Chemistry*, 621(2):171–177, 2008.

[100] CGBt Garrett and W He Brattain. Physical theory of semiconductor surfaces. *Physical Review*, 99(2):376, 1955.

[101] Leo Chau-Kuang Liau and Jia-Lin Jhan. Investigation of rapid thermal annealing on Cu_2O properties and n-p Cu_2O homojunction performance by electrochemical deposition processing. *Journal of The Electrochemical Society*, 163(14):D787, 2016.

[102] Adriana Paracchino, Nripan Mathews, Takashi Hisatomi, Morgan Stefik, S David Tilley, and Michael Grätzel. Ultrathin films on copper (I) oxide water splitting photocathodes: a study on performance and stability. *Energy & Environmental Science*, 5(9):8673–8681, 2012.

[103] W John Albery, Gerald J O'Shea, and Alec L Smith. Interpretation and use of Mott–Schottky plots at the semiconductor/electrolyte interface. *Journal of the Chemical Society, Faraday Transactions*, 92(20):4083–4085, 1996.

[104] H Paul Maruska and Amal K Ghosh. Photocatalytic decomposition of water at semiconductor electrodes. *Solar Energy*, 20(6):443–458, 1978.

[105] H Gerischer. Electrochemical behavior of semiconductors under illumination. *Journal of the electrochemical society*, 113(11):1174, 1966.

[106] M Muhibbullah and Ashraf M Abdel Haleem. Estimation of the Open Circuit Voltage of a p-n Junction Based on Photoelectrochemical Measurements. *Transactions of the Materials Research Society of Japan*, 40(3):247–252, 2015.

[107] Kyeongsik Nam, Gyuri Choi, Hyungseup Kim, Mookyoung Yoo, and Hyoungho Ko. A Potentiostat Readout Circuit with a Low-Noise and Mismatch-Tolerant Current Mirror Using Chopper Stabilization and Dynamic Element Matching for Electrochemical Sensors. *Applied Sciences*, 11(18):8287, 2021.

[108] CE Jeffree. Light and Electron Microscopy., 1993.

[109] Sébastien Decossas. *Nanotribologie par microscopie à force atomique (AFM) sur des nanotubes de carbone*. PhD thesis, Grenoble 1, 2001.

[110] J Tauc and A Menth. States in the gap. *Journal of non-crystalline solids*, 8:569–585, 1972.

[111] RE Reason. Progress in the appraisal of surface topography during the first half-century of instrument development. *Wear*, 57(1):1–16, 1979.

[112] Tom R Thomas. *Rough surfaces*. World Scientific, 1998.

[113] M Parans Paranthaman, Winnie Wong-Ng, and Raghu N Bhattacharya. *Semiconductor materials for solar photovoltaic cells*, volume 218. Springer, 2016.

[114] Yamin Leprince-Wang, A Yacoubi-Ouslim, and GY Wang. Structure study of electrodeposited ZnO nanowires. *Microelectronics journal*, 36(7):625–628, 2005.

[115] Oleg Lupan, Thierry Pauporté, Bruno Viana, IM Tiginyanu, VV Ursaki, and Robert Cortes. Epitaxial electrodeposition of ZnO nanowire arrays on p-GaN for efficient $UV-$light-emitting diode fabrication. *ACS Applied Materials & Interfaces*, 2(7): 2083–2090, 2010.

[116] Masanobu Izaki, Tsutomu Shinagawa, Ko-Taro Mizuno, Yuya Ida, Minoru Inaba, and Akimasa Tasaka. Electrochemically constructed $p - Cu_2O/n - ZnO$ heterojunction diode for photovoltaic device. *Journal of Physics D: Applied Physics*, 40 (11):3326, 2007.

[117] Run Liu, Alexey A Vertegel, Eric W Bohannan, Thomas A Sorenson, and Jay A Switzer. Epitaxial electrodeposition of zinc oxide nanopillars on single-crystal gold. *Chemistry of Materials*, 13(2):508–512, 2001.

[118] Vincent Consonni, Joe Briscoe, Erki Kärber, Xuan Li, and Thomas Cossuet. ZnO nanowires for solar cells: a comprehensive review. *Nanotechnology*, 30(36):362001, 2019.

[119] Runze Chen, Chuan Liu, Kyeiwaa Asare-Yeboah, Ziyang Zhang, Zhengran He, and Yun Liu. Retracted Article: Wavelength modulation of ZnO nanowire based organic light-emitting diodes with ultraviolet electroluminescence. *RSC Advances*, 10(40): 23775–23781, 2020.

[120] Sikai Zhao, Yanbai Shen, Pengfei Zhou, Fulai Hao, Xiangyu Xu, Shuling Gao, Dezhou Wei, Yuxin Ao, and Yansong Shen. Enhanced NO_2 sensing performance

of ZnO nanowires functionalized with ultra-fine In_2O_3 nanoparticles. *Sensors and Actuators B: Chemical*, 308:127729, 2020.

[121] Yang Zhang, Xiangli Zhong, Dongguo Zhang, Weijie Duan, Xiaolei Li, Shuaizhi Zheng, and Jinbin Wang. TiO_2 nanorod arrays/ZnO nanosheets heterostructured photoanode for quantum-dot-sensitized solar cells. *Solar Energy*, 166:371–378, 2018.

[122] Hongye Yuan, Saif Abdulla Ali Alateeqi Aljneibi, Jiaren Yuan, Yuxiang Wang, Hui Liu, Jie Fang, Chunhua Tang, Xiaohong Yan, Hong Cai, Yuandong Gu, et al. ZnO nanosheets abundant in oxygen vacancies derived from metal-organic frameworks for ppb-level gas sensing. *Advanced Materials*, 31(11):1807161, 2019.

[123] Shobhnath P Gupta, Amit S Pawbake, Bhaskar R Sathe, Dattatray J Late, and Pravin S Walke. Superior humidity sensor and photodetector of mesoporous ZnO nanosheets at room temperature. *Sensors and Actuators B: Chemical*, 293:83–92, 2019.

[124] Ziqi Sun, Ting Liao, Yuhai Dou, Soo Min Hwang, Min-Sik Park, Lei Jiang, Jung Ho Kim, and Shi Xue Dou. Generalized self-assembly of scalable two-dimensional transition metal oxide nanosheets. *Nature communications*, 5(1):1–9, 2014.

[125] Y Manjula, R Rakesh Kumar, P Missak Swarup Raju, G Anil Kumar, T Venkatappa Rao, A Akshaykranth, and P Supraja. Piezoelectric flexible nanogenerator based on ZnO nanosheet networks for mechanical energy harvesting. *Chemical Physics*, 533:110699, 2020.

[126] Steven J Limmer, Elizabeth A Kulp, and Jay A Switzer. Epitaxial electrodeposition of ZnO on $Au(111)$ from alkaline solution: Exploiting amphoterism in $Zn(II)$. *Langmuir*, 22(25):10535–10539, 2006.

[127] Gamini Gunawardena, Graham Hills, Irene Montenegro, and Benjamin Scharifker. Electrochemical nucleation: part I. general considerations. *Journal of Electroanalytical Chemistry and Interfacial Electrochemistry*, 138(2):225–239, 1982.

[128] MR Khelladi, L Mentar, M Boubatra, and A Azizi. Study of nucleation and growth process of electrochemically synthesized ZnO nanostructures. *Materials Letters*, 67 (1):331–333, 2012.

[129] Brendan Enright and Donald Fitzmaurice. Spectroscopic determination of electron and hole effective masses in a nanocrystalline semiconductor film. *The Journal of Physical Chemistry*, 100(3):1027–1035, 1996.

[130] Masanobu Izaki and Takashi Omi. Characterization of transparent zinc oxide films prepared by electrochemical reaction. *Journal of the Electrochemical Society*, 144 (6):1949, 1997.

[131] Takashi Yamamoto, Tadashi Shiosaki, and Akira Kawabata. Characterization of *ZnO* piezoelectric films prepared by rf planar-magnetron sputtering. *Journal of Applied Physics*, 51(6):3113–3120, 1980.

[132] Benjamin Scharifker and Graham Hills. Theoretical and experimental studies of multiple nucleation. *Electrochimica acta*, 28(7):879–889, 1983.

[133] S Strbac and Radoslav R Adžić. The influence of pH on reaction pathways for O_2 reduction on the Au (100) face. *Electrochimica Acta*, 41(18):2903–2908, 1996.

[134] SP Jiang, CQ Cui, and ACC Tseung. Reactive deposition of cobalt electrodes: V. Mechanistic studies of oxygen reduction in unbuffered neutral solutions saturated with oxygen. *Journal of the Electrochemical Society*, 138(12):3599, 1991.

[135] Sophie Peulon and Daniel Lincot. Mechanistic study of cathodic electrodeposition of zinc oxide and zinc hydroxychloride films from oxygenated aqueous zinc chloride solutions. *Journal of the Electrochemical Society*, 145(3):864, 1998.

[136] T Pauporté, E Jouanno, F Pellé, B Viana, and P Aschehoug. Key growth parameters for the electrodeposition of *ZnO* films with an intense UV-light emission at room temperature. *The Journal of Physical Chemistry C*, 113(24):10422–10431, 2009.

[137] R Könenkamp, K Boedecker, M Ch Lux-Steiner, M Poschenrieder, F Zenia, C Levy-Clement, and S Wagner. Thin film semiconductor deposition on free-standing ZnO columns. *Applied Physics Letters*, 77(16):2575–2577, 2000.

[138] H Rudigier, E Bergmann, and J Vogel. Properties of ion-plated TiN coatings grown at low temperatures. *Surface and Coatings Technology*, 36(3-4):675–682, 1988.

[139] Wan-Yu Wu, Tzu-Ling Chen, and Jyh-Ming Ting. Effects of seed layer precursor type on the synthesis of ZnO nanowires using chemical bath deposition. *Journal of the Electrochemical Society*, 157(8):K177, 2010.

[140] Adriana Paracchino, Jan Cornelius Brauer, Jacques-Edouard Moser, Elijah Thimsen, and Michael Graetzel. Synthesis and characterization of high-photoactivity electrodeposited Cu2O solar absorber by photoelectrochemistry and ultrafast spectroscopy. *The Journal of Physical Chemistry C*, 116(13):7341–7350, 2012.

[141] Andrew T Marin, David Muñoz-Rojas, Diana C Iza, Talia Gershon, Kevin P Musselman, and Judith L MacManus-Driscoll. Novel atmospheric growth technique to improve both light absorption and charge collection in ZnO/Cu_2O thin film solar cells. *Advanced Functional Materials*, 23(27):3413–3419, 2013.

[142] Kevin P Musselman, Andreas Wisnet, Diana C Iza, Holger C Hesse, Christina Scheu, Judith L MacManus-Driscoll, and Lukas Schmidt-Mende. Strong efficiency improvements in ultra-low-cost inorganic nanowire solar cells. *Advanced Materials*, 22(35):E254–E258, 2010.

[143] Mahmoud Abdelfatah, Johannes Ledig, Abdelhamid El-Shaer, Azat Sharafeev, Peter Lemmens, Mohsen Mohamed Mosaad, Andreas Waag, and Andrey Bakin. Effect of potentiostatic and galvanostatic electrodeposition modes on the basic parameters of solar cells based on Cu_2O thin films. *ECS Journal of Solid State Science and Technology*, 5(6):Q183, 2016.

[144] Kevin P Musselman, Andrew Marin, Lukas Schmidt-Mende, and Judith L MacManus-Driscoll. Incompatible length scales in nanostructured Cu_2O solar cells. *Advanced Functional Materials*, 22(10):2202–2208, 2012.

[145] Radim Beranek. (Photo) electrochemical methods for the determination of the band edge positions of TiO_2 based nanomaterials. *Advances in Physical Chemistry*, 2011, 2011.

[146] Shi-Zhao Kang, Hong Liu, Xiangqing Li, Mojie Sun, and Jin Mu. Electrochemical behavior of eugenol on TiO_2 nanotubes improved with Cu_2O clusters. *RSC Advances*, 4(2):538–543, 2014.

[147] N Sobti, A Bensouici, Fernando Coloma, Carlos Untiedt, and S Achour. Structural and photoelectrochemical properties of porous TiO_2 nanofibers decorated with Fe_2O_3 by sol-flame. *Journal of nanoparticle research*, 16(8):1–10, 2014.

[148] Guangli Li, Yaohan Huang, Qingfei Fan, Meili Zhang, Qi Lan, Ximei Fan, Zuowan Zhou, and Chaoliang Zhang. Effects of bath pH on structural and electrochemical performance of Cu_2O. *Ionics*, 22(11):2213–2223, 2016.

[149] Longcheng Wang and Meng Tao. Fabrication and characterization of p-n homojunctions in cuprous oxide by electrochemical deposition. *Electrochemical and Solid State Letters*, 10(9):H248, 2007.

[150] Jinyan Pan, Chengfu Yang, and Yunlong Gao. Investigations of cuprous oxide and cupric oxide thin films by controlling the deposition atmosphere in the reactive sputtering method. *Sens. Mater*, 28(7):817–824, 2016.

[151] Ying Yang, Juan Han, Xiaohui Ning, Jinzhan Su, Jinwen Shi, Wei Cao, and Wei Xu. Photoelectrochemical stability improvement of cuprous oxide (Cu_2O) thin films in aqueous solution. *International Journal of Energy Research*, 40(1):112–123, 2016.

[152] Marcel Pourbaix. Atlas of electrochemical equilibria in aqueous solution. *NACE*, 307, 1974.

[153] AE Rakhshani. The role of space-charge-limited-current conduction in evaluation of the electrical properties of thin Cu_2O films. *Journal of applied physics*, 69(4): 2365–2369, 1991.

[154] Kotaro Mizuno, Masanobu Izaki, Kuniaki Murase, Tsutomu Shinagawa, Masaya Chigane, Minoru Inaba, Akimasa Tasaka, and Yasuhiro Awakura. Structural and electrical characterizations of electrodeposited p-type semiconductor Cu_2O films. *Journal of The Electrochemical Society*, 152(4):C179, 2005.

[155] Felipe Caballero-Briones, Juan M Artés, Ismael Díez-Pérez, Pau Gorostiza, and Fausto Sanz. Direct observation of the valence band edge by in situ ECSTM-ECTS in p-type Cu_2O layers prepared by copper anodization. *The Journal of Physical Chemistry C*, 113(3):1028–1036, 2009.

[156] S Laidoudi, AY Bioud, A Azizi, G Schmerber, J Bartringer, S Barre, and A Dinia. Growth and characterization of electrodeposited Cu_2O thin films. *Semiconductor science and technology*, 28(11):115005, 2013.

[157] K Nakaoka, J Ueyama, and K Ogura. Photoelectrochemical behavior of electrodeposited cuo and Cu_2O thin films on conducting substrates. *Journal of the Electrochemical Society*, 151(10):C661, 2004.

[158] Weichao Wang, Dangxin Wu, Qiming Zhang, Longcheng Wang, and Meng Tao. pH-dependence of conduction type in cuprous oxide synthesized from solution. *Journal of applied physics*, 107(12):123717, 2010.

[159] Hannes Raebiger, Stephan Lany, and Alex Zunger. Origins of the p-type nature and cation deficiency in Cu_2O and related materials. *Physical Review B*, 76(4):045209, 2007.

[160] Clemens Burda, Xiaobo Chen, Radha Narayanan, and Mostafa A El-Sayed. Chemistry and properties of nanocrystals of different shapes. *Chemical reviews*, 105(4): 1025–1102, 2005.

[161] Jiaguo Yu, Jingxiang Low, Wei Xiao, Peng Zhou, and Mietek Jaroniec. Enhanced photocatalytic CO_2-reduction activity of anatase TiO_2 by coexposed {001} and {101} facets. *Journal of the American Chemical Society*, 136(25):8839–8842, 2014.

[162] Hao Bin Wu, Jun Song Chen, Huey Hoon Hng, and Xiong Wen David Lou. Nanostructured metal oxide-based materials as advanced anodes for lithium-ion batteries. *Nanoscale*, 4(8):2526–2542, 2012.

[163] Zhiyu Wang, Liang Zhou, and Xiong Wen Lou. Metal oxide hollow nanostructures for lithium-ion batteries, 2012.

[164] Gang Liu, C Yu Jimmy, Gao Qing Max Lu, and Hui-Ming Cheng. Crystal facet engineering of semiconductor photocatalysts: motivations, advances and unique properties. *Chemical Communications*, 47(24):6763–6783, 2011.

[165] Xiaodong Li, Hongsheng Gao, Catherine J Murphy, and Linfeng Gou. Nanoindentation of Cu_2O nanocubes. *Nano Letters*, 4(10):1903–1907, 2004.

[166] Li Zhang and Hui Wang. Cuprous oxide nanoshells with geometrically tunable optical properties. *ACS nano*, 5(4):3257–3267, 2011.

[167] Chun-Hong Kuo and Michael H Huang. Fabrication of truncated rhombic dodecahedral Cu_2O nanocages and nanoframes by particle aggregation and acidic etching. *Journal of the American Chemical Society*, 130(38):12815–12820, 2008.

[168] Mei Leng, Mingzhu Liu, Yibo Zhang, Zhenqing Wang, Chao Yu, Xiangguang Yang, Hongjie Zhang, and Cheng Wang. Polyhedral 50-facet Cu_2O microcrystals partially enclosed by {311} high-index planes: synthesis and enhanced catalytic CO oxidation activity. *Journal of the American Chemical Society*, 132(48):17084–17087, 2010.

[169] Xiaofei Han, Kunhee Han, and Meng Tao. n-Type Cu_2O by electrochemical doping with Cl. *Electrochemical and Solid State Letters*, 12(4):H89, 2009.

[170] Tengfei Jiang, Tengfeng Xie, Wanshi Yang, Liping Chen, Haimei Fan, and Dejun Wang. Photoelectrochemical and photovoltaic properties of p–n Cu_2O homojunction films and their photocatalytic performance. *The Journal of Physical Chemistry C*, 117(9):4619–4624, 2013.

[171] Silvia Pelegrini, Iuri S Brandt, Cristiani C Plá Cid, Eduardo A Isoppo, Alexandre DC Viegas, and Andre A Pasa. Electrochemical Cl doping of Cu_2O: structural

and morphological properties. *ECS Journal of Solid State Science and Technology*, 4(7):P181, 2015.

[172] G Riveros, M León, and D Ramírez. Effect of chloride ions on the structural, optical, morphological, and electrochemical properties of Cu_2O films electrodeposited on fluorine-doped tin oxide substrate from a dmso solution. *Journal of the Chilean Chemical Society*, 61(4):3219–3223, 2016.

[173] Qiong Bai, Weichao Wang, Qiming Zhang, and Meng Tao. n-type doping in Cu_2O with F, Cl, and Br: A first-principles study. *Journal of Applied Physics*, 111(2): 023709, 2012.

[174] G Ya Krasnikov and VP Bokarev. Surface energy and crystal faceting of elemental semiconductors and other substances. In *Doklady Physical Chemistry*, volume 382, pages 14–17. Springer, 2002.

[175] Samuel I Stupp and Paul V Braun. Molecular manipulation of microstructures: biomaterials, ceramics, and semiconductors. *Science*, 277(5330):1242–1248, 1997.

[176] Yugang Sun and Younan Xia. Shape-controlled synthesis of gold and silver nanoparticles. *science*, 298(5601):2176–2179, 2002.

[177] Matthew J Siegfried and Kyoung-Shin Choi. Elucidating the effect of additives on the growth and stability of Cu_2O surfaces via shape transformation of pre-grown crystals. *Journal of the American Chemical Society*, 128(32):10356–10357, 2006.

[178] Kyoung-Shin Choi. Shape control of inorganic materials via electrodeposition. *Dalton Transactions*, (40):5432–5438, 2008.

[179] Sven Ruhle, Assaf Y Anderson, Hannah-Noa Barad, Benjamin Kupfer, Yaniv Bouhadana, Eli Rosh-Hodesh, and Arie Zaban. All-oxide photovoltaics. *The journal of physical chemistry letters*, 3(24):3755–3764, 2012.

[180] Elvira Fortunato, Pedro Barquinha, and Rodrigo Martins. Oxide semiconductor thin-film transistors: a review of recent advances. *Advanced materials*, 24(22):2945–2986, 2012.

[181] Peter Schröer, Peter Krüger, and Johannes Pollmann. First-principles calculation of the electronic structure of the wurtzite semiconductors ZnO and ZnS. *Physical Review B*, 47(12):6971, 1993.

[182] Zong-Liang Tseng, Chien-Hung Chiang, and Chun-Guey Wu. Surface engineering of ZnO thin film for high efficiency planar perovskite solar cells. *Scientific reports*, 5(1):1–10, 2015.

[183] Hock Beng Lee, Riski Titian Ginting, Sin Tee Tan, Chun Hui Tan, Abdelelah Alshanableh, Hind Fadhil Oleiwi, Chi Chin Yap, Mohd Hafizuddin Hj Jumali, and Muhammad Yahaya. Controlled defects of fluorine-incorporated ZnO nanorods for photovoltaic enhancement. *Scientific reports*, 6(1):1–11, 2016.

[184] Zhengrong Yao, Kun Tang, Jiandong Ye, Zhonghua Xu, Shunming Zhu, and Shulin Gu. Identification and control of native defects in N-doped ZnO microrods. *Optical Materials Express*, 6(9):2847–2856, 2016.

Résumé:

La nanostructuration des cellules solaires est une approche intéressante pour améliorer le rendement de conversion photovoltaïque (ARP) dans laquelle l'objectif principal de cette thèse est d'améliorer la performance des nanostructures électrodéposées à base de Cu_2O et de ZnO pour les dispositifs photovoltaïques. L'effet de nombreux paramètres clés a été étudié pour les deux oxydes métalliques afin de contrôler leurs propriétés physiques et électrochimiques. Dans un premier temps, une étude comparative entre le mode galvanostatique et potentiostatique a été effectuée pour des nanofeuillets de ZnO ($ZnO_{(NS)}$) et des nanofils de ZnO ($ZnO_{(NW)}$). Deuxièmement, une stratégie similaire a été appliquée pour les nanostructures et les nanoparticules de Cu_2O Où les paramètres structurels, morphologiques, optiques et électrochimiques ont été étudiés pour les nanostructures synthétisées à base de ZnO et celles de Cu_2O qu'elles ont montré de bonnes performances et une stabilité photoélectrochimique élevée. Enfin, une architecture d'une hétérojonction $(p-Cu_2O/n-ZnO_{(NW)}/ZnO_{(NS)})$ a été proposée et examinée sous les différentes approches d'électrodéposition. Dont $n-ZnO_{(NW)}\ /ZnO_{(NS)}$ est la couche conductrice dans l'hétérojonction et Cu_2O est la couche absorbante.

Mots clés: Electrodeposition, nanostructures, heterojunction, optoelectronique.

الملخص:

تعتبر البنية النانوية للخلايا الشمسية طريقة مثيرة للاهتمام من أجل رفع كفاءة التحويل (PCE)، حيث يتمثل الهدف الرئيسي لهذه الأطروحة في تعزيز الأداء للهياكل النانوية لأكسيد الزنك (ZnO) وأكسيد النحاس (Cu_2O) المستخدمة في الأجهزة الإلكتروضوئية. حيث تمت دراسة العديد من العوامل الرئيسية المؤثرة على الخصائص الفيزيائية والكهروكيميائية لكل من أكاسيد المعادن المدروسة. أولا قمنا بدراسة مقارنة بين الرقائق النانوية المرسبة باستخدام وضع الغالفانوستاتيك و الرقائق المرسبة تحت وضع البوتونسيوستاتيك لكل من الوريقات النانوية $(ZnO_{(NS)})$ والاعمدة النانوية $(ZnO_{(NW)})$. بالمقابل تم تطبيق إستراتيجية مماثلة على الهياكل النانوية النانوية لثاني أكسيد النحاس. جودة العينات تم فحصها من خلال دراسة خصائصها الهيكلية والتشكيلية والبصرية والكهروكيميائية، حيث أظهرت الأداء الجيد والاستقرار الكهروضوئي العالي. في الأخير تم اقتراح نموذج لوصلة غير متجانسة $(p-Cu_2O/n-ZnO_{(NW)}/ZnO_{(NS)})$ ثم فحصها في ظل اختلاف نهج الترسيب الكهربائي. حيث أن Cu_2O هي الطبقة الماصة و $ZnO_{(NW)}\ /ZnO_{(NS)}$ هي الطبقة الناقلة.

الكلمات المفتاحية: الترسيب الكهروكيميائي، الهياكل النانوية، وصلة غير متجانسة، الكهروضوئي.